Degradation of the electrical performance of Printed Circuit Boards (PCBs) after cyclic thermo-mechanical loading

Dissertation

by

Klaus Fellner

prepared at the

Polymer Competence Center Leoben GmbH

in cooperation with the

Institute of Materials Science and Testing of Polymers

and the

Institute of Mechanics

submitted to the

Montanuniversitaet Leoben

Academic Advisor

Univ.-Prof. DI Dr. Thomas Antretter
Montanuniversität Leoben, Austria

Supervisor

DI Dr. Peter Filipp Fuchs
Polymer Competence Center Leoben, Austria

Leoben, December 2015

I declare in lieu of oath, that I wrote this dissertation and performed the associated research myself, using only the support indicated in the acknowledgements and literature cited.

Leoben, December 2015 Klaus Fellner

The research associated with this thesis was published in the following papers. The use of published material in this thesis is explicitly permitted in all cases.

Fellner, K., Fuchs, P.F., Pinter, G., Antretter, T., Krivec, T.: Method development for the cyclic characterization of thin copper layers for PCB applications. Circuit World **40**(2), 53–60 (2014). doi: 10.1108/CW-09-2013-0032

Fellner, K., Fuchs, P.F., Antretter, T., Pinter, G., Schongrundner, R.: Determination of cyclic mechanical properties of thin copper layers for PCB applications. EuroSimE 2014. doi: 10.1109/EuroSimE.2014.6813788

Fellner, K., Antretter, T., Fuchs, P.F., Pélisset, T.: Cyclic mechanical behavior of thin layers of copper: An experimental and numerical study. Accepted for publication in: The Journal of Strain Analysis for Engineering Design.

Fellner, K., Antretter, T., Fuchs, P.F.: Numerical simulation of the electrical performance of PCBs under cyclic thermal loads. Submitted to: Microelectronics Reliability

ACKNOWLEDGEMENTS

In the beginning I would like to thank Prof. Dr. Thomas Antretter and Dr. Peter Fuchs for their comprehensive support for this thesis and for the review of the linked papers. Without the aid of Thomas Antretter the simulation work performed in this thesis would not have been possible, without the encouragement of Peter Fuchs the experimental section of the thesis would not have its scope.

Furthermore, I thank Prof. Dr. Gerald Pinter for his guidance and for the possibility to perform the testing associated with this thesis at the Institute of Materials Science and Testing of Plastics (Montanuniversitaet Leoben).

I appreciate the practical assistance, training and instruction in the field of materials testing given by DI Peter Guttmann, DI Andreas Moser, Dr. Steffen Stelzer and Jürgen Föttinger very much. The friendly support of Jürgen Grosser and Stefan Hinterdorfer in the materials testing lab as well as their ideas and comments was very valuable for me. I am grateful to Dr. Michael Berer for help with the cyclic four point bending tests as well as to Dr. Bernd Schrittesser for help with the blow-up tests.

For fruitful discussions about simulation and for general assistance at the labs I am indebted to Dr. Daniel Tscharnuter, Harish Pothukuchi, MSc and Astrid Rauschenbach. Besides, Daniel Tscharnuter and Harald Schmid designed the device used for V-notched rail shear testing and the tension-compression testing in this thesis. I would like to thank Martin Birker for the preparation of numerous specimens.

I would like to express my graditute to Dr. Ronald Schöngrundner for measurement results and to Dr. Tiphaine Pelisset for the valueable results of curvature measurements, which were used to validate the model developed in this thesis.

For practical help and assistance with the handling of numerical models my thanks go to Martin Krobath and Dr. Peter Raninger. I am indebted to DI Karl Flicker, who helped me with the computer cluster any time necessary.

DI Thomas Krivec, Tao Chee, MSc and DI Daniela Zechner, current or former employees of Austria Technologie & Systemtechnik Aktiengesellschaft contributed in an essential way to my thesis by providing sample material, measurement results and of course their broad knowledge in the field of printed circuit boards.

For support and understanding during the whole time I am grateful to my family, my girlfriend and friends.

The research work of this doctoral thesis was performed within the COMET-projects „Micromechanical modelling and advanced fracture simulation of printed circuit boards (PCBs)“ (project-no.: IV.3.05) and „Micromechanical modelling and advanced fracture simulation of printed circuit boards (PCBs) Part II“ (project-no.: V.3.07) at the Polymer Competence Center Leoben GmbH (PCCL, Austria) within the framework of the COMET-program of the Federal Ministry for Transport, Innovation and Technology and Federal Ministry of Economy, Family and Youth with contributions by the Montanuniversitaet Leoben (Institute of Mechanics and Institute of Materials Science and Testing of Plastics) and Austria Technologie & Systemtechnik Aktiengesellschaft. The PCCL is funded by the Austrian Government and the State Governments of Styria, Lower Austria and Upper Austria.

ABSTRACT

The overall objective of this research work is the improvement of the failure behavior of Printed Circuit Boards (PCBs). During the thermal loading of PCBs stresses arise due to the different coefficients of thermal expansion of the materials. As the conducting paths are made of copper, the focus is on the characterization of thin copper layers used for PCBs. The mechanical properties of these copper layers are determined in cyclic four point bending tests and in cyclic tensile-compression tests, as their behavior under changing tensile and compression loads needs to be evaluated. Specimens for the four point bend tests are manufactured by bonding 18 µm thick copper layers on both sides of 10 mm thick silicone plates. The silicone is characterized in tensile, shear and blow-up tests to provide input data for a hyperelastic material model. Specimens for the cyclic tensile-compression tests are produced in a compression molding process. Four layers of glass fiber reinforced epoxy resin (thickness 90 µm) and five layers of copper (thickness 60 µm) are applied. The results show that, due to the hyperelastic material behavior of silicone, the four point bend tests are applicable only for small strains, while the cyclic tension-compression tests can be applied to characterize thin copper foils in tension and compression up to one percent strain. Therefore such tests are conducted at different temperatures and loading conditions, covering the spectrum of strains occurring in the application.

Based on these experimental results, cyclic material parameters are determined. The obtained material response is modeled using the “Nonlinear isotropic/kinematic hardening model” built in in the Finite Element Analysis (FEA)-software Abaqus. It is capable of modelling the cyclic plastic material behavior of metals. For every loading case the optimal set of parameters is determined using an optimization procedure. Based on the known parameter sets of the individual loading cases the calibration of a “Nonlinear isotropic/kinematic hardening model” for all R-ratios and temperatures is undertaken and the findings are discussed. The kinematic hardening parameters are fitted in an optimization process from the hysteretic force-strain curves obtained in the cyclic tension-compression tests. The

isotropic hardening variables are determined based on the yield stress versus plastic strain relationship that is constructed incrementally from the available individual cycles. The so-obtained curve is found to be not unique, but to depend on the loading situation. Hence different approaches for strain range memorization are evaluated. Since these approaches have been developed for modelling strain-controlled tests, whereas the experimental data is obtained in a force-controlled way, a phenomenological formulation is developed and applied. This model accounts for the observed mean stress dependency of the plastic properties and is thus called “mean backstress memorization model”. The results of curvature measurements during thermal cycling are used for model validation. The experimental results and the numerical predictions are in good agreement.

In the last part of this thesis, different PCB designs are tested in Interconnection Stress Tests (IST). In such tests, PCBs are subjected to temperature cycles alternating between two extremes (e.g. -40°C to 160°C). The electrical resistance is measured on-line during these tests. If the resistance rises by more than 10% of the initial value at the highest temperature, the test is terminated. The stress/strain states computed by Abaqus serve as input to a pore growth model which eventually allows working out an indicator for the electrical performance loss. Subsequently, electrical FEA are conducted to obtain a correlation between the pore volume fraction distributed over the structure and the electrical resistance increase. The results of the simulations are compared to experimental results to determine parameters. Finally the so-computed distribution of the pore volume fraction is compared to micrographs of PCBs tested in ISTs. They are in good agreement.

KURZFASSUNG

Das übergeordnete Ziel dieser Forschungsarbeit ist die Verbesserung des Versagensverhaltens von Leiterplatten. Wird eine Leiterplatte wechselnden Temperaturen ausgesetzt, entstehen mechanische Spannungen aufgrund der unterschiedlichen Wärmeausdehnungskoeffizienten der eingesetzten Materialien. Da die Leiterbahnen selbst aus Kupfer bestehen, liegt der Schwerpunkt dieser Arbeit auf der Charakterisierung dünner Kupferschichten, wie sie in Leiterplatten verwendet werden. Die mechanischen Eigenschaften dieser Kupferschichten werden in zyklischen Vierpunkt-Biegetests und in zyklischen Zug-Druck-Tests charakterisiert, da das Verhalten der Kupferschichten bei wechselnder Zug- und Druckbelastung bestimmt werden muss. Prüfkörper für die Vierpunkt-Biegetests werden durch Aufkleben von 18 µm dicken Kupferschichten auf beide Seiten einer 10 mm dicken Silikonplatte hergestellt. Das Silikon wird in Zug- und Scherversuchen sowie in biaxialen Tests charakterisiert, um Eingangsdaten für ein hyperelastisches Materialmodell zu sammeln. Prüfkörper für die zyklischen Zug-Druck-Tests werden in einem Formpressverfahren hergestellt. Vier Schichten aus glasfaserverstärktem Epoxidharz (Dicke 90 µm) und fünf Schichten aus Kupfer (Dicke 60 µm) werden verpresst. Die Ergebnisse zeigen, dass die Vierpunkt-Biegetests aufgrund der Hyperelastizität des Silikons nur für kleine Dehnungen anwendbar sind. Die zyklischen Zug-Druck-Tests aber können erfolgreich eingesetzt werden, um dünne Kupferfolien unter wechselnden Zug- und Drucklasten zu charakterisieren. Dies ist für Dehnungen bis zu einem Prozent möglich. Daher werden diese Tests bei unterschiedlichen Temperaturen und R-Verhältnissen durchgeführt, um das Spektrum von Belastungen, die in der Anwendung auftreten, abzudecken.

Auf der Grundlage dieser experimentellen Ergebnisse werden zyklische Materialparameter bestimmt. Die erhaltene Materialantwort wird mit Hilfe des "Nichtlinearen isotropen / kinematischen Verfestigungsmodells", welches in der Finite-Elemente-Analyse (FEA)-Software Abaqus zur Verfügung steht, modelliert.

Es ist zur Simulation des zyklischen plastischen Materialverhaltens von Metallen geeignet. Für jeden Lastfall wird der optimale Parametersatz in einem Optimierungsverfahren bestimmt. Auf Basis der bekannten Parametersätze der einzelnen Lastfälle wird die Kalibrierung eines "Nichtlinearen isotropen / kinematischen Verfestigungsmodells" für alle Temperaturen und R-Verhältnisse durchgeführt, und die Ergebnisse werden diskutiert. Die kinematischen Verfestigungsparameter werden in einem Optimierungsprozess aus den hysteretischen Kraft-Dehnungskurven der zyklischen Zug-Druck-Tests bestimmt. Aus den verfügbaren Hysteresen einzelner Zyklen werden inkrementell Kurven der Fließspannung über der plastischen Dehnung konstruiert. Aus diesen werden die isotropen Verfestigungsparameter abgeleitet. Diese sind jedoch nicht eindeutig, sondern hängen vom R-Verhältnis ab. Daher werden unterschiedliche Ansätze zur Modellierung dieser Abhängigkeit evaluiert. Da diese Ansätze aber zur Simulation dehnungsgesteuerter Versuche entwickelt wurden, die experimentellen Daten in dieser Arbeit aber aus kraftgesteuerten Versuchen stammen, wird eine eigene phänomenologische Formulierung entwickelt. Diese verwendet die beobachtete Mittelspannungsabhängigkeit der plastischen Materialeigenschaften und wird daher als "Modell der mittleren Rückspannung" bezeichnet. Die Ergebnisse von Krümmungsmessungen während thermischer Belastung werden zur Modellvalidierung verwendet. Die experimentellen Ergebnisse und die numerischen Vorhersagen stimmen gut überein.

Im letzten Teil dieser Arbeit werden verschiedene Leiterplattendesigns im „Interconnection Stress Test“ (IST) geprüft. Bei solchen Tests werden Leiterplatten thermisch zwischen zwei Extremen (beispielsweise -40°C bis 160°C) zykliert. Der elektrische Widerstand wird während dieser Versuche stets mitgemessen. Erhöht sich der Widerstand um mehr als 10% des Ausgangswertes (betrachtet werden immer Werte bei der höchsten Temperatur), so wird der Test abgebrochen. Die Leiterplattenstrukturen werden in der FEA-Software Abaqus mit dem zuvor entwickelten Materialmodell modelliert. Die in Abaqus berechneten Spannungs- und Dehnungszustände dienen als Basis für ein Porenwachstumsmodell. Das Porenvolumen ist ein Indikator für den Anstieg des elektrischen Widerstandes.

Anschließend werden elektrische FEA durchgeführt, um eine Korrelation zwischen dem Porenvolumenanteil in den verschiedenen Leiterplattenstrukturen und der elektrischen Widerstandserhöhung zu erhalten. Die Ergebnisse der Simulationen werden mit experimentellen Ergebnissen verglichen, um Parameter zu bestimmen. Schließlich wird die berechnete Verteilung des Porenvolumenanteils mit Schliffbildern von Leiterplatten, welche in ISTs getestet wurden, verglichen. Sie sind in guter Übereinstimmung.

LIST OF SYMBOLS

Symbol	Quantity	Dimension
A_S	Cross section	mm²
A	Pore growth parameter	-
b	Isotropic hardening parameter	-
B	Pore growth parameter	-
C	Backstress evolution parameter	MPa
c	Inner variable	MPa
D_{Ogden}	Ogden model parameter	1/MPa
D	Material parameter	MPa
$\mathbf{D}$	(Forth order) elasticity tensor	MPa
E	Young's Modulus	MPa
F	Force	N
F_m	Memory surface	-
F_y	Yield surface	MPa
g	Material parameter	1/MPa
G	Shear Modulus	MPa
H()	Heaviside function	n.a.
h_f	Film thickness	mm
h_S	Substrate thickness	mm
i	counting parameter	-
$I_1()$	First invariant of a tensor	n.a.
J()	Second invariant of a deviatoric tensor	n.a.
J_{el}	Elastic volume strain	-
J_{tot}	Total volume strain	-
K	Exponent	-
M	Biaxial modulus	MPa
ME	Mean error	-
N	Number of cycles	-

n	Number of trials	-
$\mathbf{n}$	Normal unit to the yield surface	-
$\mathbf{n}^*$	Normal unit to the memory surface	MPa
q	Radius of the memory surface	-
Q	Yield stress of the stab. cycle	MPa
Q_S	Extremal yield stress	MPa
Q_∞	Yield stress ($Q_\infty = Q - \sigma\|_0$)	MPa
R	Electrical resistance	Ω
r	Pore radius	mm
RSME	Root mean square error	-
$\mathbf{S}$	Deviatoric stress tensor	MPa
s_{11}	Compliance coefficient	1/MPa
s_{12}	Compliance coefficient	1/MPa
T	Temperature	K
t	Time	s
T_C	Cycle duration	s
U	Displacement	mm
U_S	Strain energy potential	MPa
V	Pore volume fraction	-
w	Displacement (z-direction)	mm
:	Double dot product	n.a.
α	Pore growth parameter	-
α_{Ogden}	Ogden model parameter	-
α_{therm}	Coefficient of thermal expansion	1/K
$\boldsymbol{\alpha}$	Backstress tensor	MPa
β	Temperature correlation coefficient	1/K
γ	Shear strain	-
γ	(indexed) Backstress evolution parameter	-
ε	Strain	-

$\boldsymbol{\varepsilon}$	Total strain tensor	-
$\dot{\boldsymbol{\varepsilon}}^{\mathrm{el}}$	Elastic strain rate tensor	1/s
$\varepsilon^{\mathrm{pl}}$	Plastic strain	-
$\bar{\varepsilon}^{\mathrm{pl}}$	Equivalent plastic strain	-
$\boldsymbol{\varepsilon}^{\mathrm{pl}}$	Plastic strain tensor	-
$\boldsymbol{\zeta}$	Backstrain tensor	-
η	Strain range memorization parameter	-
κ	Curvature	1/mm
λ	Principal stretch	-
$\bar{\lambda}$	Normalized principal stretch	-
μ	Strain range memorization parameter	-
μ_{Ogden}	Ogden model parameter	MPa
ρ	Specific electrical resistivity	Ωm
σ	Stress	MPa
$\sigma\vert_0$	Initial yield stress	MPa
σ^0	Current yield stress	MPa
σ_{eq}	Equivalent stress	MPa
σ_f	Average stress in the film	MPa
σ_m	Hydrostatic stress	MPa
$\boldsymbol{\sigma}$	Stress tensor	MPa
τ	Shear stress	MPa
υ	Poisson's Ratio	-

TABLE OF CONTENTS

1. INTRODUCTION

1.1. Motivation

Printed circuit boards (PCBs) are composite structures mainly made of epoxy resin, glass fibers and copper. As these materials show different coefficients of thermal expansion, stresses are induced when PCBs are thermally loaded. For lifetime assessment cyclic thermal loading must be taken into consideration. Application examples for these loading conditions include control and regulation systems of motors of vehicles as well as mobile phones. Due to the miniaturization of electronics in general and in particular of PCBs the dimensions of the conducting paths decrease. Therefore high mechanical stresses in these areas can arise, which entails special demands on design and materials. Industry-wide standards to experimentally test the cyclic temperature performance are the Thermal Cycle Tests (TCT) [1-3] and the Thermal Shock Tests (TST) [4], where PCBs are exposed alternately to hot (up to 160°C) and cold (down to -55°C) temperatures. To reduce the experimental testing effort and to spare the associated costs, current research in this field is focused on finite element models used to test and evaluate PCBs [5-8] in a virtual way.

The aim of this thesis is to provide finite element models for lifetime assessment of PCBs under cyclic thermal loads. As the conducting paths are made of copper, the focus is on the characterization of thin copper layers used for PCBs. Copper is one of the best characterized metals, at least as far as the bulk behavior is concerned. Also for thin films in the order of a few nanometer to about one micrometer [9-13] the literature offers some results. However, only little information is available for the size ranges of thin foils under consideration in this work, i.e. from 1 to 100 micrometer. While basic information on the material's response under monotonic loading is comparatively easily accessible, in PCBs we are facing the following additional challenges, if the ultimate goal to predict failure of a PCB component under service conditions is to be achieved. (i) The cyclic elastic plastic material behavior must be determined for the full number of cycles to failure. This entails a large magnitude of the accumulated plastic strain. A viable material model has to

be formulated which is general enough to still perform well at these high accumulated strains, (ii) the cyclic temperature history as it occurs under service conditions must be accounted for, (iii) the material model must be capable of capturing many different R-ratios. This is especially critical for compressive loads where experiments on thin foils are difficult to perform and thus experimental data scarce. A trustworthy prediction of PCB failure due to via damage has therefore not yet been achieved. This work presents a continuum mechanical approach to deal with that issue. Based on generally accepted concepts such as isotropic and kinematic hardening, a novel idea will be presented that takes into account the mean stress sensitivity as it is commonly observed in fatigue tests. To this end the four steps necessary for developing a sound material model are taken: (i) Provide the experimental database covering all the aspects demanded by the application, see the discussion above, (ii) identify an appropriate material description and formulate the corresponding equations, (iii) determine the associated material parameters and (iv) validate the so-determined material law against experiments different from the ones used in (i).

Hence this work shall provide a method to measure the cyclic material behavior of copper in order to be able to describe it in the simulation models. The finite element models shall describe the constitutive behavior of PCBs under cyclic thermal loads as well as the damage evolution.

1.2. Overview of this thesis

Since the reliability of PCBs is crucial to the performance of modern electronics, considerable research has been done on the service life and failure behavior of PCBs. Hence there are different methodologies and standards published in the literature for the mechanical [14,15] as well as for the thermo-mechanical testing [1-4] of PCBs. Scientists have worked on drop or bend tests [16-19] in the mechanical area and on thermal cycle and thermal shock tests [20] in the thermo-mechanical area. As irreversible, plastic deformation is an important issue for copper parts under changing loads [21-23], this research work is carried out to numerically describe the mechanical behavior of thin copper layers in PCBs under cyclic thermal loading. As the copper layers used in PCBs are very thin, their testing under compression loads is particularly challenging. Hence, it is the first

major objective of this work to develop a testing method for cyclic tension-compression loading of thin layers. Therefore cyclic four-point bend tests and cyclic tension-compression tests are evaluated. Suitable specimens for both tests are developed. Since the thinnest copper layers used in PCBs are about 20 µm thick, they can only be loaded under compression loads if they are bonded to substrates. Layers in the same thickness as they are used in PCBs are tested, because thicker plates of copper show different material behavior and certain copper grades, e.g. galvanic copper, are not available in greater thicknesses. As substrate in the four point bend tests plates of silicone are used, in the cyclic tensile-compression tests layers of glass fiber reinforced epoxy resin (FR4-prepreg). This provides material input data for a Chaboche model of the copper. This model is implemented in the Finite Element Analysis (FEA) software Abaqus (Abaqus 6.12, Simulia, Daussault Systèmes, Providence, RI, USA) as the "nonlinear isotropic/kinematic hardening model" [24]; it can be used to describe the cyclic plasticity of copper. To be able to calculate the copper material properties from the experimental results, one must also know the material properties of the substrate. Thus an additional objective of this work is to determine the parameters for the hyperelastic material model [25] of silicone and to determine the anisotropic elastic properties of the FR4-prepreg. Silicone is characterized in tensile, biaxial and shear tests, the FR4-prepreg in tensile tests.

The kinematic and isotropic hardening behaviors are determined from the hysteretic force-strain curves obtained in the cyclic tension-compression tests. The employed "nonlinear isotropic/kinematic hardening model" is based on the research of Lemaitre and Chaboche [26, 27]. The kinematic hardening parameters are fitted in an optimization process using LS-Opt (LSTC, Livermore, CA, USA, 2011) with Abaqus as the solver. The overall backstress is defined as the sum of one backstress with linear evolution law and another with nonlinear evolution law. The linear one captures the ratcheting (accumulation of strains with cycles) behavior while the nonlinear one accounts for the curved shape of the hysteresis loops. The isotropic hardening variables are determined based on the stress against the plastic strain relationship that is constructed incrementally from the available individual cycles. No unique relationship can be found. Consequently, strain range memorization concepts, based on the work of Chaboche [28], are

considered. Since these approaches are developed for modelling strain-controlled tests, whereas the experimental data is obtained in a force-controlled way, a phenomenological mean stress memorization model is developed and implemented as an Abaqus User Subroutine. The developed material model is validated for non-isothermal cases based on curvature measurements of wafer bow samples subjected to thermal cycling. For these tests specimens consisting of silicon and copper are used.

For damage simulations, different PCB designs tested in the TCT are modeled using Abaqus. In these simulations the conditions of the TCT are applied and a stabilized loading cycle is obtained by using the phenomenological mean stress memorization model. Using this cycle the pore growth based on works of Rice, Tracy, Huang and others [29-32] is estimated. To this end the stress/strain states are exported from Abaqus and the estimation is done in a Matlab script (Matlab R2013b, Natick, MA, USA) to save computational time. Subsequently, electrical FEAs are conducted in Abaqus to obtain a correlation between the so-calculated pore volume fraction distributed over the structure and the electrical resistance increase. The results of the simulations are compared to experimental results to determine the necessary parameters for the pore growth models.

2. MATERIALS CHARACTERIZATION

In this section the experimental procedures to characterize thin copper layers under cyclic loads as well as the utilized numerical models are described. Furthermore the methodologies to determine the parameters for the employed numerical models are discussed. Copper layers in printed circuit boards are subjected to cyclical loads at different temperatures. It is also known that copper easily plastifies. Therefore, the experiments and numerical material models have been chosen such that they cover the full range of material response to realistic loads.

2.1 Experimental setup

In this section first the manufacturing of the specimens, then the testing of the individual materials (silicone, copper and FR4-prepregs) is described. Finally the cyclic testing of the composite specimens built of these materials is outlined. The cyclic four point bend tests are performed at room temperature only, thus also the silicone characterization is done only at 23°C.

Specimen manufacturing

For the silicone characterization ISO DIN EN 527 Type 5A [33] tensile test specimens (thickness 2 mm) are punched and Arcan-type shear test specimens (thickness 10 mm) are water jet cut. Figure 1 shows a sketch of the shear test

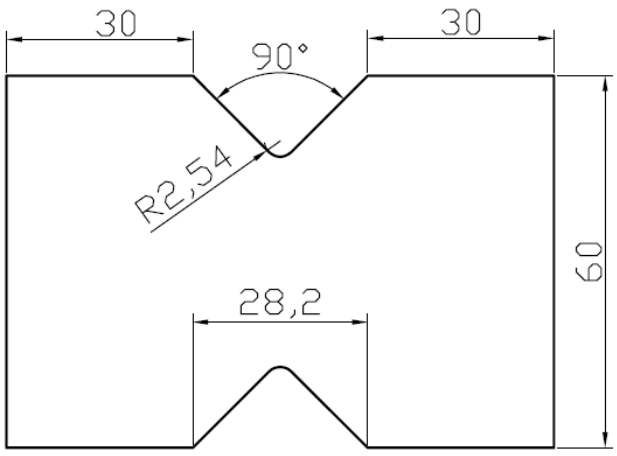

Fig. 1. Arcan-type specimen. All dimensions in mm.

specimen. These specimens and the associated testing methodology were originally proposed by Arcan [34-36]. For biaxial tests, slices of silicone with a diameter of 140 mm and a thickness of 2 mm are used. For the characterization of the FR4-prepreg and for the monotonic tensile tests of copper also ISO DIN EN 527 Type 5A [33] tensile test specimens (thickness 0.2 mm) are punched. As FR4-prepregs show orthotropic material behavior, specimens in 0°, 45° and 90° direction in the laminate plane are taken. For temperature dependent, dynamic-mechanical measurements of the copper foil strip-shaped specimens with the dimensions 40 x 5 x 0.018 mm^3 are used. To manufacture the specimens for the cyclic four point bend tests, the copper layers are bonded to 10 mm thick silicone plates, as shown in Figure 2. Silicone is chosen due to its high temperature resistance and low stiffness. Therefore the material response will be dominated by the copper. The specimens are 180 mm long and 40 mm broad. The copper foils are used as supplied, as so-called “resin coated foils” consisting of copper and epoxy resin. The epoxy side of these foils is bonded to the silicone blocks using an epoxy adhesive. The silicone blocks are treated in atmospheric plasma to increase their surface tension. Therefore it is possible to improve the quality of the bond between the silicone and the foils.

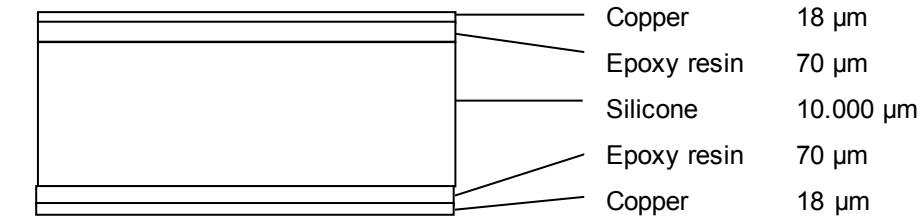

Fig. 2. Specimen for the cyclic four point bend tests

For the cyclic tensile-compression tests five layers of copper and four layers of glass fiber-reinforced (woven fabric) epoxy resin are pressed together in a compression molding process. This process is carried out under vacuum and at temperatures up to 190°C. For these specimens thicker copper foils (~60 µm)

were used (a micrograph and a photo are shown in Figure 3). The FR4-prepreg is used because of its stiffness, which is high enough for the cyclic tensile-compression tests but does not dominate the material response. To avoid failure in the fixture doublers made of FR4-prepreg are bonded to the specimens using an epoxy adhesive. The specimens are 50 mm long and 18 mm broad. The gauge length is only 5 mm in order to avoid buckling. Hence for the tensile-compression tests five layers of copper are used, while for the cyclic four point bend tests only two layers are necessary. This is especially interesting for copper types which cannot be manufactured in greater amounts, for example galvanic copper. For the curvature measurements a bimaterial composite consisting of a thin copper film

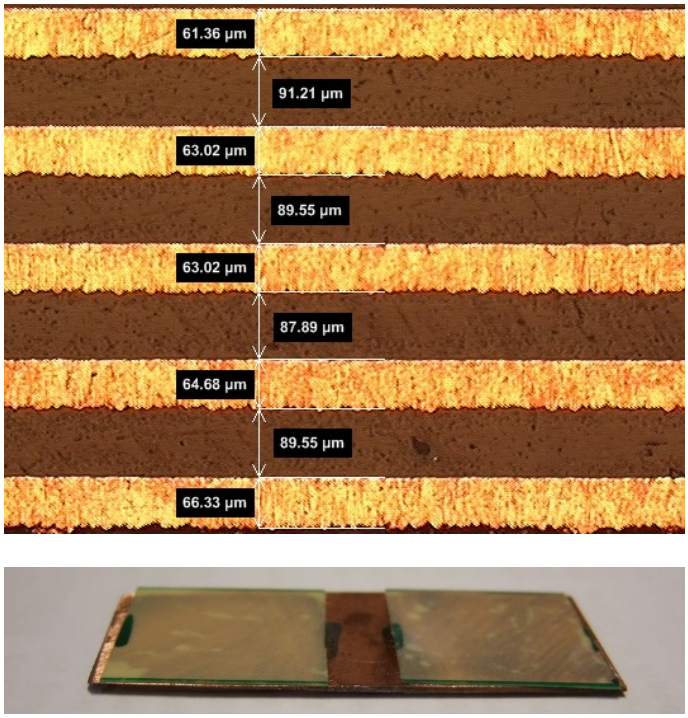

Fig. 3. Specimen for the cyclic tensile-compression tests.

sputtered onto a silicon substrate are produced. The specimens consist of a 20 µm-thick copper layer electrodeposited on a 700 µm-thick (100) silicon wafer (300 mm diameter).

Individual materials characterization

Silicone

Silicone is used as a substrate for copper in the four point bend tests. In order to determine material input parameters for a hyperelastic material model, tensile,

biaxial and pure shear tests are conducted. The silicone grade is characterized in tensile tests on a Zwick Z010 tensile testing machine (Zwick GmbH & Co. KG, Ulm, Germany) with a testing speed of 5 mm/min. These tests are conducted based on the standard DIN EN ISO 527. The tensile test is shown in Figure 4 (left). Shear tests are conducted using “V-Notched Rail Shear Tests”, similar to the one described in [37]. The corresponding device is installed on a Zwick Z250 tensile testing machine (Zwick GmbH & Co. KG, Ulm, Germany) using pneumatic clamping jaws. The shear testing device is shown in Figure 4 (right). The testing speed is also 5mm/min. The shear stress τ at a given applied load F was calculated by the expression (equation 1)

$$\tau = \frac{\mathrm{F}}{A_s} \tag{1}$$

in which A_s is the cross section between the two notch tips. In both tests the strains are measured by the ARAMIS-System, a digital image correlation system by Gesellschaft für optische Messtechnik (GOM), Germany. The ARAMIS-System is shown in Figure 4 (left) in front of the tensile testing machine. Biaxial tests are conducted using a blow-up testing device. This device is shown in Figure 5; it was constructed at the Polymer Competence Center Leoben [38]. The specimens, slices of silicone, are clamped in the device and pressurized using compressed

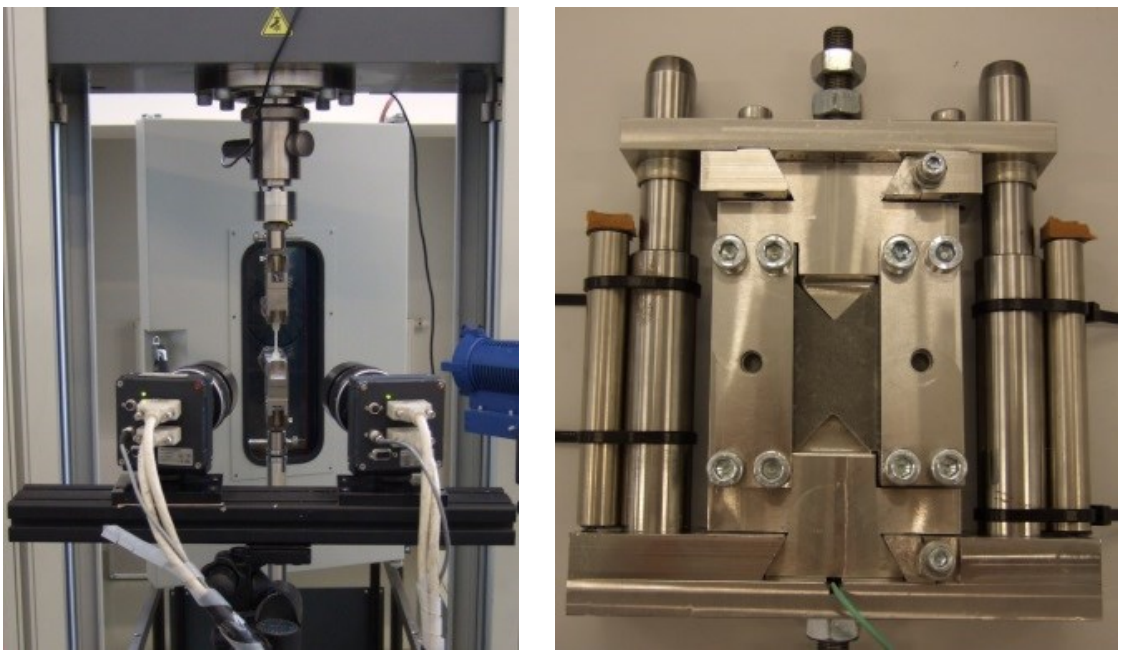

Fig. 4. Left: Tensile test, Right: Shear test.

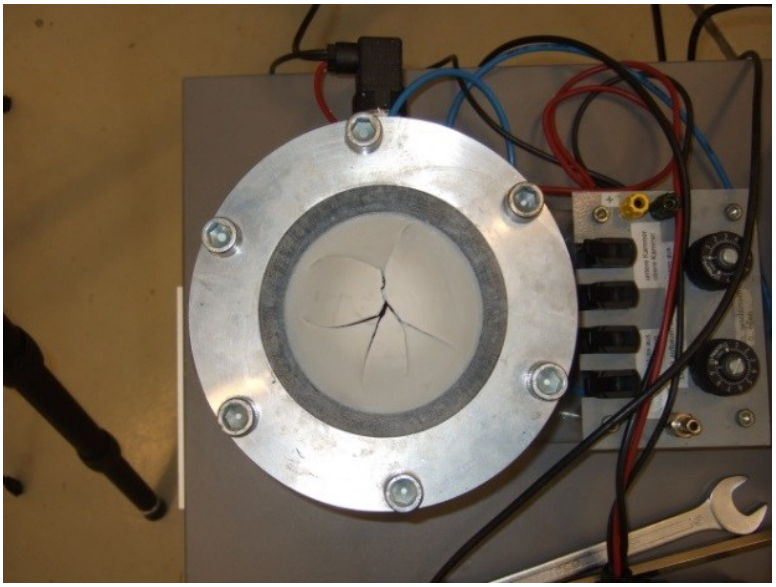

Fig. 5. Blow up testing device with tested specimen.

air. The pressure signal is recorded and the occurring strain is measured by the ARAMIS-System. Blow-up tests are carried out at room temperature. Data reduction is conducted as described in [39]. In all tests four specimens are tested. Based on the experimental data of these three types of tests, hyperelastic material parameters for a third order Ogden model [25] are determined using the built in "Evaluate"-function in the FEA software Abaqus.

Copper and FR4-prepreg

Copper is characterized in tensile tests at room temperature on an Instron 5500 (Instron Limited, Massachusetts, USA) tensile testing machine. Five specimens are tested and the occurring strains are measured using the ARAMIS-System. Additionally, the temperature-dependent elastic properties of the copper foil are measured dynamically by means of a micro-Dynamic Mechanical Analyzer (model µ-DMA RSAG2, Texas Instruments, New Castle, USA). The specimens are loaded with a deformation amplitude of 0.02% and with a frequency of 1Hz. The considered temperature range is between room temperature and 150°C.

The FR4-prepreg is characterized in tensile tests on a Zwick Z250 tensile testing machine at 23°C, 85°C and 145°C. These tests are conducted in the same way as the tensile tests of copper. Hence also the temperature-dependent plastic properties of the material can be determined. As the FR4-prepreg is a thin layer, only the mechanical properties in the laminate plane can be measured and the

missing properties have to be calculated by micromechanics simulations. For them the software digimat-MF (digimat-MF 4.4.1, e-Xstream engineering SA, Louvain-la-Neuve, Belgium) is employed. The mean-field homogenization method based on Mori–Tanaka [40,41] is used. The reinforcing glass fibers are represented as a woven microstructure [42], fiber and matrix are modeled linear elastically. The properties of the pure resin are back-calculated from the in-plane measurements, the glass fiber properties are taken from the literature [43]. To be able to describe the elastic-plastic properties in-plane, three directions, 0°, 45° and 90° are characterized. In each direction four specimens are tested. These measurements and the corresponding simulations are described in detail in [44]. The coefficients of thermal expansion of copper and prepreg needed for the simulations performed in this thesis were determined in former work [45].

Cyclic composite tests

Cyclic four point bending tests

The four point bending equipment is shown in Figure 6. The support length is 137 mm; the length of the loading span is 64 mm. Rollers of polyoxymethylene (POM) are used as bearings, due to their low coefficient of friction. The four point bending equipment is used in a Bose 3230 Electro Force (Bose Corp,

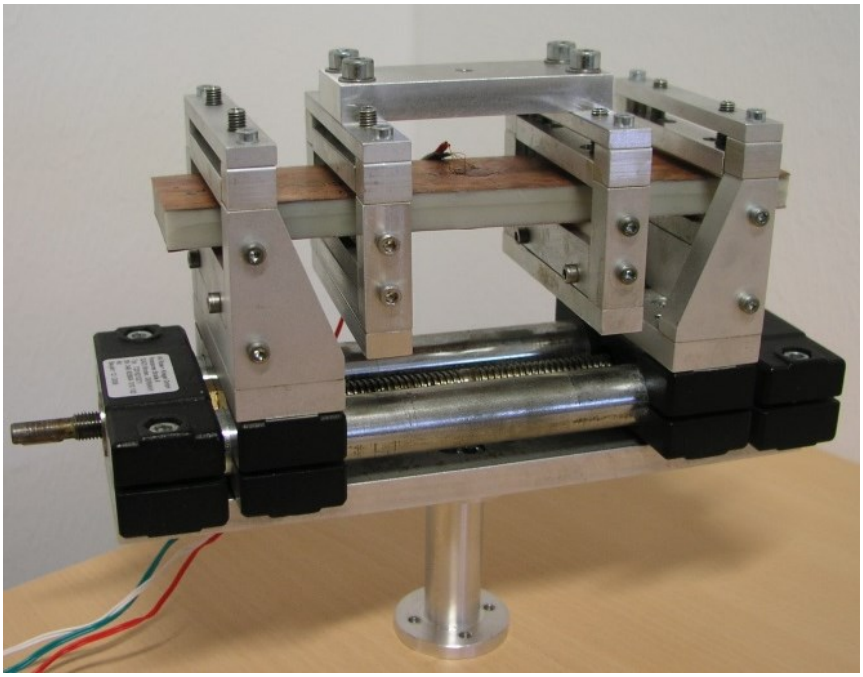

Fig. 6. Four point bending equipment with specimen.

Framingham, MA, USA) testing machine. Tests are carried out in a displacement-controlled way. A sinusoidal waveform is chosen for the actuator displacement. The upper and lower limits of the sine and the R-ratios are listed in Table 1. All experiments are performed at room temperature. The circular frequency of the sine is varied depending on the amplitude in order to keep the strain rate constant. During the tests the strains are recorded using strain gauges, which have been attached to the middle of the upper specimen surface. Forces and displacements are recorded by the Bose 3230 sensors. For better interpretation and understanding of the test results, a two-dimensional FEA model of the cyclic four point bend tests is created. For this model the FEA software Abaqus is used with 8-node biquadratic plane stress quadrilateral elements (Abaqus name: CPS8R). Figure 7 shows the model. For the sake of better visibility, only half of the specimen is depicted. Due to the low thickness of the copper foil and the epoxy layer, see Figure 2, the corresponding regions are meshed finer. The copper parts are shown in gold, epoxy resin parts in black, the silicone in blue. The fixture is modeled as a rigid body, between fixture and specimen a frictional contact with an assumed frictional coefficient of 0.2 is implemented. This value is chosen because

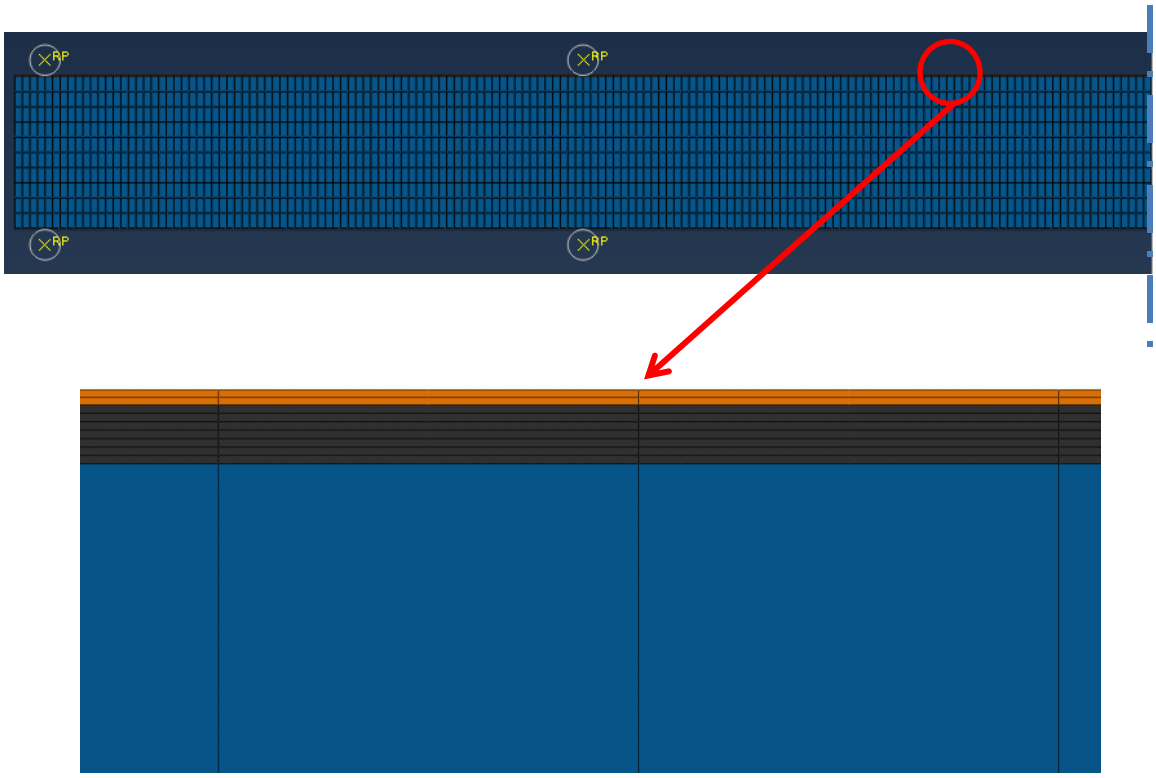

Figure 7: Meshed model of the cyclic four point bending test.

the frictional coefficient between metals and POM is known to be low [46]. At the reference points (see 'RP' in Figure 7) the actuator displacements are applied.

Table 1. Amplitudes, R-ratios and circular frequencies.

Upper limit [mm]	1	2	1	5
Lower limit [mm]	-1	-2	-2	-5
R-ratio [-]	-1	-1	-2	-1
Circular frequency [rad/s]	5	2.5	3.33	1

Cyclic tension-compression tests

The equipment for these tests is shown in Figure 8. It is used in a MTS 810-22 testing machine for the experiments at room temperature (RT) and in a MTS 831 (MTS, Eden Prairie, MN, USA) testing machine for the experiments at higher temperatures (85°C, 145°C). The gauge length is 5 mm and the occurring strains are measured by the ARAMIS-System while the forces are recorded by the

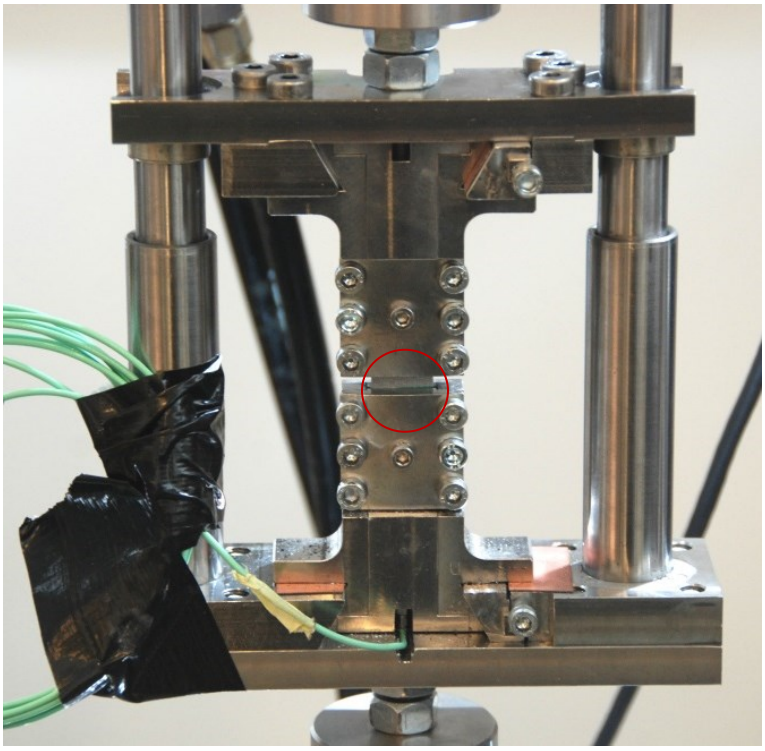

Fig. 8. Testing device with specimen (inside red circle).

MTS 810-22 sensors. Using the ARAMIS system, four hysteresis loops (25 frames per hysteresis loop) are recorded in immediate succession. This is called "measuring phase". In total, the recording program includes four measuring

phases and three recording pauses between the measuring phases; it covers the whole testing time. As the specimen is a composite specimen, see Figure 3, many different modes of failure initiation during the cyclic testing are possible. The tests are carried out force-controlled, which is considered to be more accurate than displacement-control, because of the rather complex testing setup and the small displacements. A sinusoidal waveform is chosen for the force signal. The load cases tested in the cyclic tension-compression test are listed in Table 2. The force limits are reduced at higher temperatures to account for the lower material strength. Three specimens are measured per load case. The circular frequency of the sine is varied depending on the amplitude in order to keep the strain rate constant.

Table 2: Loading cases in the cyclic tension-compression test

R-ratio [-]	-0.25	-0.3	-0.33	-0.5	-0.89	-1	T. [°C]
Upper force limit [N]	2000	2000	-	2000	1800	1600	23
Lower fower limit [N]	-500	-600	-	-1000	-1600	-1600	
Upper force limit [N]	-	1800	1620	1800	1620	1600	85
Lower fower limit [N]	-	-540	-540	-900	-1440	-1600	
Upper force limit [N]	-	1400	1260	1400	1260	1260	145
Lower fower limit [N]	-	-420	-420	-700	-1120	-1260	

2.2 Experimental results

In this section all the stresses are true stresses; all the strains are engineering strains. This strain measure is used, as all measured strains are in the small strain regime, except for the ones in silicone, which was not used in the final built-up.

Individual materials characterization

Silicone

The silicone test curves are shown in Figure 9. The curves differ due to different types of load. Furthermore, the strain rates differ due to the different geometries of the specimen and the nature of the load. While the tensile and the shear tests are both conducted with a testing speed of 5 mm per minute, in the biaxial test the testing pressure is applied and held constant during the testing time. In all three tests the curve shape is as expected. Based on this experimental data, the

following material parameters for a third order Ogden material model are determined (see Table 3). The integer i is a counting parameter, μ_{Odgen}, α_{Ogden} and D_{Ogden} are material parameters. In a third order Odgen model the strain energy potential U_s is (equation 2)

$$U_S = \sum_{i=1}^{3} \frac{2\mu_{Ogden\ i}}{\alpha_{Odgen\ i}^2} \left(\bar{\lambda}_1^{\alpha_{Odgen\ i}} + \bar{\lambda}_2^{\alpha_{Odgen\ i}} + \bar{\lambda}_3^{\alpha_{Odgen\ i}} - 3\right) + \sum_{i=1}^{3} \frac{1}{D_{Ogden\ i}} (J_{el} - 1)^{2i} \quad (2)$$

Here J_{el} is the elastic volume strain, $\bar{\lambda}_1$, $\bar{\lambda}_2$ and $\bar{\lambda}_3$ are normalized principal stretches which are derived from the principal stretches λ_1, λ_2 and λ_3 by equation 3. J_{tot} stands for the total volume strain.

$$\bar{\lambda}_i = {J_{tot}}^{-1/3} \lambda_i \quad (3)$$

From the strain energy potential U_S and the strain tensor the stresses in the material can be derived. The model is described in detail in [24].

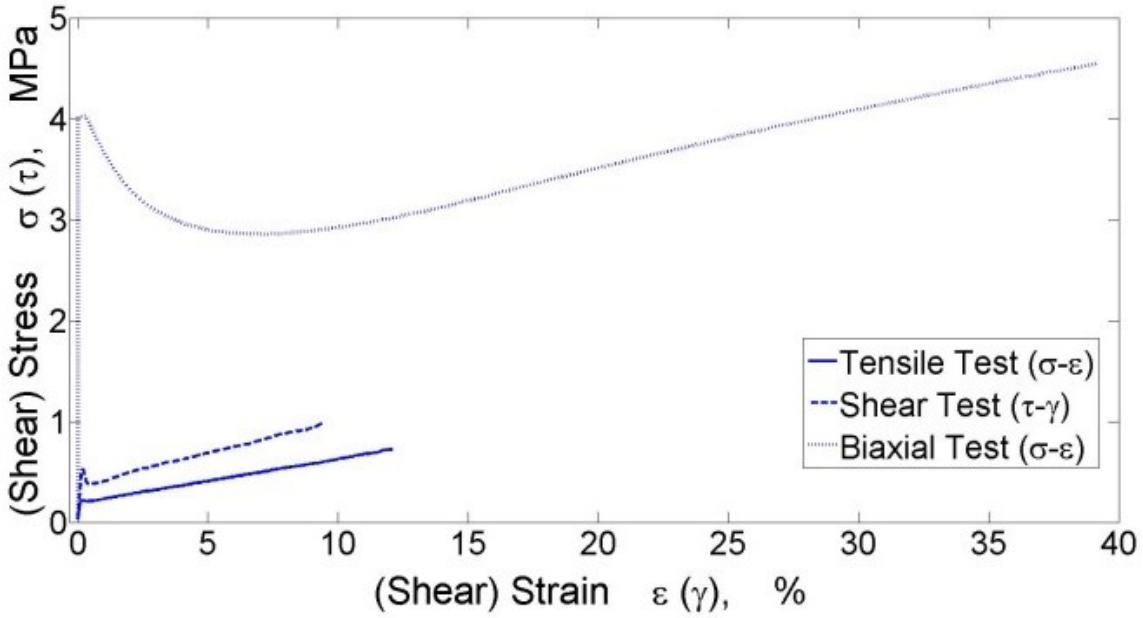

Fig. 9: Silicone test curves

Table 3: Material parameters for a third order Ogden material model of silicone.

i	μ_{Odgen} (i) [MPa]	α_{Ogden} (i) [-]	D_{Ogden}(i) [1/MPa]
1	29.98	5.848	0.1059
2	-27.30	6.900	0
3	0.08947	-12.73	0

Copper

A stress-strain curve of the copper grade is shown in Figure 10. The curve has the expected shape [47]. The elastic properties are listed in Table 4 as a function of temperature. Since it is not possible to measure the Poisson's ratio with the DMA and the tensile tests showed large scatters concerning Poisson's ratio literature data [48] are used. The coefficient of thermal expansion can be found in [45].

Table 4: Elastic properties of copper foil

T [°C]	Young's modulus E [GPa]	Poisson's ratio υ [-]
20	91.8	0.34
50	89.8	0.34
100	85.8	0.34
150	80.8	0.34

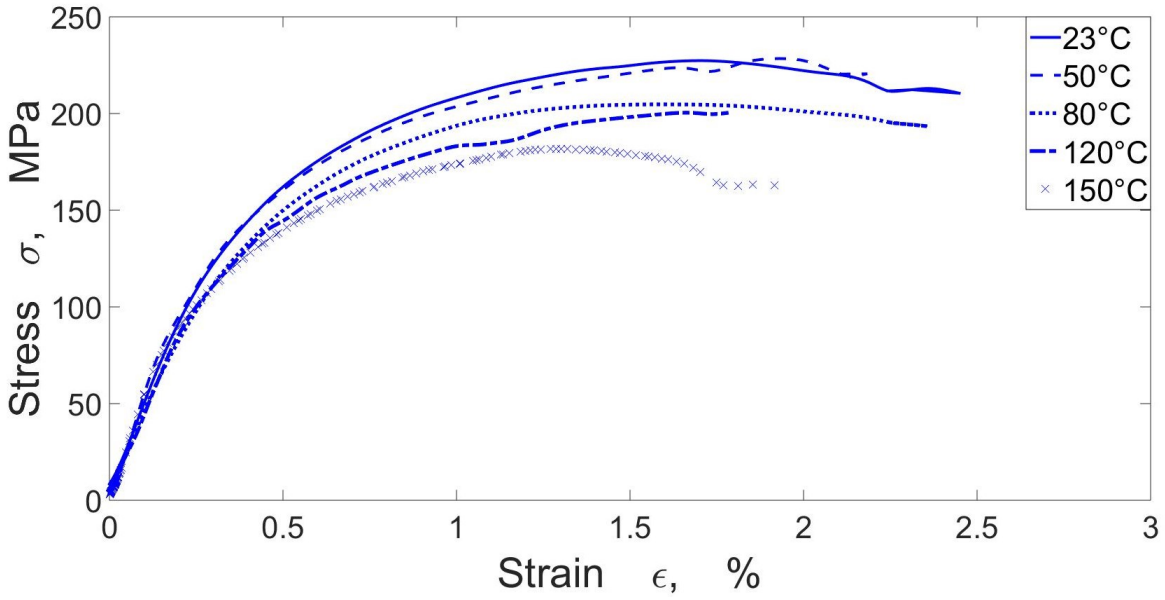

Fig. 10: Flow curve of copper.

FR4-Prepreg

The elastic properties [44] of the used FR4-prepreg are given in Table 5. Direction 1 means warp direction (0° in plane), direction 2 means fill direction (90° in plane) and direction 3 means out-of-plane direction. E stands for the Young's Modulus, v for the Poisson's Ratio and G for the shear modulus. These results seem plausible, as higher fiber content increases material stiffness and the fiber content in the warp direction is higher than that in the fill direction. In the out-of-

plane direction there are no fibers at all. Temperature-dependent elastic properties as well as the coefficients of thermal expansion can be found in [45]. To the readers convenience they are reprinted in Figure 12. Figure 11 depicts the stress versus plastic strain curve of the FR-4 prepreg in direction 2, i.e. the loading direction in the cyclic tension-compression tests. The curves at 85°C and at 145°C are very similar, the material behavior seems to be dominated by the glass fiber at both temperatures.

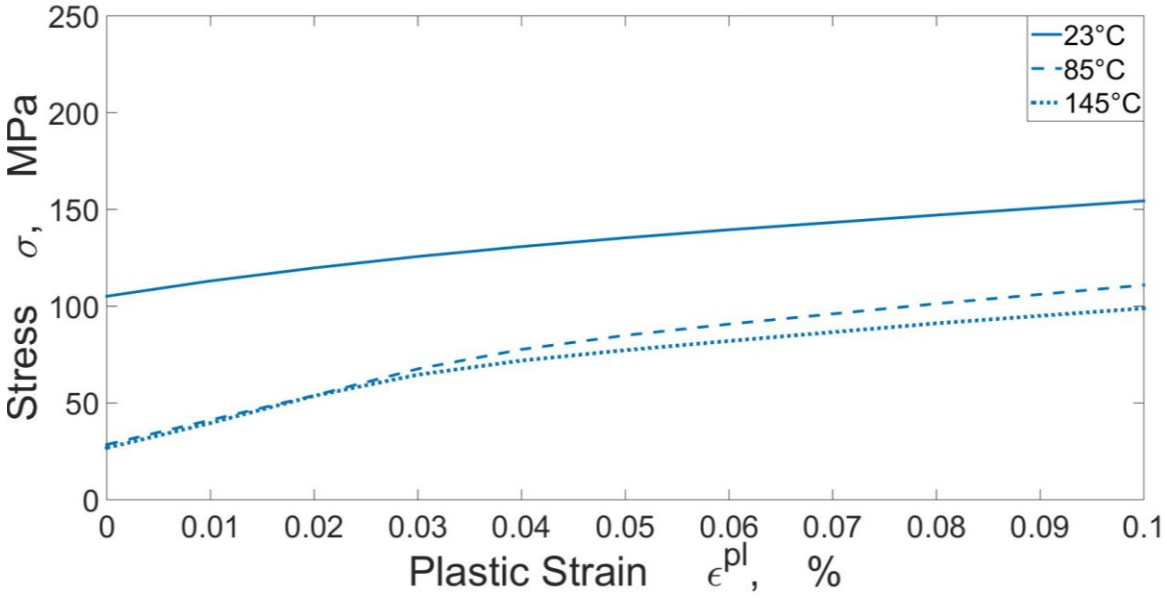

Fig. 11. Stress versus plastic strain curve of the FR4-prepreg in direction 2.

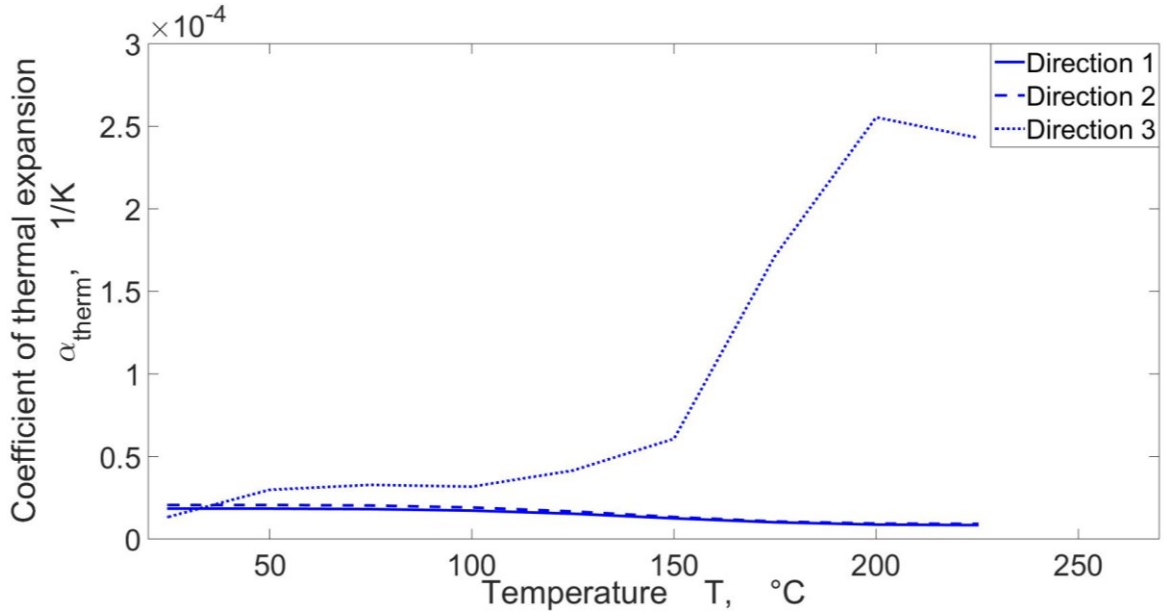

Fig. 12. Coefficients of thermal expansion.

Table 5: Elastic properties of the FR4-prepreg at room temperature.

E_1 [MPa]	E_2 [MPa]	E_3 [MPa]	ν_{12} [-]	ν_{13} [-]	ν_{23} [-]	G_{12} [MPa]	G_{13} [MPa]	G_{23} [MPa]
16757	15086	9455	0,16	0,33	0,34	3548	3445	3416

Cyclic composite tests

Cyclic four point bending tests

Hysteresis curves of the copper-silicone composite specimens are obtained using the cyclic four point bend tests. Figure 13 shows stabilized hysteresis loops measured on samples at symmetrical amplitude of 2 mm and of 5 mm. As after a certain testing time there is no change in the shape of the hysteresis loops anymore, these loops can be regarded as “stabilized”. The corresponding strain versus time signals from the strain gauges are shown in Figures 14 and 15. The hysteresis at an amplitude of 2 mm in Figure 13 does not have the typical shape of a plastic hysteresis curve (plastic hysteresis curves are shown in Figures 18 to 24) and the strains in Figure 14 are between -1000 με and 1000 με, which is inside the linear-elastic regime of the examined copper according to tensile tests. Figures 13 and 15 show the stabilized force-displacement curve and the corresponding strain signal measured on a sample at symmetrical amplitude of 5 mm. Due to the

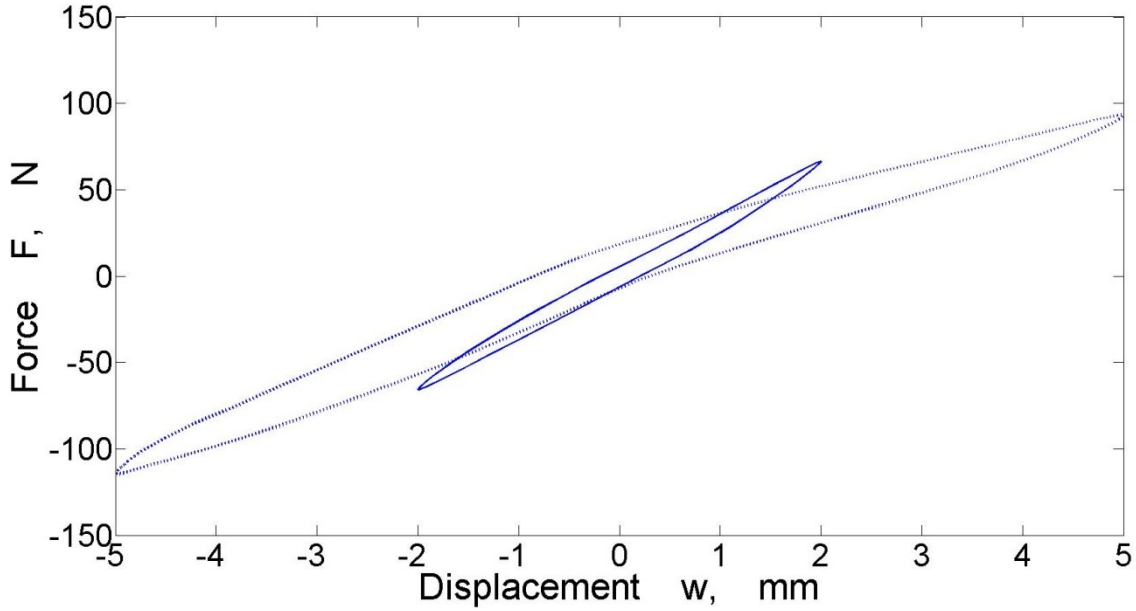

Fig. 13. Stabilized force-displacement curve at amplitudes of 2 mm and 5 mm.

low stiffness of the silicone, the bearings are pressed into the silicone during the testing. As a result, at higher deflections failure occurs at one of the bearings at a low number of cycles. The stresses and strains occurring at the bearings cannot be measured. As failure already occurs after a few cycles only neither the force-displacement curve nor the strain signal are symmetrical anymore. The strains in Figure 15 show that the lower copper layer has already failed, while the upper the

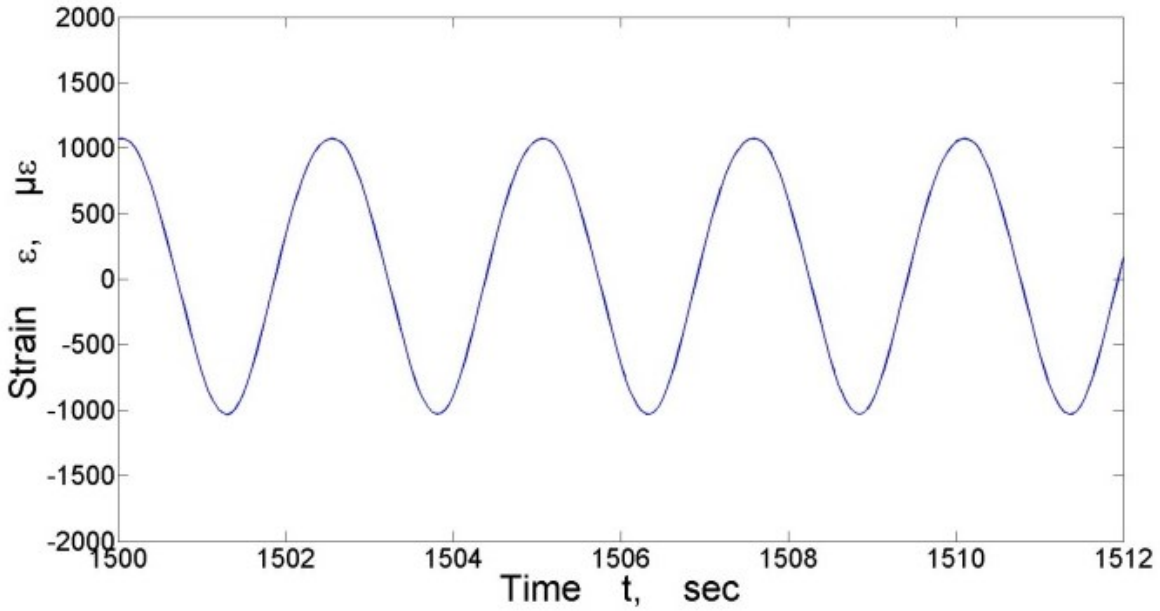

Fig. 14. Strain versus time, Amplitude 2 mm.

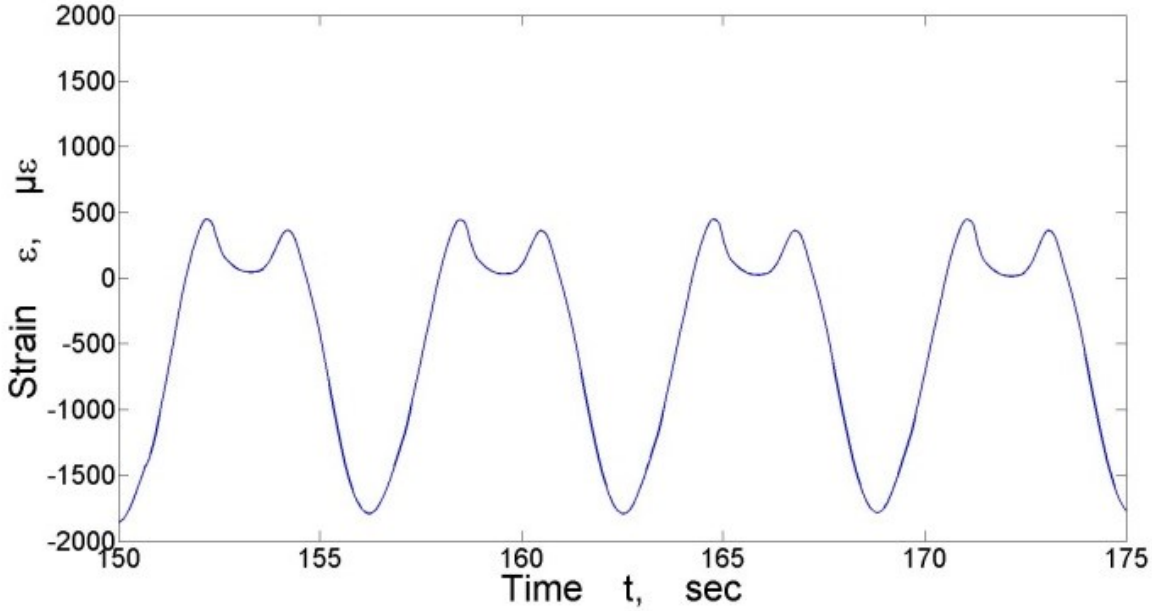

Fig. 15. Strain versus time, Amplitude 5 mm.

layer is still intact. The hysteresis in Figure 13 (Amplitude 5 mm) is flattened on corresponding side for that reason. Thus these measurements cannot be used to determine material parameters. Besides, only small strains can be transmitted by the silicone to the copper layers due to its hyperelastic material behavior. Figures 16 and 17 show the bending line of a copper-silicone composite specimen in a four point bend test. The results shown in Figure 16 are based on a linear-elastic material model (Young's Modulus E=50 MPa, Poisson's Ratio v=0.45) used for silicone, while the results in Figure 17 have been calculated

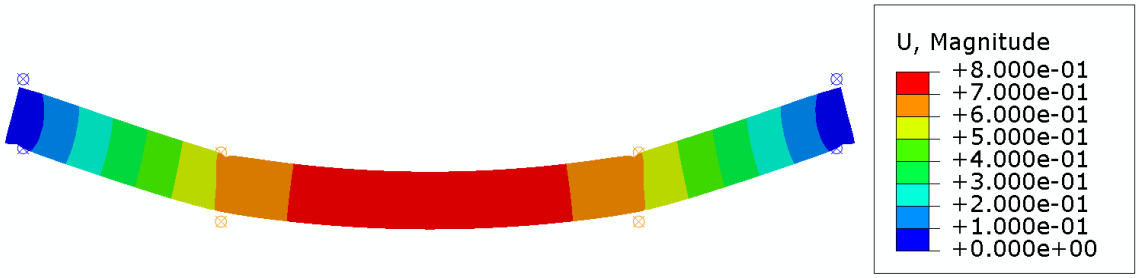

Fig. 16. Linear-elastic bending line (Abaqus).

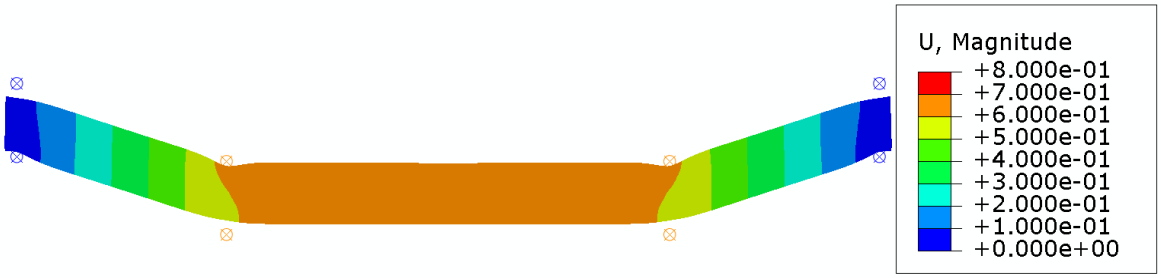

Fig. 17. Hyperelastic bending line (Abaqus).

employing a hyperelastic Ogden material model for silicone, see Table 3. In the linear-elastic case a classic bending line appears, while in the hyperelastic case the deflection is nearly constant in the middle region (loading span) of the specimen. Since bending strains are proportional to the second derivative of the deflection [49], the strains in the copper layers are much smaller in the hyperelastic case.

Consequently, due to the low stiffness and the hyperelastic material behavior of the silicone, this methodology is applicable only for small strains.

Cyclic tension-compression tests

In these tests hysteresis curves of the copper-FR4-prepreg composite specimens are obtained. The thermal and mechanical material properties of the FR4-prepreg were determined in [45]. These properties need to be known in order to be able to extract the copper material behavior from the composite specimen behavior. In Figure 18 stabilized hysteresis loops measured at room temperature, R-ratio equals -1, are shown. In the following figures the number of elapsed cycles is given and also the number of cycles to failure (N_f), because the hysteresis at $N_f/2$ is often used for lifetime estimation. Failure is detected when the specimen is no longer able to transmit tensile loads. During the testing many different failure modes occur, inside the gauge length as well as in the fixture. As a result, the number of cycles to failure scatters extremely. Moreover this number does not represent the copper material behavior alone, but also the interface between copper and FR-4 prepreg and the influence of the fixture. Hence it must be ensured that the hysteresis loops have actually stabilized by inspecting foregoing and subsequent loops. If after a certain shakedown period there is no change in the shape of the hysteresis loops anymore, they can be regarded as “stabilized”.

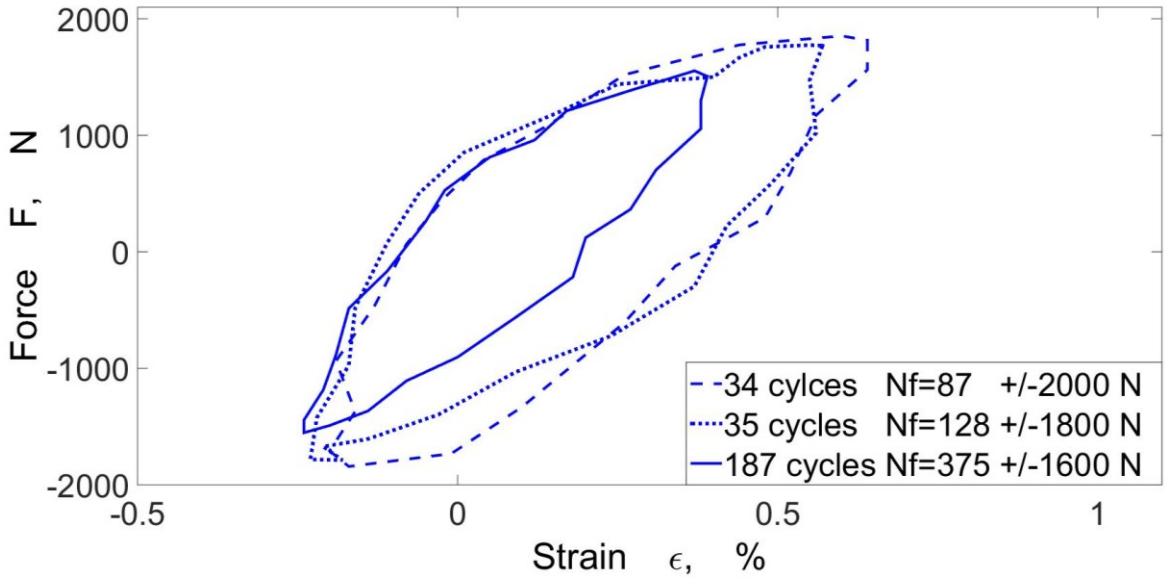

Fig. 18. Stabilized force-strain curves, R=-1, the loads are given in the legend.

Although the force- controlled loading conditions of the curves shown in Figure 18 are symmetrical, the strains are generally not symmetrical. This is due to the loading condition in the first loading cycle and due to the plastic material behavior.

As the specimen has been loaded in tensile direction before it is loaded in compression direction, the first part of the compression loading period is used to reset the plastic tensile strain. This is illustrated in Figure 19; the graph shows the

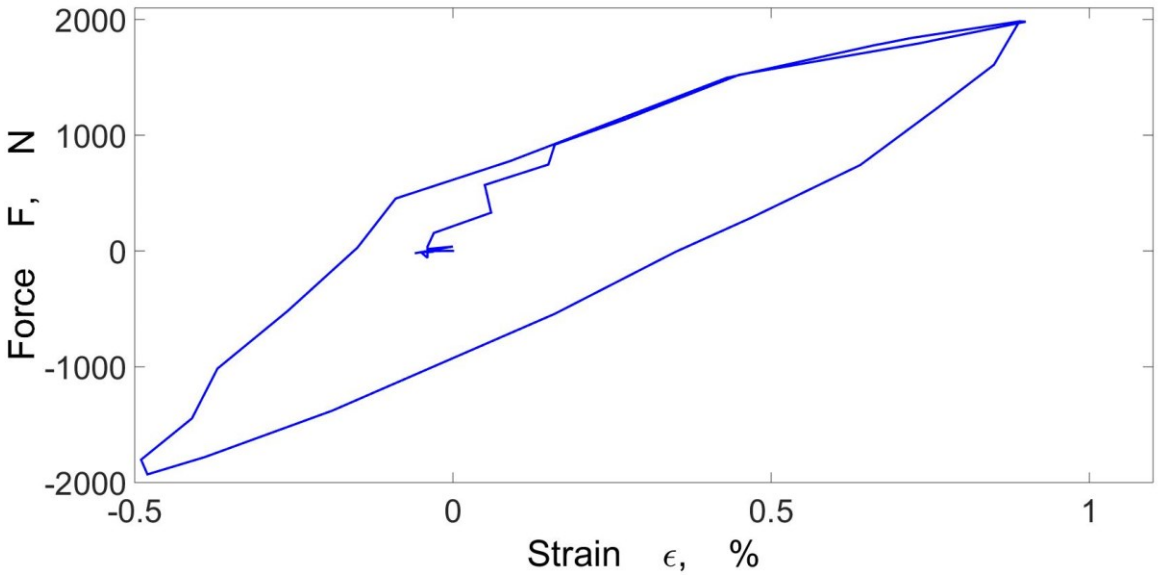

Fig. 19. Initial force-strain curve, R=-1

initial hysteresis of a specimen under symmetrical load. When the load is reversed to its minimum, the strain reaches only about half of its maximum in tension, because of the plastic material behavior. Since the loading is symmetrical, no ratcheting will take place. Figure 20 shows stabilized hysteresis loops under different sinusoidal loading conditions. Because of different mean stresses, ratcheting occurs to different degrees, so that the curve with the highest mean stress also shows the highest mean strain. All amplitudes listed in Table 2 were tested successfully. Figures 21 and 22 show the corresponding hysteresis loops obtained at testing temperatures 85°C and 145°C, at an R-ratio of -1. The strains shown in all following figures are caused by the mechanical loading. Thermal strains are not measured, because the recording of the heating-up is not possible with the ARAMIS-System. Hence, the digital image correlation measurements starts when the specimens are heated through, but still free of mechanical load. Again, the curves show asymmetry with respect to the zero-strain line, although the loading is symmetric, because the first loading cycle starts in tensile direction which shifts the entire hysteresis loop to the right. Hence, there residual tensile plastic strains develop. This effect is observed at all tested temperatures, but

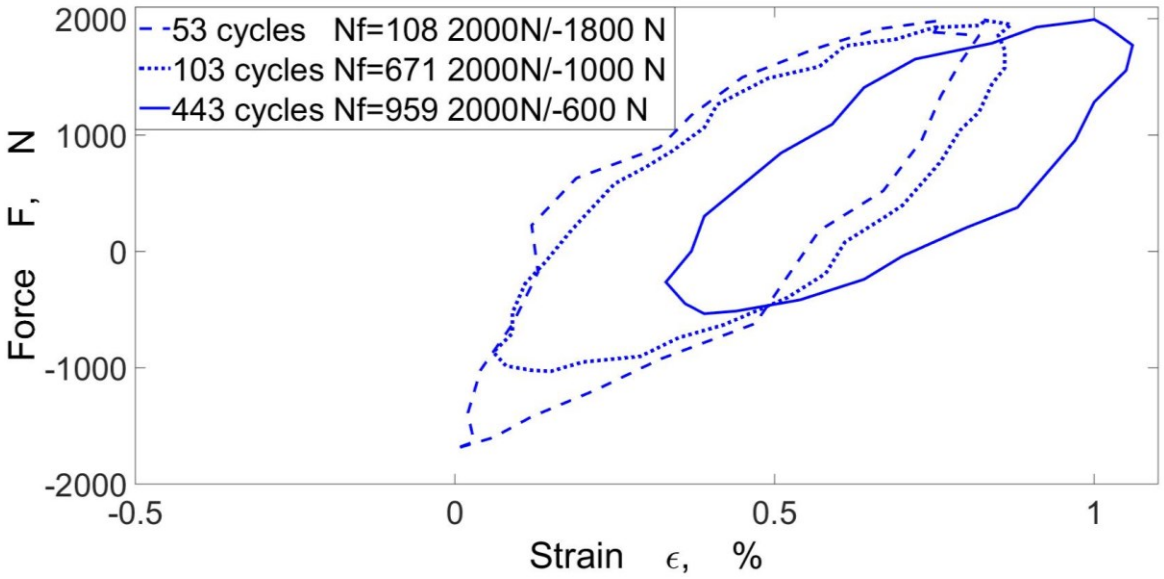

Fig. 20. Stabilized force-strain curves, asymmetric loading, room temperature. The loads are given in the legend.

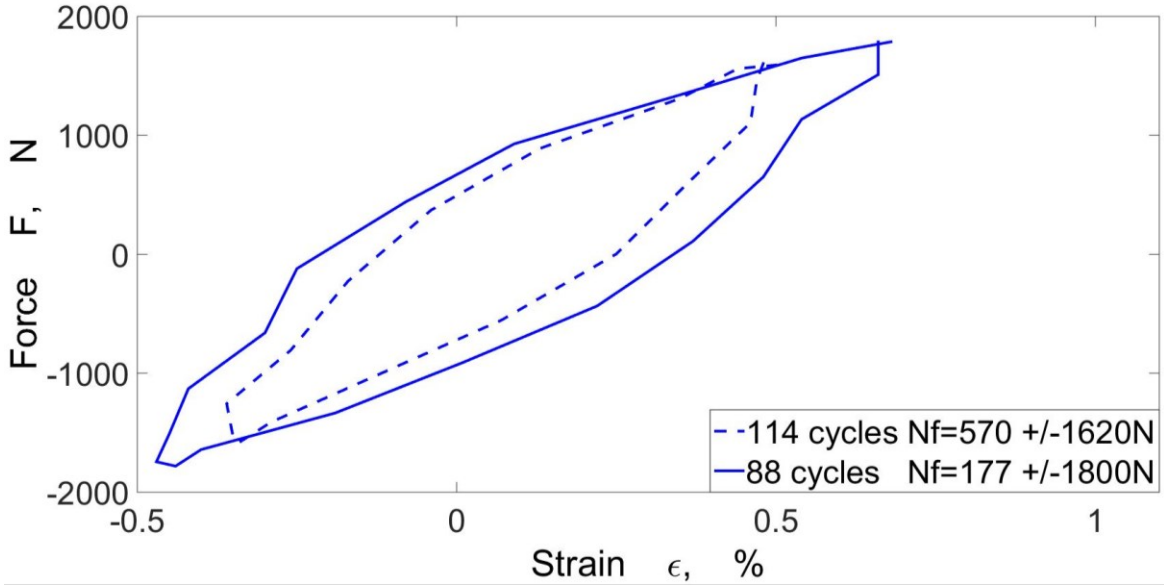

Fig. 21: Stabilized force-strain curves, R= -1, testing temperature 85°C

increases with temperature due to the lower material stiffness at higher temperatures. It also increases with higher loads, leading to higher plastic strains, as the different mean strains in the Figures 21 and 22 indicate. Figures 23 and 24 show the material response of composite specimens subjected to asymmetric loading conditions. The force limits are given in the figures. Although the loading is reduced at higher temperatures keeping the R-ratios constant at all testing temperatures (see Table 2), the curves measured at 145°C show higher mean

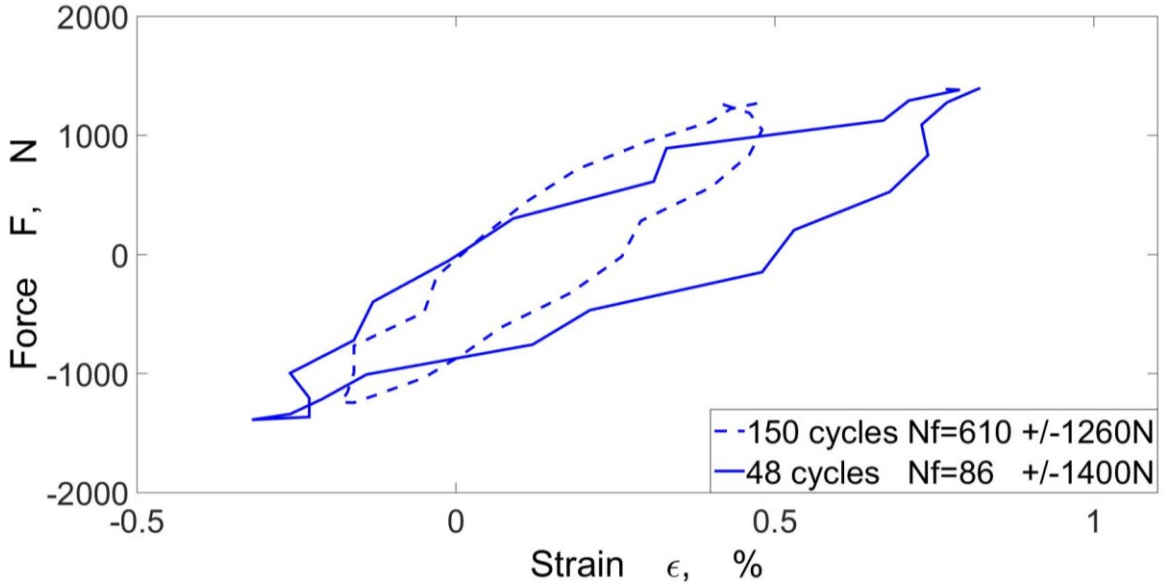

Fig. 22: Stabilized force-strain curves, R= -1, testing temperature 145°C

strains than the ones measured at 85°C. This effect can be explained with reduced yield stresses at higher temperatures and hence greater mean strains created by the loading of the cyclic test. In general, the recording of smooth hysteresis loops at 145°C is more difficult than at 85°C or at room temperature, because the window pane of the climate chamber of the MTS 831 testing machine foggs up considerably. Therefore, at higher temperatures larger measuring tolerances are admitted in the optical strain measurements.

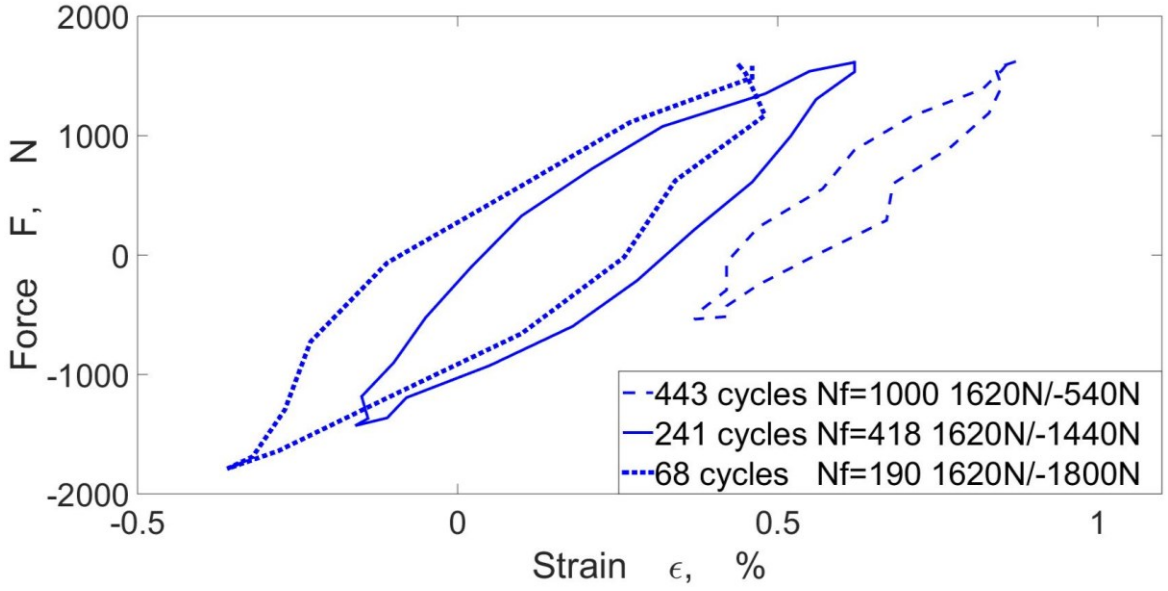

Fig. 23: Stabilized force-strain curves, asymmetric loading, testing temp. 85°C

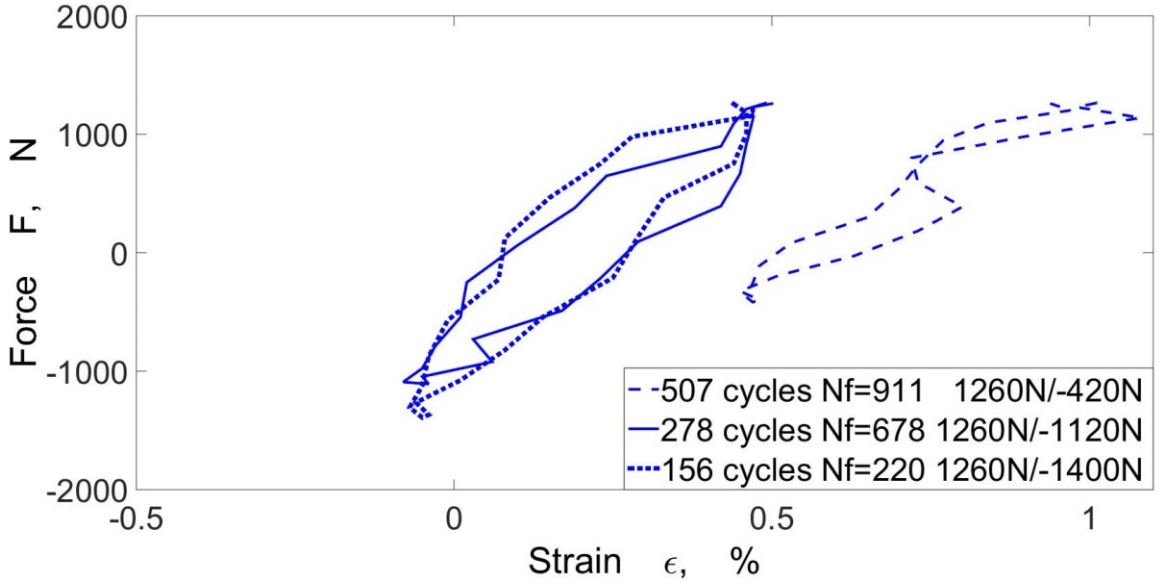

Fig. 24: Stabilized force-strain curves, asymmetric loading, testing temp. 145°C

2.3 Numerical models

For numerically modeling the observed material behavior the "nonlinear isotropic/kinematic hardening model" implemented in Abaqus [24] is used. It is based on the work of Lemaitre and Chaboche [26,27] and can reproduce the behavior of metals subjected to cyclic loading. In this implementation and assuming a small strain framework, the total strain rate $\dot{\boldsymbol{\varepsilon}}$ is written as the sum of the elastic $\dot{\boldsymbol{\varepsilon}}^{\mathrm{el}}$ and the plastic $\dot{\boldsymbol{\varepsilon}}^{\mathrm{pl}}$ strain rate tensor (equation 4).

$$\dot{\boldsymbol{\varepsilon}} = \dot{\boldsymbol{\varepsilon}}^{\mathrm{el}} + \dot{\boldsymbol{\varepsilon}}^{\mathrm{pl}} \tag{4}$$

For $\boldsymbol{\varepsilon}^{\mathrm{el}}$ linear elasticity is assumed following Hooke's law (equation 5), where **D** stands for the fourth order elasticity tensor and $\boldsymbol{\sigma}$ for the stress tensor. : is the double dot product.

$$\boldsymbol{\sigma} = \mathbf{D} : \boldsymbol{\varepsilon} \tag{5}$$

The plastic behavior is described with classical concepts; equation 6 defines the yield surface F_Y. In this equation σ^0 gives the radius of the yield surface and $\mathrm{J}(\boldsymbol{\sigma} - \boldsymbol{\alpha})$ is calculated for Mises plasticity as follows:

$$F_Y = \mathrm{J}(\boldsymbol{\sigma} - \boldsymbol{\alpha}) - \sigma^0 = 0 \quad \text{with} \quad \mathrm{J}(\boldsymbol{\sigma} - \boldsymbol{\alpha}) = \sqrt{\frac{3}{2}(\mathbf{S} - \boldsymbol{\alpha}) : (\mathbf{S} - \boldsymbol{\alpha})}. \tag{6}$$

Here **α** means the backstress tensor and **S** the deviatoric stress tensor. This model uses associated plastic flow, so the rate of plastic flow $\dot{\boldsymbol{\varepsilon}}^{pl}$ is given by (equation 7)

$$\dot{\boldsymbol{\varepsilon}}^{pl} = \frac{\partial F_Y}{\partial \boldsymbol{\sigma}} \dot{\bar{\varepsilon}}^{pl} \qquad \text{with} \qquad \dot{\bar{\varepsilon}}^{pl} = \sqrt{\frac{2}{3} \dot{\boldsymbol{\varepsilon}}^{pl} : \dot{\boldsymbol{\varepsilon}}^{pl}} \tag{7}$$

The evolution law of the k[th] backstress $\boldsymbol{\alpha}_k$ is given by (equation 8)

$$\dot{\boldsymbol{\alpha}}_k = C_k \frac{1}{\sigma^0} (\boldsymbol{\sigma} - \boldsymbol{\alpha}) \dot{\bar{\varepsilon}}^{pl} - \gamma_k \boldsymbol{\alpha}_k \dot{\bar{\varepsilon}}^{pl} + \frac{1}{C_k} \boldsymbol{\alpha}_k \frac{dC_k}{dT}. \tag{8}$$

The overall backstress **α** is calculated as the sum of all backstresses $\boldsymbol{\alpha}_k$. C_k and γ_k are material parameters, T is the temperature. The size of the yield surface σ^0 depends on the equivalent plastic strain $\bar{\varepsilon}^{pl}$. Equation 9 shows the differential (left) and integral (right) form of this relationship, $\sigma|_0$ is the initial size of the yield surface, Q and b are material parameters.

$$\dot{\sigma^0} = b(Q - \sigma^0) \dot{\bar{\varepsilon}}^{pl} \quad => \quad \sigma^0 = \sigma|_0 + Q_\infty \left(1 - e^{-b\bar{\varepsilon}^{pl}}\right) \quad \text{with } Q_\infty = Q - \sigma|_0 \tag{9}$$

As this function may depend on the loading situation, Chaboche et al. [28] proposed to add an additional inner variable q to the model, which changes the value of the material parameter Q (equation 10)

$$dQ = 2\mu(Q_S - Q)dq \tag{10}$$

Q_S and μ are material parameters, q memorizes the plastic strain amplitude. A memory surface F_m (equation 11) is defined in the plastic strain space. It develops following the current plastic strain path. Here hardening rules similar to those for rate independent plasticity apply.

$$F_m = \frac{2}{3} J\left(\boldsymbol{\varepsilon}^{pl} - \boldsymbol{\zeta}\right) - q < 0 \quad \text{with} \quad J\left(\boldsymbol{\varepsilon}^{pl} - \boldsymbol{\zeta}\right) = \sqrt{\frac{3}{2} (\boldsymbol{\varepsilon}^{pl} - \boldsymbol{\zeta}) : (\boldsymbol{\varepsilon}^{pl} - \boldsymbol{\zeta})} \tag{11}$$

q and **ζ** represent the radius and the center of the hypersphere, they evolve [50,51] according to (equation 12)

$$\dot{q} = \frac{2}{3} \eta H(F) \langle \mathbf{n} : \mathbf{n}^* \rangle \dot{\bar{\varepsilon}}^{pl} \qquad \dot{\boldsymbol{\zeta}} = \frac{2}{3} (1 - \eta) H(F) \langle \mathbf{n} : \mathbf{n}^* \rangle \mathbf{n}^* \dot{\bar{\varepsilon}}^{pl} \tag{12}$$

where the unit normal to the memory surface is calculated as (equation 13)

$$\mathbf{n}^* = \frac{2}{3}(\boldsymbol{\varepsilon}^{\mathrm{pl}} - \boldsymbol{\zeta})/\mathrm{J}(\boldsymbol{\varepsilon}^{\mathrm{pl}} - \boldsymbol{\zeta}) \tag{13}$$

and the unit normal to the yield surface as (equation 14)

$$\mathbf{n} = \frac{2}{3}(\mathbf{S} - \boldsymbol{\alpha})/\mathrm{J}(\mathbf{S} - \boldsymbol{\alpha}) \tag{14}$$

The Heaviside function H gives H(F)=0 if F<0 and H(F)=1 if F=0. The McCauley symbol in $\langle \mathbf{n}:\mathbf{n}^* \rangle$ ensures that the term vanishes if the current plastic strain rate direction $\mathbf{n}$ points into the interior of the memory surface. The parameter 0<η<1/2 was introduced by Ohno [52] and enables a gradual transition into memorization.

2.4 Parameter determination

Determination of the kinematic hardening behavior

Hysteresis loops obtained in the cyclic tension-compression tests are used to determine the kinematic hardening parameters C_k and γ_k plus the current yield stress σ^0. The prepreg material is modeled using a temperature-dependent elastic-plastic material model. The elastic properties are modeled as orthotropic, the plastic properties, for the sake of simplicity, are modeled as isotropic. A von Mises yield criterion is used, measured values of the fill direction are taken as this is the loading direction in the cyclic tension-compression tests (see Figure 11). The overall backstress is defined as the sum of two backstresses, a nonlinear (equation 15) and a linear one (equation 16).

$$\dot{\boldsymbol{\alpha}}_1 = C_1 \frac{1}{\sigma^0}(\boldsymbol{\sigma} - \boldsymbol{\alpha})\dot{\bar{\varepsilon}}^{pl} - \gamma_1 \boldsymbol{\alpha}_1 \dot{\bar{\varepsilon}}^{pl} + \frac{1}{C_1}\boldsymbol{\alpha}_1 \frac{dC_1}{dT} \tag{15}$$

$$\dot{\boldsymbol{\alpha}}_2 = C_2 \frac{1}{\sigma^0}(\boldsymbol{\sigma} - \boldsymbol{\alpha})\dot{\bar{\varepsilon}}^{pl} + \frac{1}{C_2}\boldsymbol{\alpha}_2 \frac{dC_2}{dT}. \tag{16}$$

The shape of the experimentally obtained hysteresis loops calls for a nonlinear evolution law according to equation 15. Models using that kind of backstress evolution law overestimate ratcheting [53,54], but the predictive performance can be improved by adding a linear backstress. By modifying the ratio C_1/C_2 the degree of ratcheting can be adjusted. The parameter identification is accomplished using an optimization procedure. First a FEA-model of the test setup is created using

Abaqus. The model takes advantage of the quarter-symmetry of the specimen and considers the influence of the fixture. Figure 25a shows the modelled region of the specimen, Figure 25b shows the FEA-model and the used boundary conditions to account for the symmetry and the fixture. Quadratic shell elements with reduced integration (Abaqus element type S8R, continuum shell formulation) are used. The loading direction displacements of the nodes on the top of the model are kinematically coupled to a reference point, which guarantees that the symmetry line remains straight. The load is then applied to the reference node. The model is used to computationally determine the material response of certain sets of material parameters (C_1, C_2, γ and σ^0). The parameters are varied governed by an optimization algorithm. Figure 26 shows the optimization procedure by means of

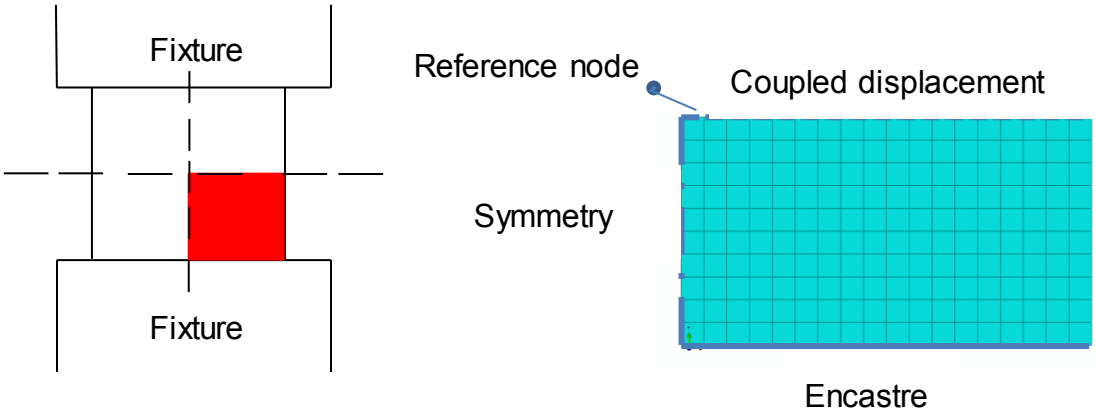

Fig. 25: a) Modelled region of the specimen (red mark) b) FEA-model of the specimen.

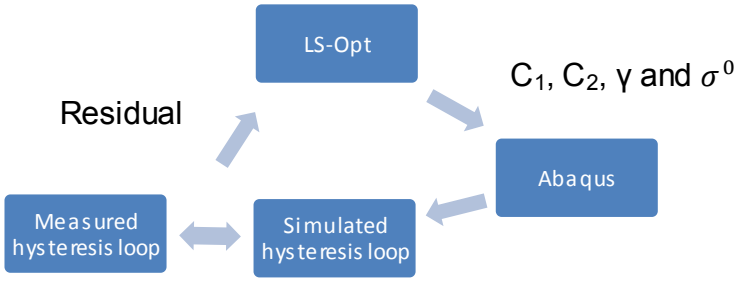

Fig. 26: Optimization procedure for parameter determination

LS-Opt. Abaqus is used as a “user defined solver” in the LS-Opt optimization procedure. First, test sets of material parameters (C_1, C_2, γ and σ^0) are chosen based on full-factorial design of experiments. Moreover, also a D-optimal [55] design of experiments algorithm is used. Subsequently these sets of material parameters are entered into an Abaqus input file and the loading of the cyclic tensile-compression test is simulated. First, when required by the load case, the heating-up of the sample is simulated. This allows working out thermal strains and residual stresses due to the thermal mismatch of the constituents of the specimen. Afterwards it is subjected to the same cyclic loads as in the experiments. Since the material response of the model with constant yield stress σ^0 stabilizes very quickly, simulating only four cycles is found to be sufficient. To compare the simulated material response to the one obtained in the tests, a “curve-mapping algorithm” [55] is employed. This algorithm calculates the area between two curves and uses it as a residual for optimization tasks. Based on these residuals, new sets of test parameters are chosen by LS-Opt. The material response of every set of parameters is plotted in order to be able to manually intervene in the selection of new material parameters. By repeating it for different hysteresis loops, an optimal set of parameters can be found.

Determination of the isotropic hardening behavior

In the “Nonlinear isotropic/kinematic hardening model” the isotropic hardening component is represented by a relationship between yield stress σ^0 and equivalent plastic strain $\bar{\varepsilon}^{pl}$. Since this tabular relationship is not a-priori known a methodology has to be devised that allows to iteratively forecast the increment of equivalent plastic strain $\bar{\varepsilon}^{pl}$ pertaining to a given yield stress σ^0 within each cycle. As the experimentally determined current yield stress σ^0 depends on both the number of elapsed cycles and the loading situation, simulations of every loading situation using different values of the yield stress σ^0 are conducted. That way, a relationship between the yield stress and the equivalent plastic strain accumulated during each loading cycle can be obtained. In order to ensure that these values are taken from a stabilized cycle, four loading cycles are simulated and the magnitude of the equivalent plastic strain increment that is added in the fourth loading cycle is chosen. This was done because the amount of equivalent plastic

strain generated in the first loading cycle can significantly differ from the one obtained in the subsequent cycles. This is especially the case in asymmetric loading situations. By using a Matlab code these functions are fitted and analytical expressions were obtained. Figure 27 shows the procedure for the identification of the values of the equivalent plastic strain and explains how the sampling points of the tabular function are generated. It should be noted that the first entry of this

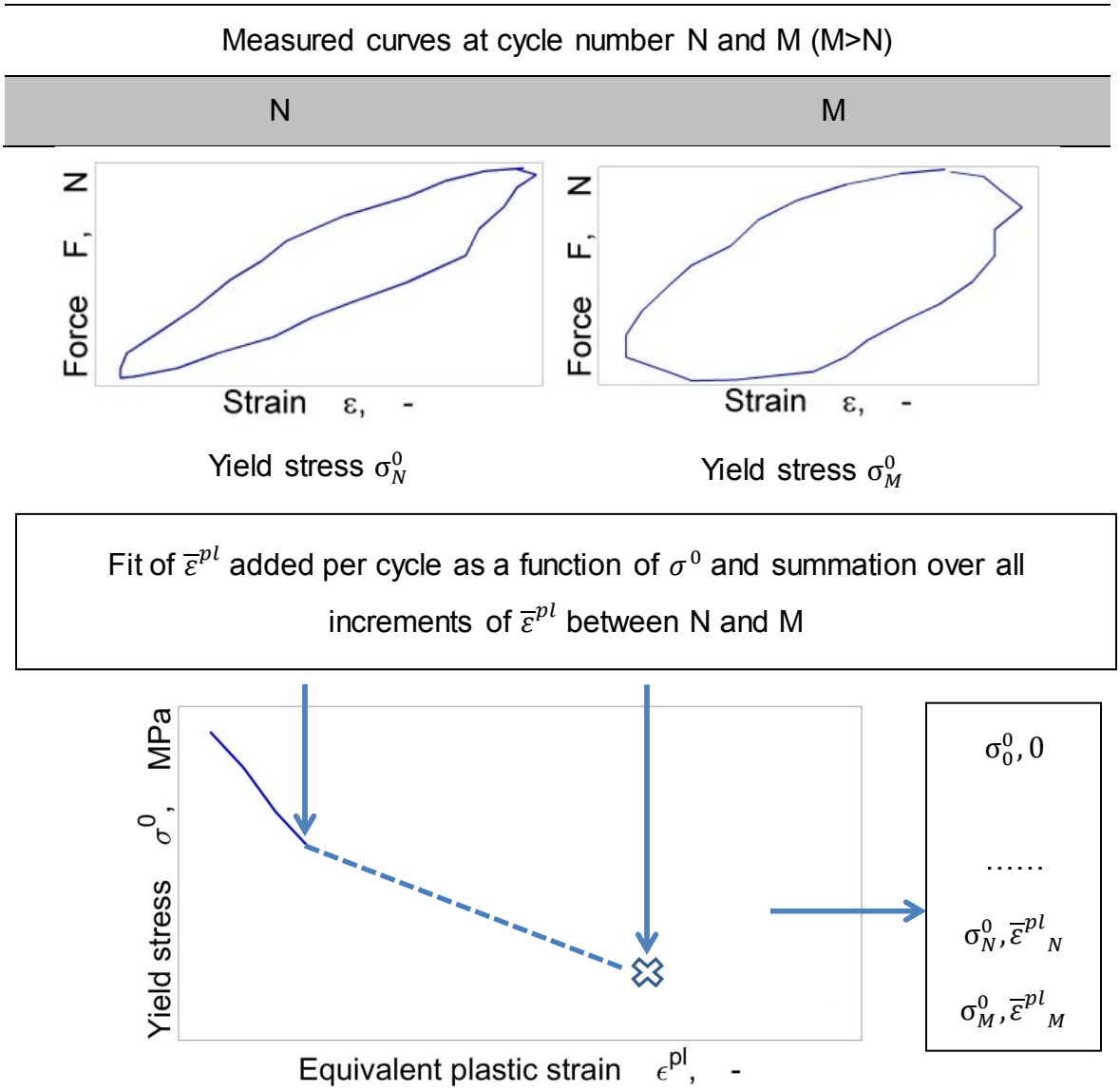

Fig. 27: Determination of the equivalent plastic strain. The iteratively determined sampling point is marked.

function always has to be the initial yield stress and zero equivalent plastic strain. The sampling points are obtained step-by-step, because the amount of equivalent plastic strain $\bar{\varepsilon}^{pl}$ at cycle number N (see Figure 27) needs to be known for the

determination of the amount of equivalent plastic strain $\bar{\varepsilon}^{pl}$ at cycle number M>N. Bearing in mind that the values of the yield stress σ^0 are linearly interpolated between the sampling points, a Matlab script determines the suitable value of the equivalent plastic strain for a given cycle number M iteratively. This script basically adds up the equivalent plastic strain increments depending on the current yield stress. Here the analytical relationship between the yield stress and the equivalent plastic strain added during each loading cycle and the known amount of equivalent plastic strain $\bar{\varepsilon}^{pl}$ at cycle number N is used. Furthermore, the yield stresses σ^0 and the elapsed number of cycles are needed as input for this procedure. It is verified by simulating the cyclic tension-compression tests using the obtained material parameters and comparing it to the experimental results.

2.5 Results of the parameter determination

Kinematic hardening behavior

As the heating-up of the specimens cannot be recorded with digital image correlation, only the strains caused by the mechanical load can directly be compared with the simulations. Nevertheless, the simulations must of course also reproduce the heating-up stage. Therefore, the heating-up is simulated, using the known coefficients of thermal expansion for the copper and for the FR4-prepreg from [45]. Then the mechanical loading is applied to the model. For the figures in this section and also for the optimization process the thermal strains are subtracted from the total strains obtained in the simulations in order to ensure comparability and to account for the thermal loads. The parameters C_1, C_2, D (see section 2.6.) and the yield stress σ^0 are normalized by the initial yield stress of copper at room temperature $\sigma|_0$ $(T = 23°C)$. In the following the normalized values are called $\bar{C}_1$, $\bar{C}_2$, $\bar{D}$ and $\bar{\sigma}^0$. For all relevant loading cases (see Table 2) the sets of kinematic hardening parameters are shown in Table 6. At higher temperature the material stiffness decreases. This is shown for the elastic properties in Table 4, but it can also be seen in the plastic regime as C_1 decreases (see Table 6). At 145°C a higher value of C_2 is chosen to reduce the degree of ratcheting, as models with a large C_1/C_2 ratio tend to overestimate ratcheting. The ratcheting behavior can be further optimized by using a backstress evolution law including a threshold [56],

Table 6. Kinematic hardening parameters

Temperature [°C]	$\bar{C}_1$ [-]	$\bar{C}_2$ [-]	γ_1 [-]
23	2778	33	1900
85	2778	33	1900
145	2228	83	1900

this is not done as the simulated ratchet strains are in good agreement with the measured ones. Figure 28 exhibits hysteresis loops at 23°C and the results of the corresponding simulations, using the parameters from Table 6. Figures 29 and 30 depict hysteresis loops recorded at 85°C and at 145°C and the corresponding simulated material response. The legend shows the upper and lower force limit as well as the number of elapsed cycles. The shape of the simulated hysteresis loops can be reproduced reasonably well for all relevant loading cases; a further refinement with additional backstresses (equations 15 and 16) is not useful due to the scatter in the measurement results.

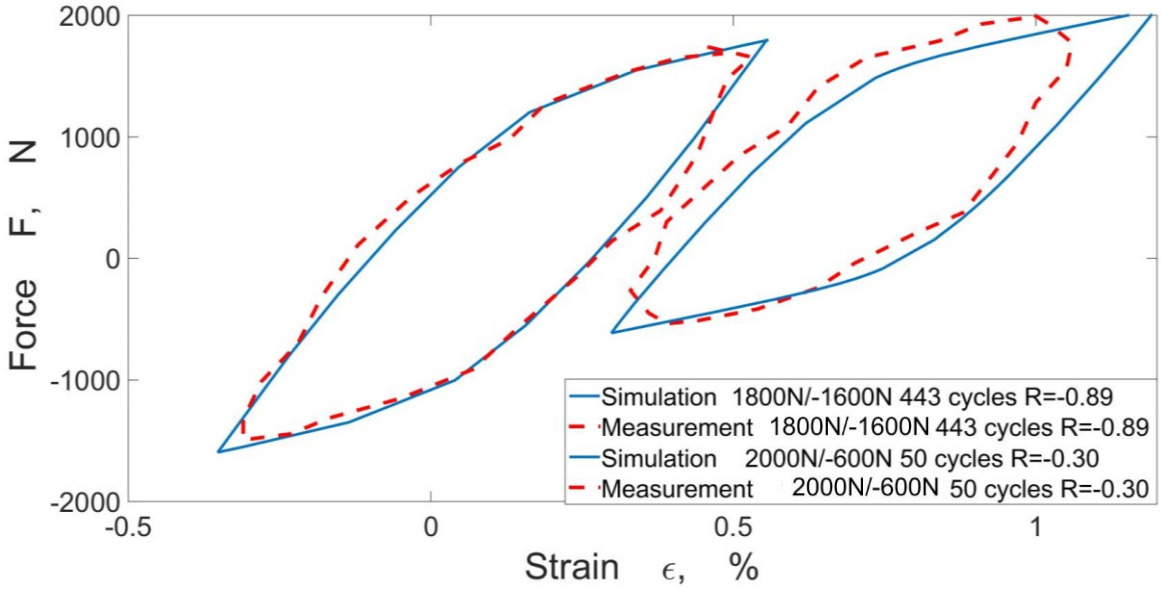

Fig. 28: Hysteresis loops obtained under different loading conditions at 23°C and the corresponding fits.

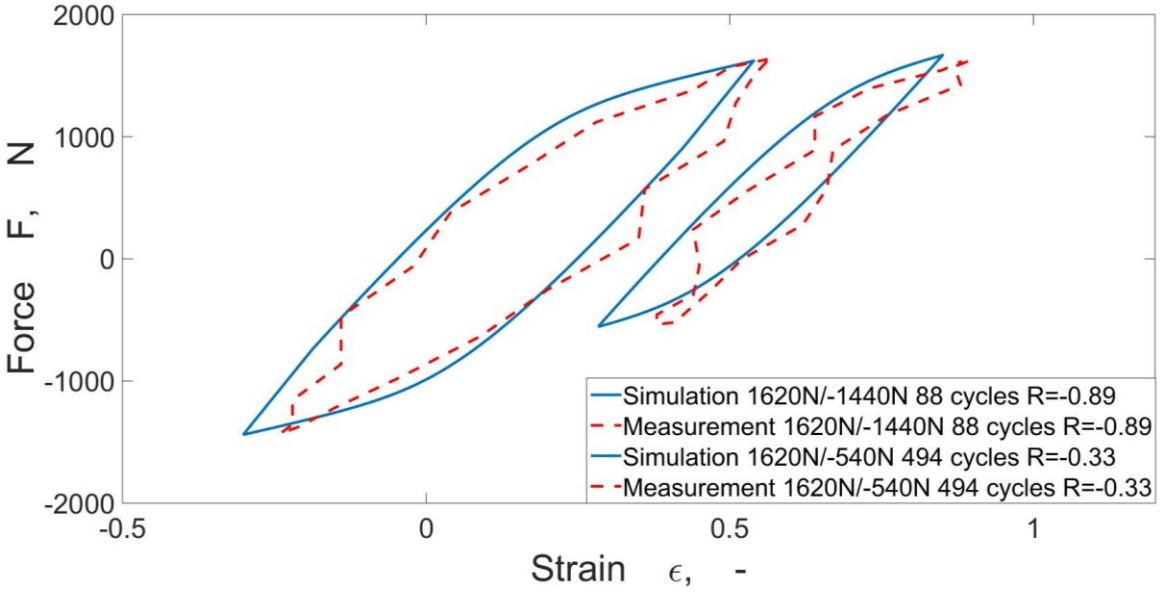

Fig. 29: Hysteresis loops obtained under different loading conditions at 85°C and the corresponding fits.

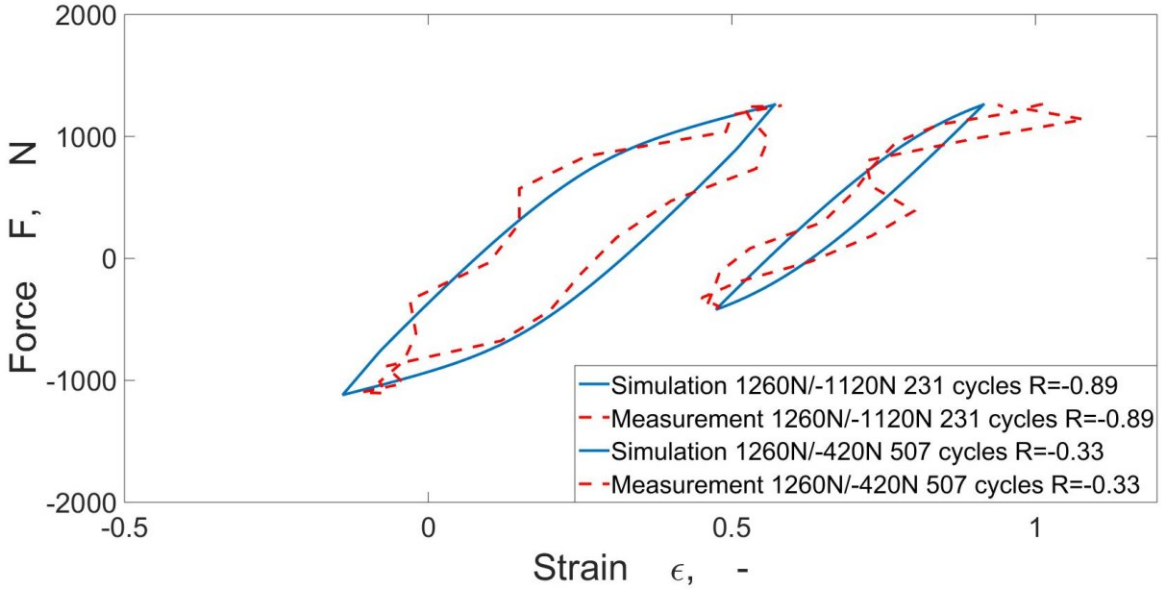

Fig. 30: Hysteresis loops obtained under different loading conditions at 145°C and the corresponding fits.

Isotropic hardening behavior

In Figure 31 the material response of a specimen subjected to sinusoidal loading (upper limit: 2000N, lower limit -600N) at room temperature is shown. The hysteresis loops obtained at different cycle numbers and the known yield stresses σ^0 at these cycle numbers are used to identify the tabular function, see Table 7.

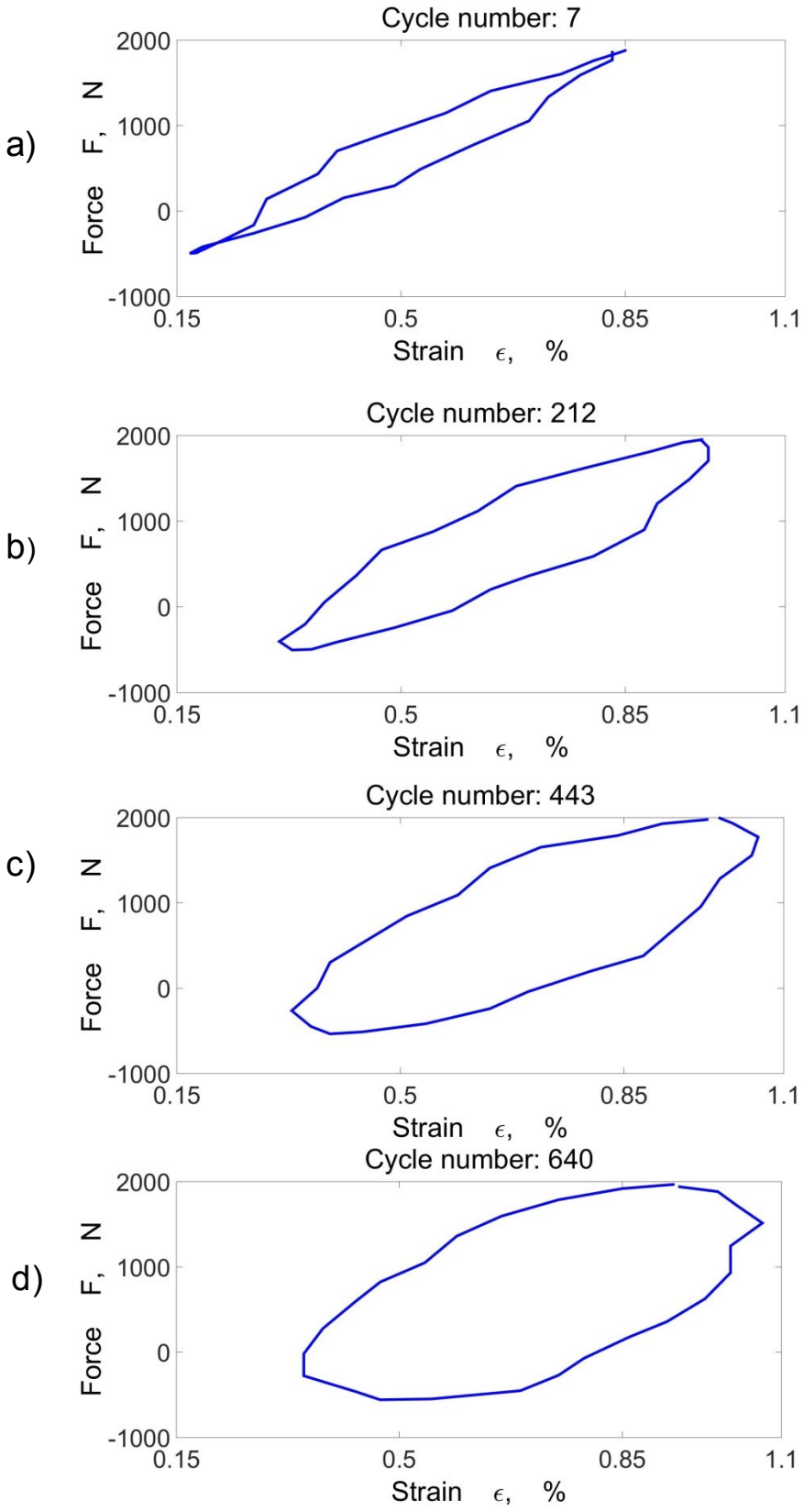

Fig. 31: Hysteresis loops obtained at different cycle numbers.

Table 7: Isotropic hardening behavior. In the first column the corresponding hysteresis loop in Figure 29 is given.

	Norm. yield stress σ^0 [-]	Equivalent plastic strain $\bar{\varepsilon}^{pl}$[-]
a)	1	0.0
a)	1	0.00984
b)	0.2571	0.52033
c)	0.0952	2.80569
d)	0.0190	5.51740

The amount of equivalent plastic strain $\bar{\varepsilon}^{pl}$ accumulated in each loading cycle is calculated. The yield stress obtained in the hysteresis loop shown in Figure 31a (cycle number 7) is also taken as initial yield stress, as the first cycles cannot be measured properly due to the tuning of the testing machine. Since this research work focusses on lifetime assessment, no focus is put on the first cycles. As shown in Figure 31, the investigated copper grade shows cyclic softening. This is true for all tested strain ranges and temperatures. Comparing the isotropic hardening behaviors obtained at different strain ranges, they differ from each other. Hence it is not sufficient to model the isotropic hardening behavior using a single relationship between yield stress σ^0 and equivalent plastic strain $\bar{\varepsilon}^{pl}$ as it is done in the “Nonlinear isotropic/kinematic hardening model”. The figures 32 a) to

a)

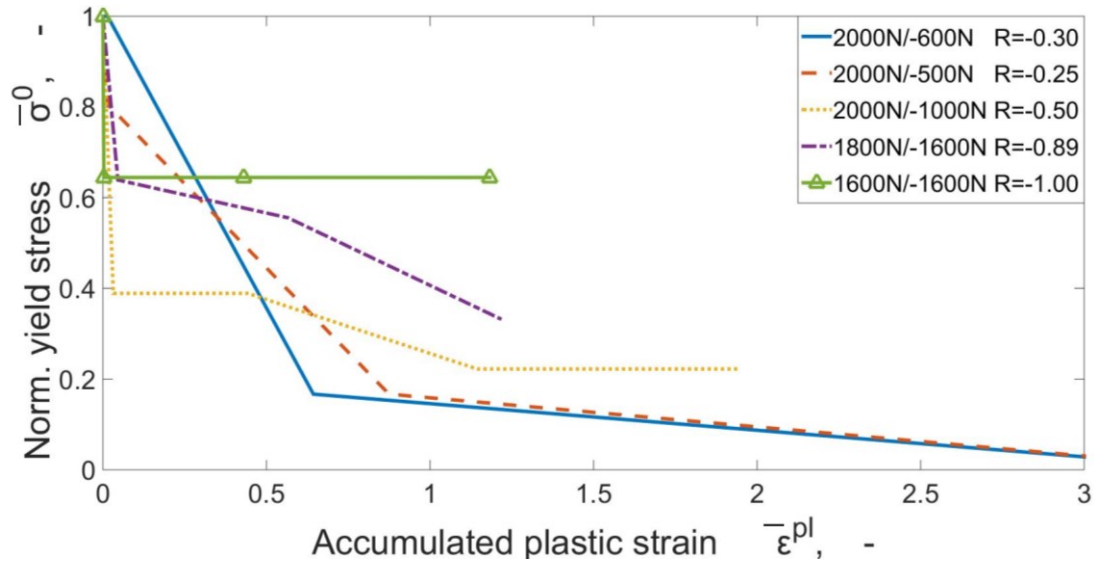

b)

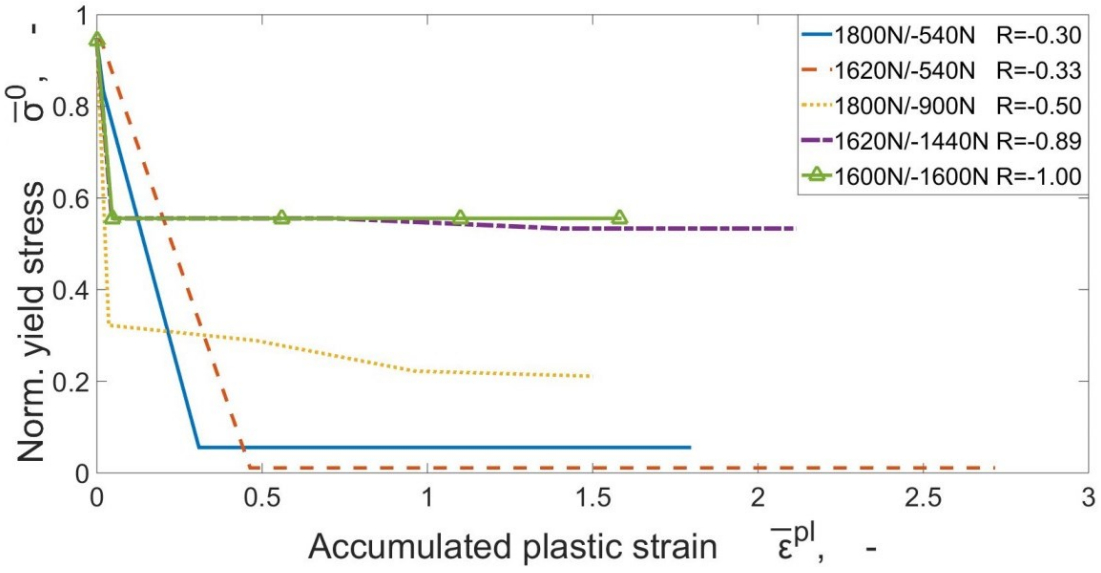

c)

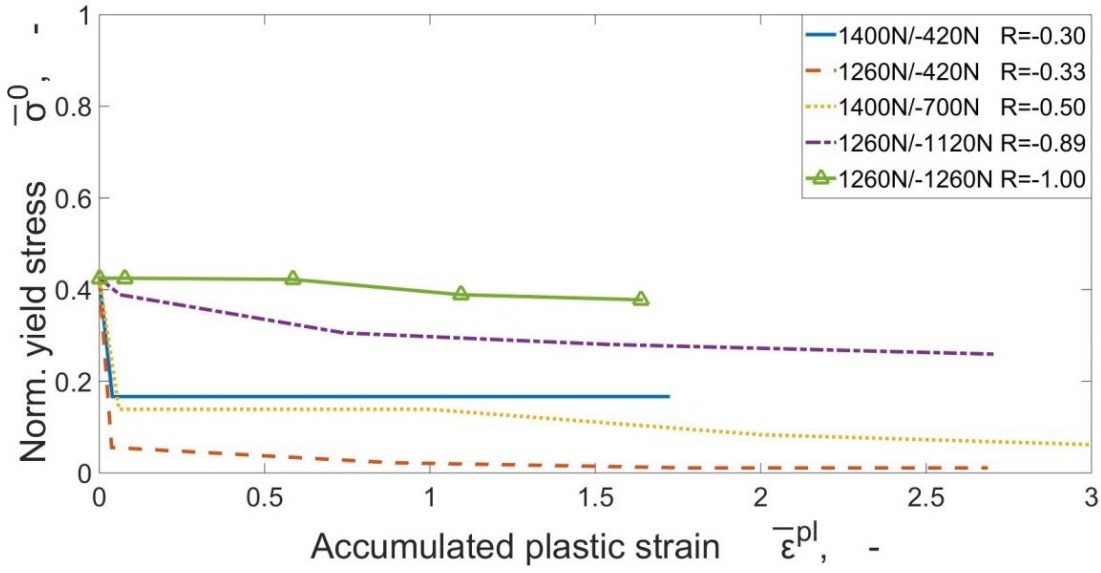

Fig. 32: a) Isotropic hardening behavior at 23°C, b) isotropic hardening behavior at 85°C, c) isotropic hardening behavior at 145°C.

c) show the obtained isotropic hardening behavior at 23°C, 85°C and 145°C. The force limits are reported in the legend. The specimens are tested until fracture. The relationship between yield stress and accumulated plastic strain is not unique. It depends strongly on the loading case. In all cases, the material shows cyclic softening as expected for cold-worked copper [57]. The experimental data shows that lower R-ratio results in stronger cyclic softening.

Evaluation of strain range dependency

The plastic strain range memorization formalism described in section 2.3 (starting from equation 10) is utilized to model the isotropic softening behavior shown in Figure 32. The following evaluation is done for the material behavior at room temperature, shown in Figure 32 a). The parameters for the strain range memorization are determined by the software LS-Opt using a full-factorial design of experiments. A least squares approach is used for the optimization where all loading cases are weighted equally. Abaqus is used as "user defined solver"; a model of the test setup is implemented. The difference between the experimentally determined values of the material parameter Q (see equation 9) for every single loading case and the ones predicted by the strain range memorization model is used as residuum to be minimized. Q stands for the yield stress of the stabilized cycle. The determined material parameters are given in Table 8, their usage is shown in the equations (10) to (12). Figure 33 exhibits a comparison between the values of Q experimentally determined for the individual load cases and the ones predicted by the model. Obviously the correlation between simulation and experiment is not satisfactory even though the model memorizes the plastic strain range [28]. The isotropic hardening behavior does not seem to depend

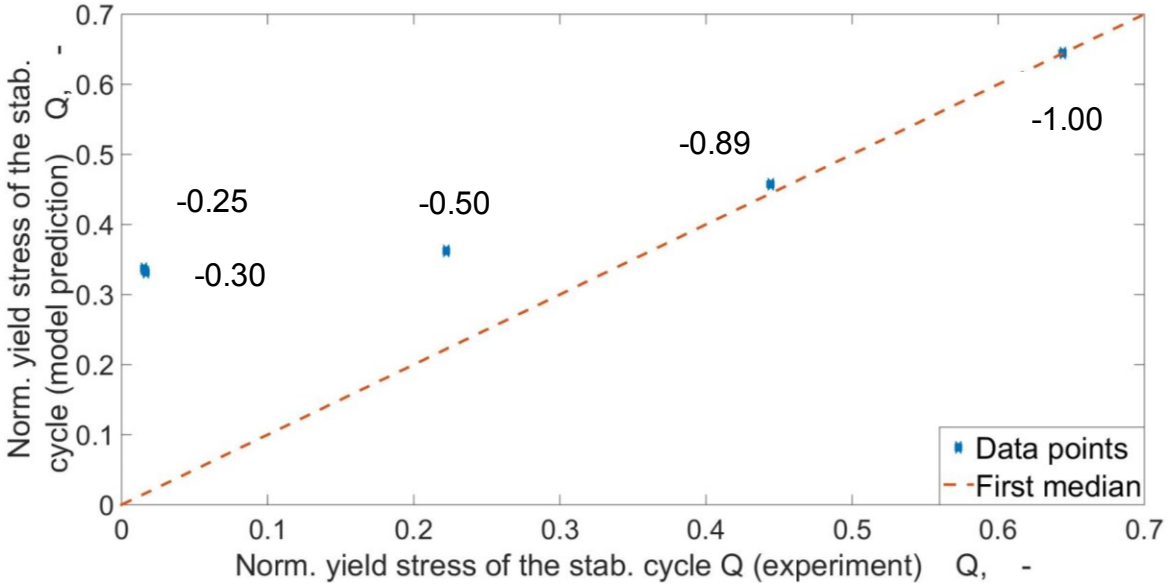

Fig. 33: Comparison of the stabilized yield stresses Q obtained from the loading cases at 23°C. At every sample point the R-ratio is given, the data points for R=-0.25 and R=-0.3 almost coincide.

Table 8: Parameters for the strain range memorization model at 23°C

$\bar{Q}_S$ [-]	η [-]	μ [-]	q_i [-]
Lowest stabilized yield stress	Material parameter	Material parameter	Initial radius of F_m
0.015	0.3	250	0.002

(linearly) on the plastic strain range. Furthermore, the plastic strain range changes over the elapsed cycles, as the experiments are in a conducted force-controlled way with a simultaneous drop of the yield stress, as shown in Figure 32 a) to c). Hence, strain range memorization can be used to roughly estimate the amount of cyclic softening but it is still too inaccurate to model all the loading cases.

2.6 Mean backstress memorization model

Rather than a strain range influence a correlation between the yield stress of the stabilized cycle and the mean force in the tests is observed, see Figure 34. To account for that a phenomenological approach is proposed (equation 17) intended for cyclic loads and low strain rates. The strain rate in the tests was of the order of

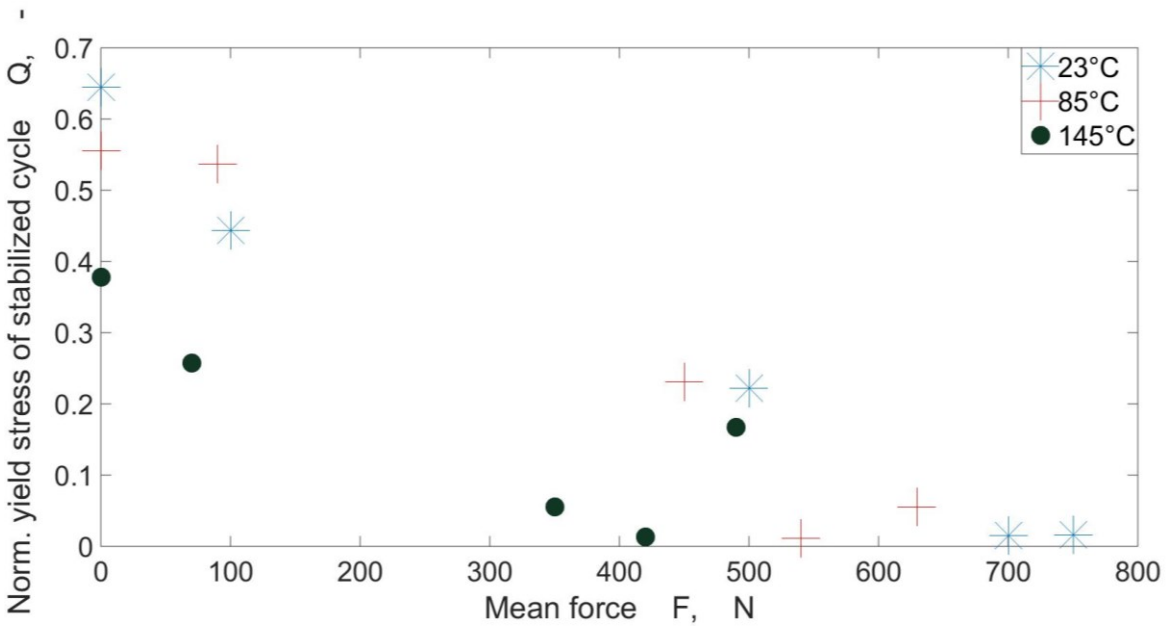

Figure 34: Yield stress of the stabilized cycle over mean value of the sinusoidal force signal in the experiment.

$$c = \frac{1}{T_C}\int_{t\left(\bar{\varepsilon}^{pl}=0\right)}^{t\left(\bar{\varepsilon}^{pl}=\bar{\varepsilon}^{pl\_limit}\right)} I_1(\alpha)\,dt \qquad \text{with} \qquad I_1(\alpha) = \alpha_{11} + \alpha_{22} + \alpha_{33} \tag{17}$$

0.01 s^{-1}. The basic idea is to introduce a further internal variable c memorizing the mean stress. As the overall backstress **α** gives the center of the elastic region, the first invariant of the backstress $I_1(\boldsymbol{\alpha})$ is calculated and integrated over a certain timespan. The time needed to reach a certain amount of accumulated plastic strain ($\bar{\varepsilon}^{pl}$) is used. In this work, a limit of $\bar{\varepsilon}^{pl\_limit}$=0.02 is used. Finally, the so-obtained value is divided by the duration of one loading cycle T_C. The internal variable c has the unit MPa. Figure 35 shows the correlation between the internal variable c and the (normalized) yield stress Q of the stabilized cycle. This correlation can be fitted very well by an exponential function, shown in equation 18. The material parameters D and g are listed in Table 9; D was normalized ($\overline{D}$).

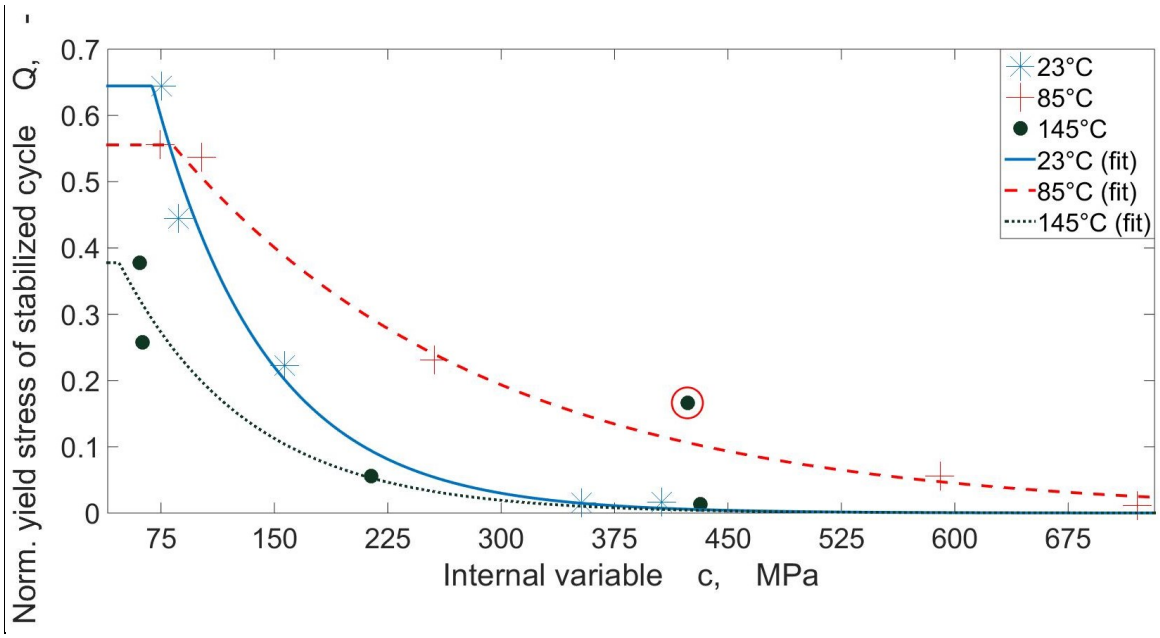

Figure 35: Yield stress of the stabilized cycle over the proposed internal variable. The value in the red circle was disregarded for obtaining the fit curve.

Table 9: Parameters for the phenomenological model

Temperature [°C]	23	85	145
$\overline{D}$ [-]	1.62	0.83	0.66
g [1/MPa]	-0.0133	-0.0048	-0.0118

Note that for implementation reasons the Q versus c curves were truncated with the highest value for Q recorded at a given temperature, see the plateaus in Figure 35.

$$Q = D(T)e^{-g(T)|c|} \tag{18}$$

This “mean backstress memorization” model works well for all investigated temperatures, but if one compares the curve for 23°C and for 85°C in Figure 35, the one for 85°C surprisingly shows higher values for the yield stress of the stabilized cycle.

Implementation

The model described in this chapter is implemented in Abaqus, for the sake of simplicity in a semi-explicit way using the concept of a “User defined field variable (USDFLD)” [58]. The value of the yield stress of the stabilized cycle Q is used as field variable; the different isotropic hardening behaviors (see Figure 32) are listed under the menu item "cyclic hardening". Consequently the user subroutine calculates the value of the internal variable c and the yield stress of the stabilized cycle Q during the analysis and selects the appropriate isotropic hardening behavior.

2.7 Validation

Validation test

As the material model presented in this thesis was calibrated under isothermal conditions, the objective of this test is to validate it also for non-isothermal loading conditions. Curvature measurements of a bimaterial composite consisting of a thin copper film sputtered onto a silicon substrate are performed. In this technique, stress is generated in the film due to the mismatch of the thermal expansion coefficients between film and substrate. The motivation for that kind of validation experiment is the fact that copper foils in PCBs are subjected to the same loading conditions as in this experiment. The specimens consist of a 20 µm-thick copper layer electrodeposited on a 700 µm-thick (100) silicon wafer. The samples are cycled from 80°C to 180°C in forming gas atmosphere to avoid copper oxidation. The experiment is conducted in the kSA MOS thermal scan (k-Spaces Associates,

Inc, Dexter, MI, USA). The substrate curvature changes are measured over temperature using an array of parallel laser beams [59,60]. For a polycrystalline film, which can be assumed isotropic, the measured curvature κ can be converted to an average stress σ_f in the film using Stoney's formula (equation 19) [61,62]:

$$\sigma_f = \frac{M_s\, h_s^2}{6\, h_f}\, \kappa \qquad (19)$$

where $M_s = 1/(s_{11}+s_{12})$ is the substrate biaxial modulus given as a function of the compliance coefficients s_{11} and s_{12}, h_s being the substrate thickness and h_f the film thickness. The wafer dimension (300 mm diameter) ensures that the film is under biaxial stress. In addition, given the respective thicknesses (h_f=20µm, h_s=700µm) and elastic properties (M_f=197GPa, M_s=180GPa) of the film and substrate, Stoney's equation is accurate within 10% [63].

Simulation

The tests are modelled in the FEA-software Abaqus. Quadratic 20-node brick elements with reduced integration (Abaqus name C3D20R) were used. Just a small sector of the 300 mm wafer is modelled, periodic boundary conditions are applied. The mesh is shown in Figure 36.

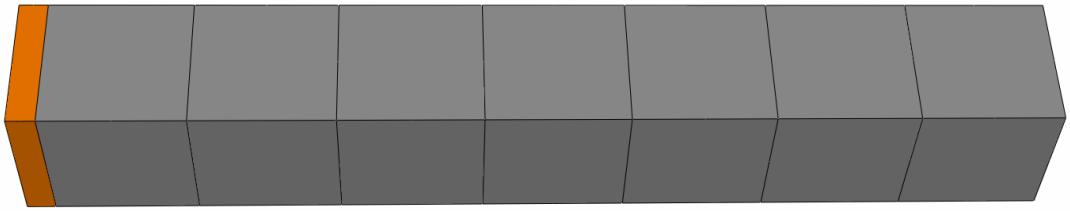

Fig. 36: Finite element model of the specimen for the curvature tests.

The copper is shown in gold, the silicone in grey. The material input data for silicon is taken from the literature [64,65]. Figure 37 a) shows the temperature profile and Figure 37 b) the stresses occurring in the curvature measurements as well as the simulated material response. The copper shows mean stress relaxation as the R-ratio in the test is close to -1, although one could expect that the copper would be subjected to compression loads only since the coefficient of thermal expansion of copper is far higher than that of silicon. The model reproduces this effect very well.

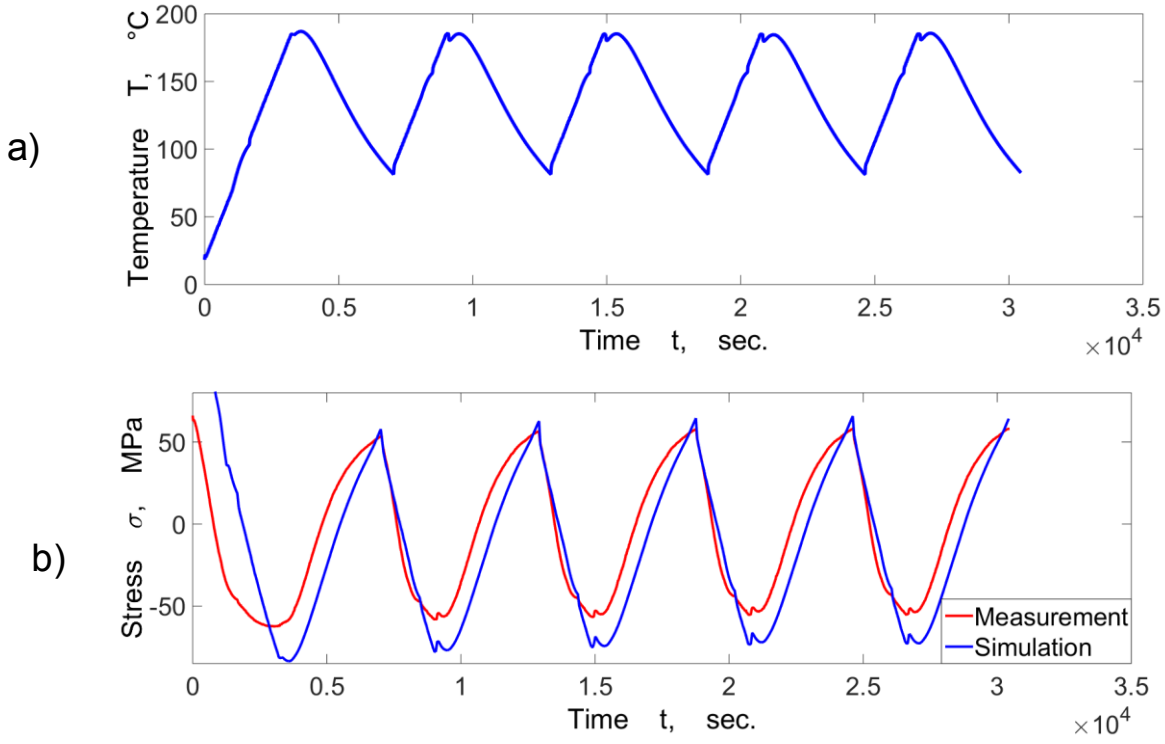

Fig. 37: Curvature measurements a) temperature profile, b) measured and calculated stresses.

3. ANALYSIS OF COMPONENT

3.1 General structure of a PCB

A PCB acts as a support for electronic components. It electrically connects the components to each other and is used for mechanical attachment. Figure 38 shows the schematic structure of such a PCB. Prepregs and cores are fiber-reinforced polymers, which can differ in the matrix (epoxy resins) and in the reinforcing glass fiber fabrics. They are called FR4 materials, FR stands for flame retardant. Cores are prepregs to which the copper layers were applied in advance. The sequence of prepregs and cores and the number of layers can be varied. Vias are electrical connections of conductive layers in a printed circuit board, which are usually implemented as metallized hole. Figure 38 shows three basic types of vias [66], the "blind via" (1) extends from the edge to one of the middle layers, the "buried via" (2) is buried inside the PCB and the "through hole" (3) extends through the entire circuit board. Vias with a small diameter are often referred to as

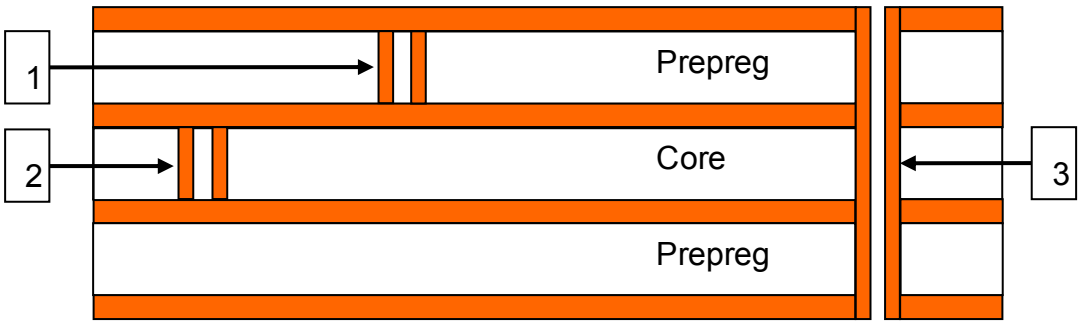

Fig. 38: Schematic structure of a printed circuit board made of fiber-reinforced plastic and copper layers. The copper layers are marked in orange.

microvias. To protect the circuit board from corrosion and mechanical damage solder resist is applied to the outermost copper layers. The process of manufacturing printed circuit boards containing vias [66] can be divided into three basic steps.

- Production of the dielectric materials
- Drilling of the hole

• Metallization of the drill hole.

For drilling in the dielectric materials, various technologies are available, where for FR4 materials mostly laser drilling is employed. Only in a few instances mechanical drilling is preferred (Hitachi HITAVIA technology). The metallization of the bore serves for producing the conductive connection and can be done by chemically deposited copper, galvanically applied copper, by the introduction of conductive pastes in the via or by the incorporation of hulls of solid metal.

3.2 Interconnection Stress Test

As cyclic thermal loading is a fatigue issue, material models reproducing the constitutive behavior under cyclic loading as well as a description for damage evolution are needed. Furthermore the question must be tackled to what extent mechanical damage correlates with degradation of the electrical performance. This work focuses on the copper vias that form the current paths. Their reliability is crucial to the functionality of whole devices or even systems. Hence the presented research provides a numerical methodology to test new circuit designs of PCBs under cyclic thermal loading conditions.

Interconnection Stress Tests (IST) [67,68] of different PCB designs were conducted to provide the experimental basis of this work. In such tests, PCBs are subjected to temperature cycles alternating between two extreme (e.g. -40°C to 160°C) temperatures. The electrical resistance is measured online during these tests. If the resistance rises to more than 10% of the initial value at the highest temperature, the test is terminated. Simultaneously, finite element models of these designs are set up in the commercial software Abaqus. For the material description the constitutive model for thin copper layers developed in this thesis is implemented and a pore growth indicator is added. Pore growth is chosen as a damage indicator, because the relationship between pore volume and electrical resistance is known from the literature [69]. It is thus used to establish a link between the mechanical and the electrical simulations (see section 3.4). In order to save a considerable amount of computation time and to be able to determine the parameters of the pore growth model, the damage simulations are done based on a stabilized loading cycle. To this end, the stress-strain state at a stabilized

cycle is exported from Abaqus and pore growth is calculated by means of an external Matlab-Script. Separating the mechanical analysis from the pore growth calculations is admissible as long as the pore volume fraction does not feed back to the elastic data which has been assumed here for the sake of simplicity. The so-calculated local pore volume fraction is then re-imported into Abaqus by means of a user subroutine (User Defined Field UFIELD) [58] for the subsequent electrical simulations obviously significantly affecting the conductance properties of the current paths. That way, a virtual IST can be performed using a decoupled mechanical-electrical FEA.

3.3 Material models

Constitutive modeling

Modelling of the copper parts

For modeling the constitutive behavior of thin copper layers the “nonlinear isotropic/kinematic hardening model” implemented in Abaqus is employed. It is extended by a mean backstress memorization, see section 2 of this thesis. The temperature-dependent coefficient of thermal expansion (CTE) for the used copper grade is determined in [45].

Modeling of the dielectrical parts

In PCBs both glass fiber-reinforced epoxy resins (cores and prepregs) as well as the pure resin are utilized. The cores and prepregs are modeled using temperature-dependent orthotropic elasticity, for the pure resin a temperature-dependent isotropic elastic model is used. All of them are characterized in tensile tests at room temperature. Additionally, the temperature-dependent elastic properties are measured by Dynamic Mechanical Analysis (DMA). For the cores and prepregs the out-of-plane mechanical properties have to be calculated by micromechanics simulations. The corresponding measurements and methodologies are described elsewhere. [44,45,70] The temperature-dependent CTEs for the prepregs, cores (orthotropic) and resins (isotropic) are determined in [45].

Damage modeling

For the copper parts, a suitable pore growth model has to be identified and its parameters have to be determined. The model by Rice and Tracey [30] describes the growth of an initially spherical void in an infinite, rigid, ideally plastic von Mises material subjected to a homogeneous boundary strain rate. If spherical void growth is assumed, the average rate of growth can be calculated according to (equation 20)

$$\frac{\mathrm{d}r}{r} = \alpha \exp\left(\frac{3\sigma_m}{2\sigma_{eq}}\right) \mathrm{d}\bar{\varepsilon}^{\mathrm{pl}}. \qquad (20)$$

Here, r stands for the radius of the void, σ_m is the hydrostatic stress and α is a constant. As real materials are not ideally plastic, Beremin [71] suggested substituting the equivalent stress σ_{eq} for the yield stress in equation 20. Huang [31] reappraised the model and found for σ_m/σ_{eq}>1, α=0.427 and, for σ_m/σ_{eq}<1, α=0.427$(\sigma_m/\sigma_{eq})^{0.25}$. In real materials, α can differ from the theoretical value of the isolated cavity [32]. Therefore in this thesis equation 20 was adopted to model the evolution of the pore volume fraction V and the material parameters A and B were introduced (equation 21).

$$\frac{\mathrm{d}V}{V} = 3\alpha \exp\left(\frac{3\sigma_m}{2\sigma_{eq}}\right) \mathrm{d}\bar{\varepsilon}^{\mathrm{pl}} \qquad \text{with} \qquad \alpha = \mathrm{A}\left(\frac{\sigma_m}{\sigma_{eq}}\right)^{B} \qquad (21)$$

3.4 Component simulation

PCB designs

The following figures show the investigated PCB designs. These designs are specimens produced for the IST. The structures are largely repetitive, so in an effort to keep the models as small as possible a representative region has been identified that appears periodically in the PCB. The corresponding boundary conditions are described in the subsection ‘Structural modeling’ in this section. In the following figures the copper parts are shown in gold, pure resin parts in black. All other materials are explicitly marked in the figures. Figure 39 exhibits a design containing microvias. The investigated copper path is shown as well as a section through the structure to illustrate the layer build-up. The microvias have a diameter

of 35 µm. The PCB is 53.1 mm long and 4.2 mm broad. For this design the resin M1 is used, the woven fabric type is given in the figure. Wherever the copper was etched away, it has been replaced with pure resin. In the simulations a potential difference of 0.05 mV is applied between the faces marked with '1' and '2' in Figures 39 and 40 to measure the electrical resistance.

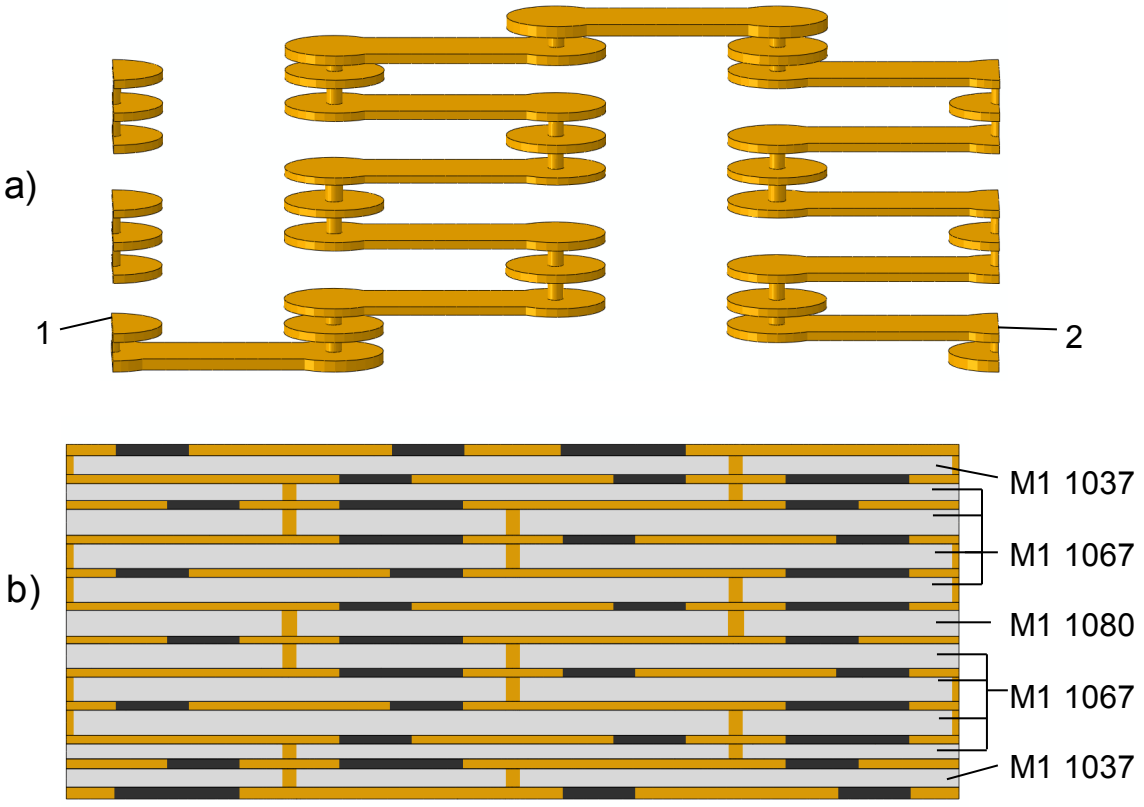

Fig. 39: Microvia-test design: (a) investigated copper path, (b) layer built-up.

Figure 40 shows the second investigated design containing (a) a buried via structure, (b) a through-hole via, (c) a line structure and (d) the corresponding

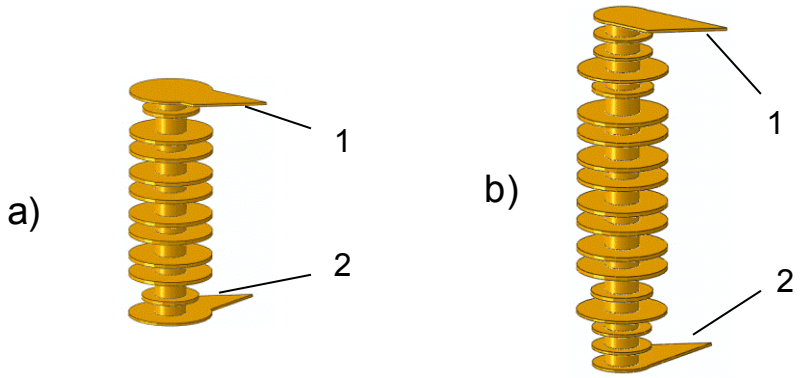

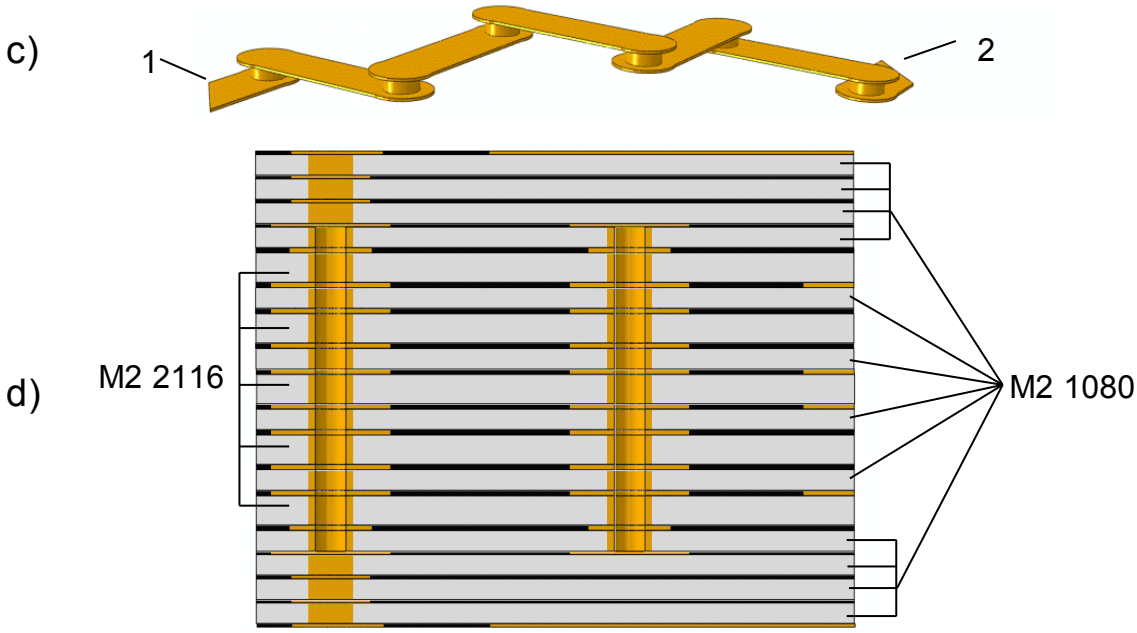

Fig. 40: a) Through hole b) buried via and (c) line structure test-design d) layer build-up.

layer build-up. Please note that the structures are hollow in some places. For this design the resin M2 is used. The vias in this structure have an (outer) diameter of 150 µm. This PCB is 63.6 mm long and 16.6 mm broad.

Virtual Testing

A methodology to perform a virtual IST is developed. Furthermore, suitable material parameters for the pore growth model described in section 3.3 are determined, see section 3.5. First the mechanical models are thermally cycled until a “stabilized” cycle is reached. The microvia design is cycled between 30°C and 200°C, the design shown in Figure 40 is cycled between 30°C and 150°C. These values are default values for the tested structures [67,68]. Since after a certain shakedown period no further change in the shape of the hysteresis loops is observed, the material behavior can be considered as stabilized. Since it is computationally very expensive to simulate hundreds of loading cycles, all further considerations concerning the pore fraction evolution refer to a stabilized stress-strain cycle. The corresponding data are exported to a text file, where for the sake of simplicity the values are averaged at the nodes in order to facilitate the subsequent re-import of the pore fractions into Abaqus. The error caused by this procedure will be small as the stress-strain state does not show large gradients

within one material at positions with high electrical current density. The pore growth is calculated analytically based on the stresses and strains obtained from the stabilized cycle according to equation 22. The mathematical operations are carried out by a Matlab script. In a stabilized cycle the right hand side of the first equation will remain constant in every cycle. Therefore it can be approximated using the second equation which can be integrated to yield the third equation. V_0 is the initial pore volume, N is the elapsed number of cycles. The constant K has to be determined numerically from a stabilized cycle.

$$\frac{\mathrm{dV}}{V} = 3\alpha \exp\left(\frac{3\sigma_m}{2\sigma_{eq}}\right) \mathrm{d}\bar{\varepsilon}^{\mathrm{pl}} \quad ==> \quad \frac{dV}{V} = KdN \quad ==> \quad V = V_0 e^{KN} \tag{22}$$

In this way, the pore volume fraction at each node after a given number of cycles can be calculated much faster than by purely incremental means. Please note that this simplification technically only works if the pore volume fraction does not feed back and thus influence the elastic data. As the IST is terminated if the resistance rises to more than 10% of the initial value at the highest temperature, the maximum average pore volume, see equation 23, is around 5.8%. Since a pore volume in that order of magnitude does not cause an essential reduction of the Young's modulus [72], the chosen approach is admissible. Subsequently, from these values the specific electrical resistivity ρ is calculated using analytical correlations between pore volume and electrical resistivity [69], see equation 23.

$$\frac{\rho_{BULK}}{\rho} = \frac{1-V}{1+11V^2} \quad \text{with} \quad \rho_{BULK}(\mathrm{T}) = \rho(\mathrm{T}_0).(1+\beta.(\mathrm{T}-\mathrm{T}_0)) \tag{23}$$

Here the specific electrical resistivity depends linearly on the temperature T, the correlation coefficient β was taken from the literature [73]. This relationship is implemented as a User Field by means of an appropriate subroutine (UFIELD) in Abaqus [58]. This subroutine imports the pore volume fraction for every node of the model and returns the correct electrical specific resistivity in the electrical FEA. In these simulations a potential difference of 0.05 mV is applied between the faces marked with '1' and '2' in Figures 39 and 40. The reaction current is recorded and the global electrical resistance of the structure after an arbitrary number of thermal loading cycles is calculated. The schematic of such a virtual IST is shown in Figure 41.

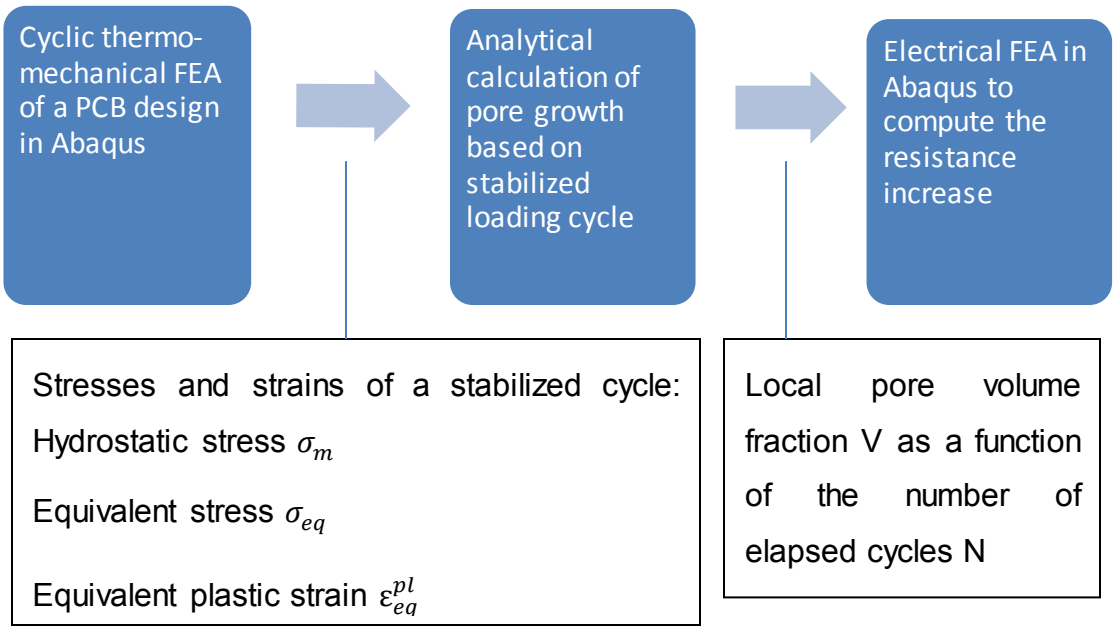

Fig. 41: Virtual Interconnection Stress Test (IST)

Structural modeling

For the mechanical models quadratic brick elements (C3D20R) are used, because they give reasonably accurate results and do not show any locking effects [24]. The electrical FEA models have exactly the same geometry and mesh topology as the mechanical models, only the element type must be changed. Here quadratic coupled thermal-electrical brick elements (DC3D20E) are used. In Abaqus electrical simulations can be conducted in the framework of coupled thermal-electrical or coupled thermal-electrical-structural simulations. For the present work, the first option was chosen, as the "nonlinear isotropic/kinematic hardening model" is not available in coupled thermal-electrical-structural simulations in Version 6.13.

The necessary size of the mesh is determined in a convergence study. For this study, a small example structure taken from the microvia-test design (see Figure 42) is used, since it is evidently the component most susceptible to discretization errors. The geometry and the (finally) chosen mesh of this example structure is shown in Figure 42. First, only the electrical simulation is performed using an arbitrary constant value for the electrical conductivity to evaluate the electrical mesh influence. A potential difference of 0.05 mV is applied between the

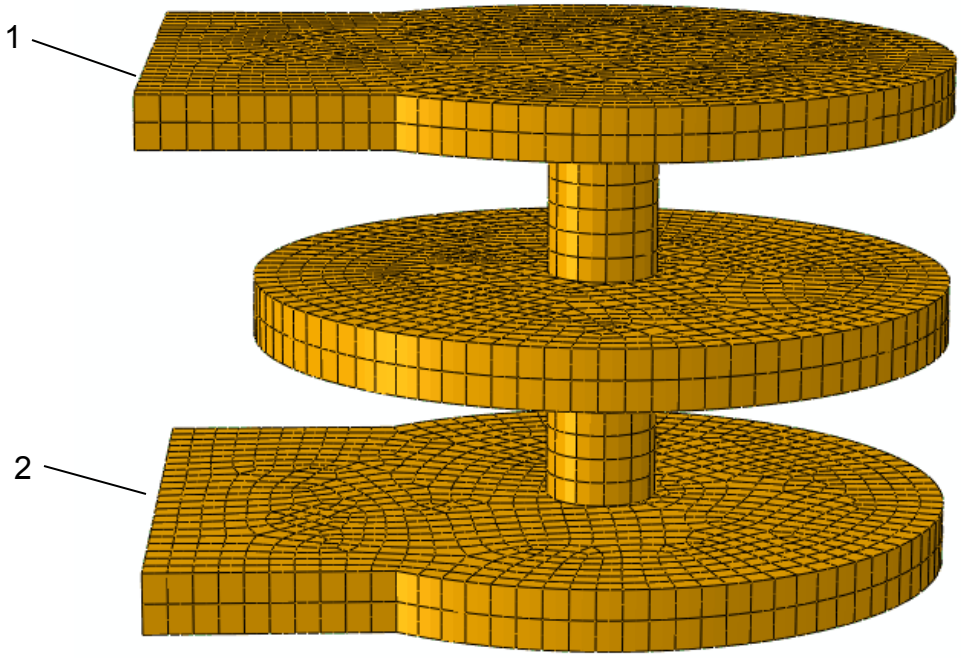

Fig. 42: Example structure: Geometry of the copper via and eventually selected mesh.

faces marked with ‘1’ and ‘2’ in Figure 42. The result shown in Figure 43 indicates that any decoupled mechanical-electrical simulation using a mesh with an element size greater than 0.008 mm (marked in Figure 43) will give inadequate results. After defining the meshing details the structure is cycled thermally four times from room temperature up to 230°C following a sinusoidal loading history in the mechanical model. From the results of this thermo-mechanical analysis the pore volume fraction after thermal cycle is evaluated in an external script and re-imported to serve as an input for the subsequent electrical FEA model. Figure 44 shows the results of this procedure, where the electrical resistance is normalized by the initial electrical resistance. The figure demonstrates that also in the case of the thermo-mechanical analysis for elements smaller than 0.008 mm the solution does not depend on the element size anymore. Furthermore coarser meshes show an incorrectly small increase of the electrical resistance, because these meshes are not fine enough for accurate plasticity and damage predictions.

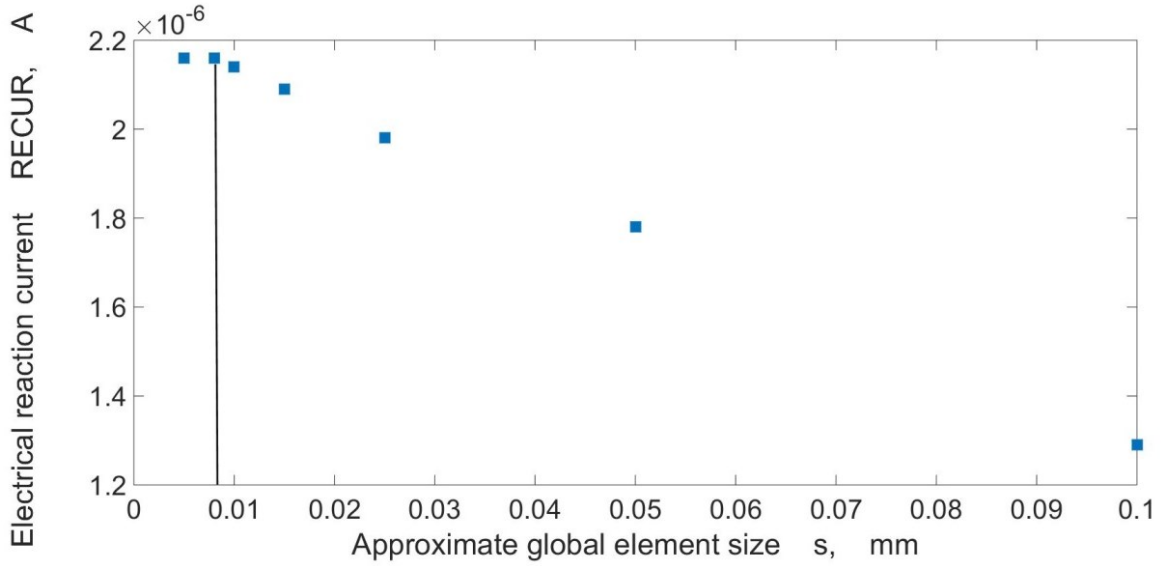

Fig. 43: Influence of the mesh density on the electrical FEA. The threshold below which the result does no longer depend on the element size is marked.

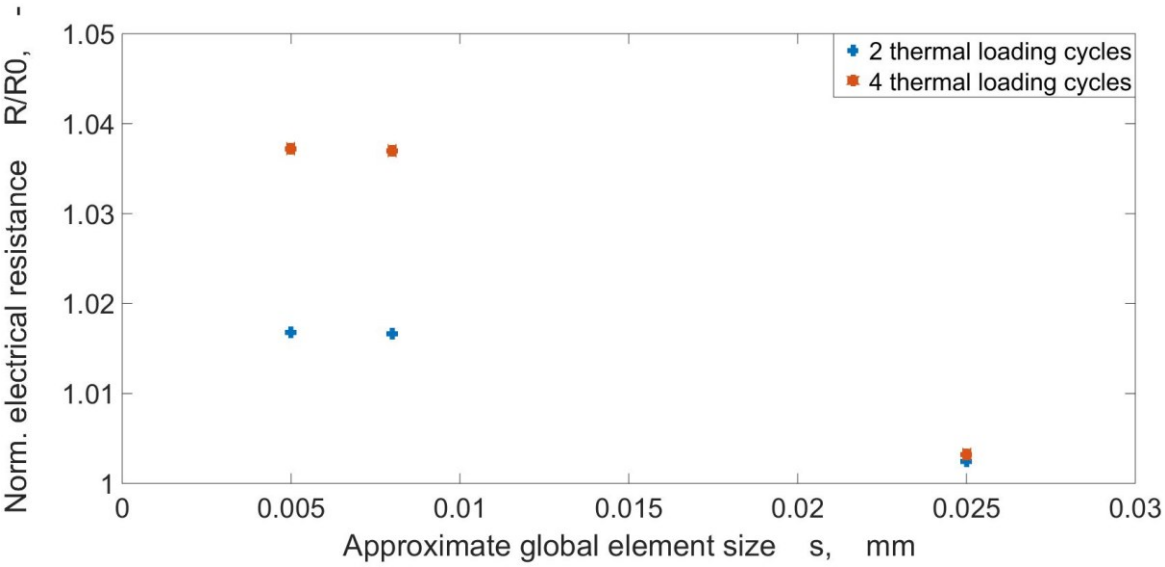

Fig. 44: Influence of the mesh density in the decoupled mechanical-electrical FEA.

In copper regions where the current density is low or near zero and also the mechanical loads are low, a coarser mesh is used in order to save computational time. This approach is validated by comparing the results to the ones in Figure 44. When they are the same as for global element sizes less than 0.008 mm, the proposed mesh can be regarded as acceptable. In this study, for practical reasons, three FEA models are set up. The first one contains the microvia circuit, see Figure 39, the second one the through-hole via and the buried via, see

Figure 40 a) and b) and the third one contains the line structure, see Figure 40 c). In all cases, the layers are modeled separately and assembled using tie constraints [25]. The modeled details are parts of specimens, in which structures repeat themselves within the PCBs, so periodic boundary conditions are applied. They ensure that one edge deforms exactly like the opposite one plus an additional constant determining the stretch of the unit cell. A representative structure is cut out and used as unit cell. Periodicity is enforced only at the faces perpendicular to the free surface. The latter must be left unconstrained. Strictly speaking periodicity only applies well in the longer direction of the PCBs, while in shorter direction the unit cell pattern can be found only two to three times, depending on the design. Nevertheless periodic boundary conditions are imposed, also in that direction. The error caused by that simplification is evaluated by comparing the results with those obtained assuming symmetric boundary conditions. This comparison is deemed admissible since the strains in the model are governed by the orthotropic thermal expansion of the prepregs and cores in the PCB and almost zero shear strains are expected. In the case of symmetric boundary conditions the boundary faces have to remain plane after deformation. This is accomplished by coupling the displacements of all the nodes of one bounding face perpendicular to this surface to a reference point while the corresponding displacements of the opposite boundary face are fixed. Figure 45 shows the Mises stresses in a layer of the microvia-design at 200°C after nine loading cycles. It turns out that the choice of the boundary conditions has almost no influence on the results. In other words both types of boundary conditions work equally well for the selected unit cell.

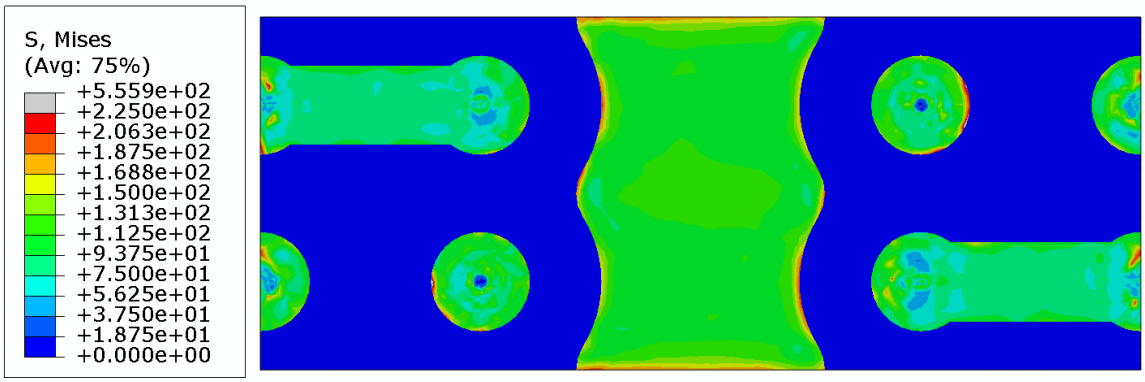

Fig. 45: Stresses in a layer of the microvia-design. They are almost independent of the investigated applied boundary conditions.

3.5 Parameter determination

The procedure described in the foregoing section is employed to determine suitable pore growth parameters for the used copper grade. Hence equation 21 is reevaluated and the parameters A and B are calibrated based on the data from the real IST, i.e., based on the measured number of cycles elapsing until the resistance has risen to 10%. The simulations are then performed for the so-determined cycle number and the numerically determined resistance increase is compared to the 10% resistance increase of the experiments. Figure 46 shows the normalized electrical resistance at a given number of cycles as a function of the parameters A and B for the microvia-design. The color coding corresponds to the ratio of the electrical resistance R to a reference value R_0 of the undamaged material.

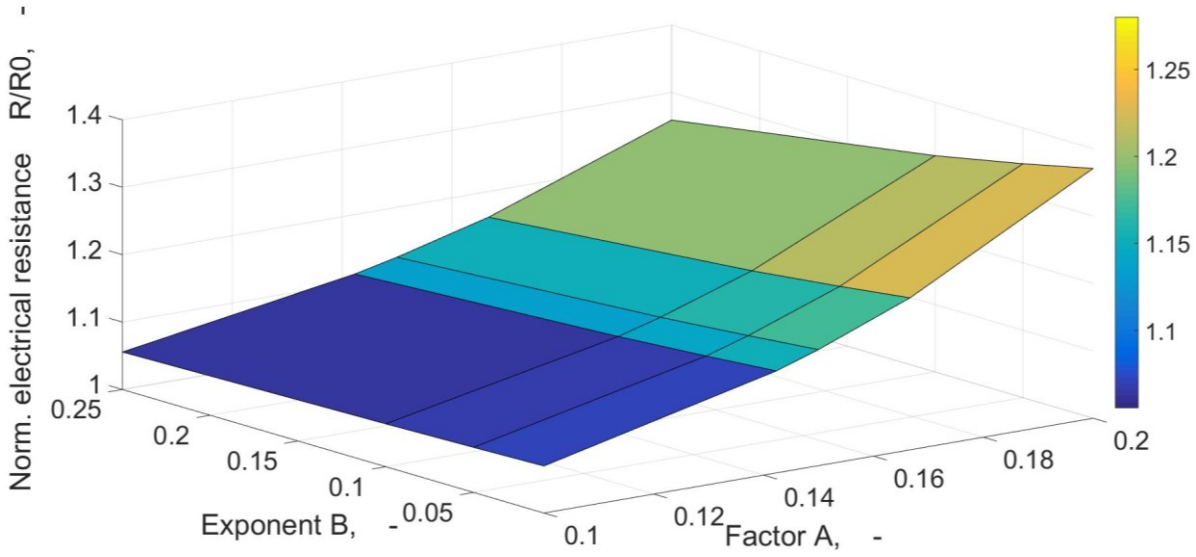

Fig. 46: Normalized electrical resistance of the microvia-design as a function of A and B.

This parameter study is likewise repeated for the structures shown in Figure 40a and 40b and an optimum set of parameters by minimizing the least squares error between all three simulations and measurements according to equations 24 and 25. Equation 24 gives the mean error (ME), equation 25 the root mean square error (RMSE), 1.1 is the value from the tests (10% resistance increase), n is the number of trials, here three, because the line structure (see Figure 40c) is

excluded from the calculations for reasons that will be discussed in the next chapter. Figure 47 shows the residua calculated by equations 24 and 25. The figures focus on the relevant regions with the lowest errors. Based on these results, the optimum set of parameters is A=0.15 and B=0.25.

$$ME = \frac{1}{n}\Sigma|(R/R_0) - 1.1| \tag{24}$$

$$RMSE = \sqrt{\Sigma((R/R_0) - 1.1)^2/n} \tag{25}$$

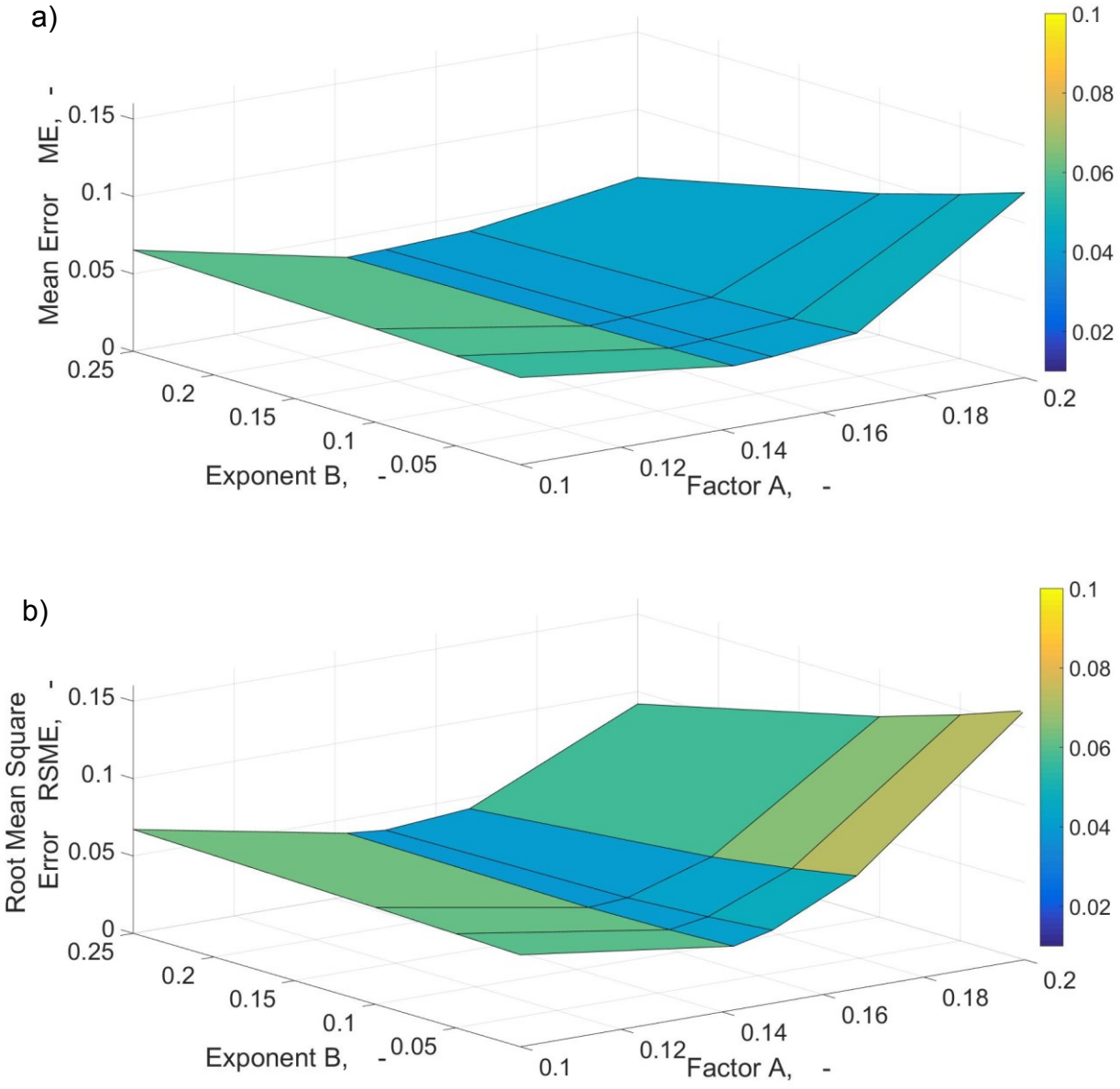

Fig. 47: Residua between simulation and experiment. a) mean error (ME) b) root mean square error (RMSE).

3.6 Results and discussion

Based on the model described in section 3.3 and using the parameters determined in section 3.5 virtual ISTs are conducted. Figure 48 compares the results of the virtual ISTs to those of their real-life counterparts. The number of cycles after which the electrical resistance increases by 10% percent is shown. It should be mentioned that the test is terminated, if the structure survived a thousand cycles. This was the case for the line structure (see Figure 40d), therefore it has been excluded from all further considerations.

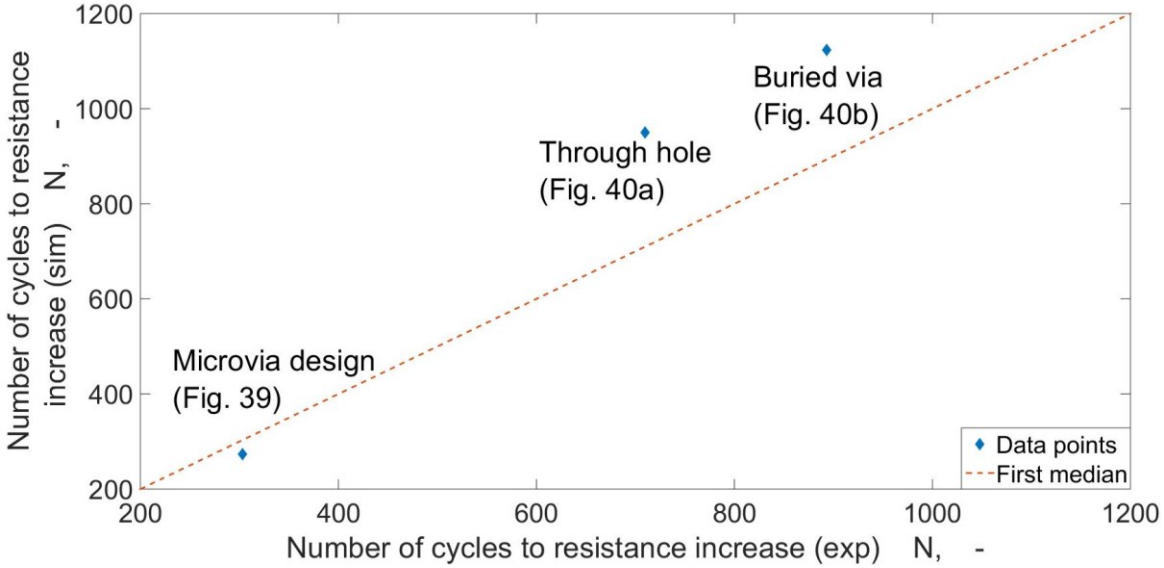

Fig. 48: Comparison of simulation results to experimental results. The number of the figure showing the corresponding design is indicated in the figure.

Figure 48 shows a reasonably reliable correlation between simulations and experiments. The model slightly overestimates rather robust designs (40a and 40b). This may be corrected by underweighting the stress triaxiality σ_m/σ_{eq} in equation 21. However, the researcher refrains from doing so as the triaxiality is known to be crucial to pore growth [30]. Instead, the initial pore volume fraction used for the simulations must be discussed. From density measurements of the used copper grades in the PCBs it is found to be 3.70%. However, it is expected that the initial pore volume fraction will vary for each specific design. Consequently, it is worthily evaluating the initial pore volume fraction for the different designs necessary to achieve a perfect match between the simulated and experimentally measured number of cycles. Table 10 shows the results. An

additional factor comes into play in this context: The initial pore volume fraction is assumed to be constant over the structure due to lacking information on the initial pore fraction distribution. Conversely, it is well known that the thickness of the copper plating as well as the pore volume fraction varies throughout PCBs [66].

Table 10. Initial pore volume fraction

Design	Microvia	Through hole	Buried via
Initial pore volume fraction [%]	2.86	5.80	4.95

The „through hole“ and the „buried via“ designs are known to be prone to the formation of precracks and pores during the production process [66], so assuming a higher average initial pore volume fraction for these structures is reasonable. Please note that the number of cycles needed to increase the pore volume fraction by a certain percentage (see equation 22) does not depend on the initial pore volume fraction. Nevertheless, the correlation between pore volume fraction and specific electrical resistivity is nonlinear (see equation 23) and does depend on the current pore volume fraction. Based on the initial pore volume fraction in Table 10, the pore volume at the experimentally determined number of cycles to resistance increase is computed. The results are found to be in good agreement with micrographs of PCBs tested in the IST, see Figure 49. The micrographs show that for the “through hole” design cracks generally occur at the corner of the barrel, while they occur at its center for the “buried via” design. For the microvia design the cracks are found somewhere in the region near the via. In this study, the exact geometry of the vias (see the micrographs) had to be slightly simplified in the simulation as production-related fluctuations are very difficult to reproduce in FEM models; this may also affect the results. This is especially true for the microvia design, where also the diameter of the vias differs in some cases from the specifications, see Figure 49. Furthermore, the pore growth is calculated based on the stabilized cycle, neglecting the shakedown behavior of the material. Another source of uncertainty may be the fact that pore nucleation [74-76] in the material has not been taken into account in the model since the initial pore volume fraction is already considerable and thus pore growth can be considered as dominant over nucleation. In continuation of the methodology proposed in this work the logical

next steps in a future work will be (i) to evaluate more PCB designs to strengthen the correlation shown in Figure 48 and (ii) to develop a methodology to measure the locally varying pore distribution in PCBs.

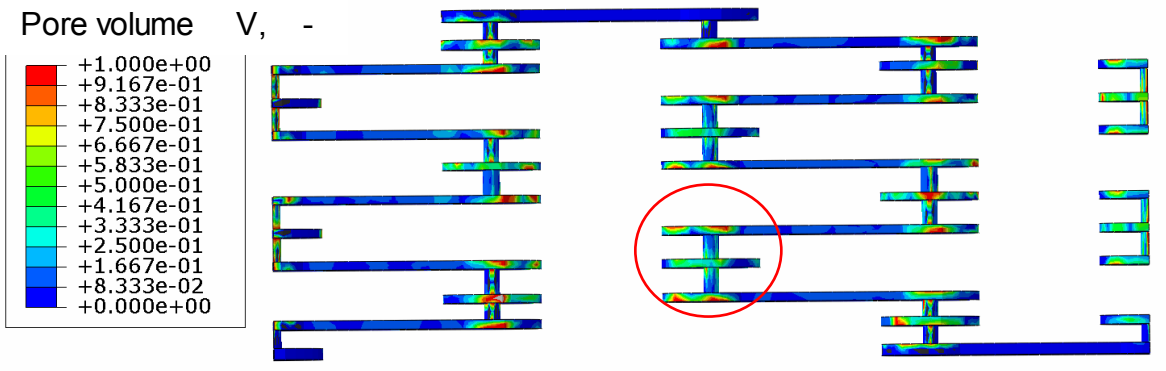

a)

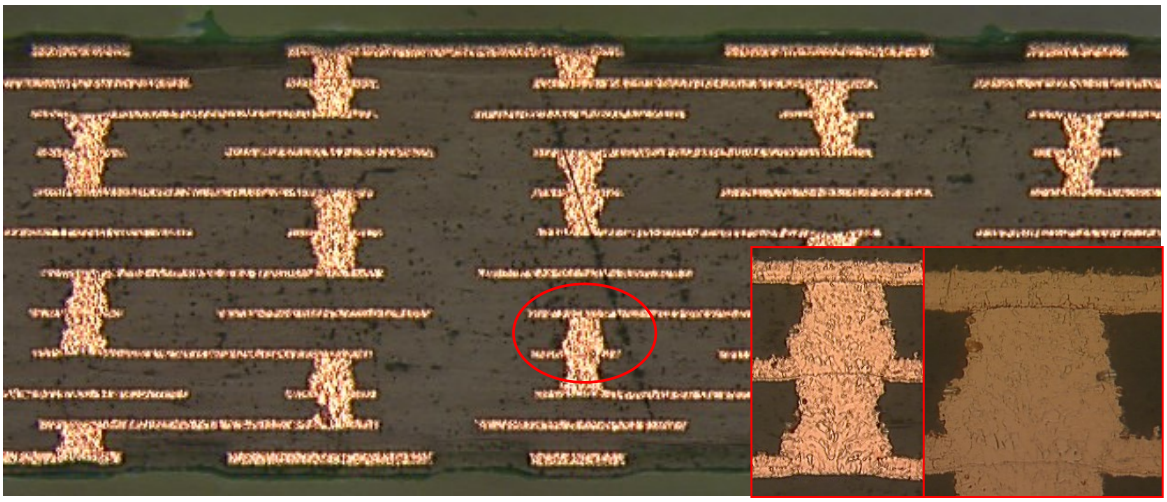

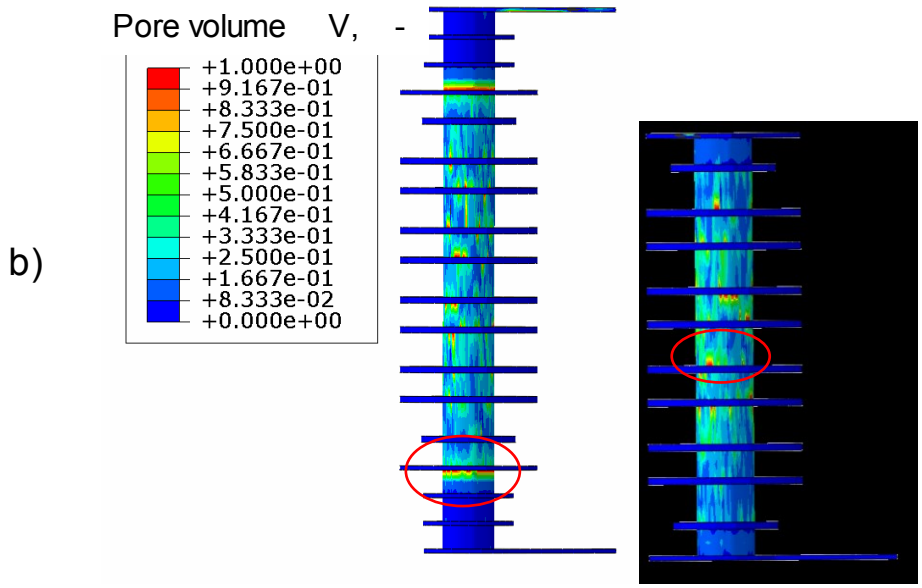

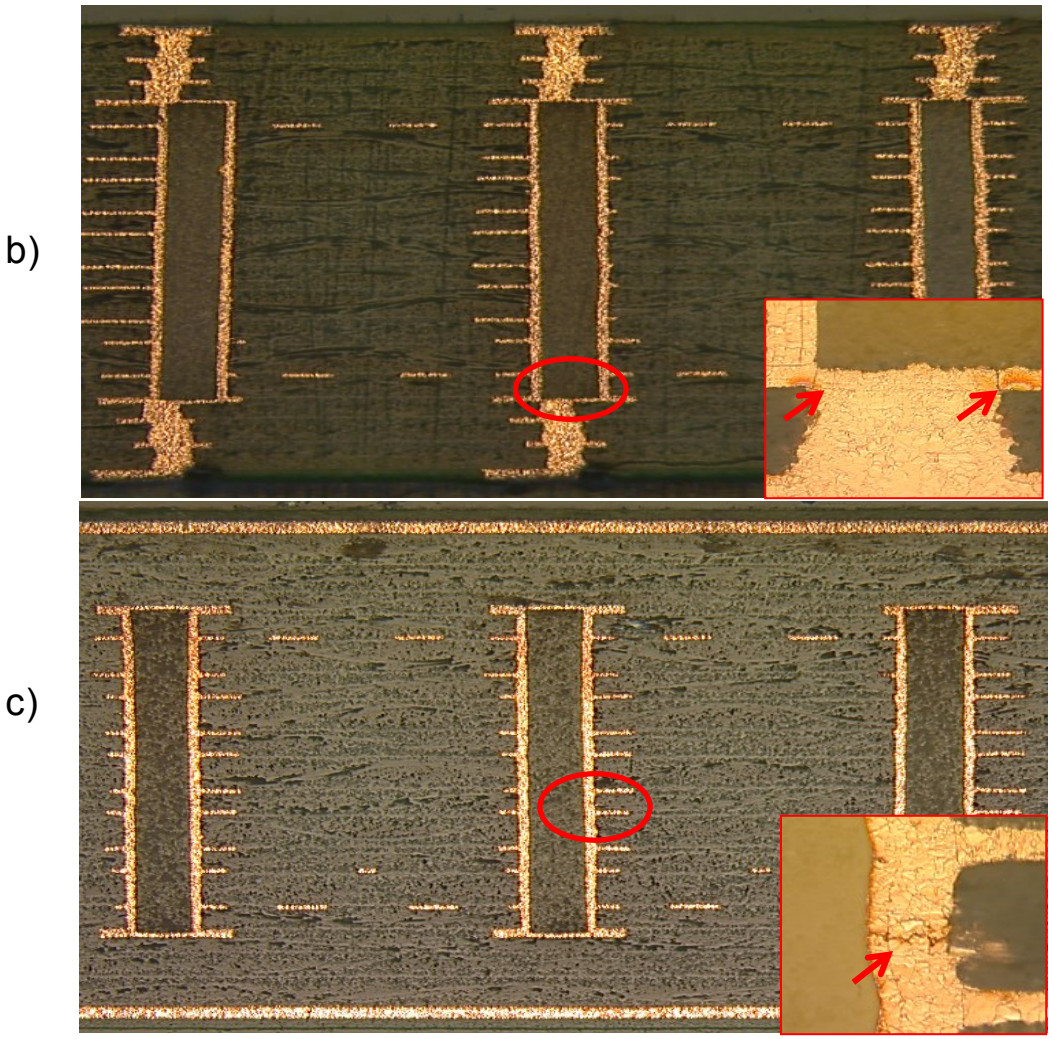

Fig. 49: Comparison of stress patterns to micrographs: a) microvia, b) through hole and c) buried via.

4. CONCLUSION AND OUTLOOK

In this thesis first an experimental and numerical study to characterize thin copper layers for PCB applications has been conducted. Cyclic four point bending tests with composite copper-silicone specimens were intended to measure cyclic strains up to one percent in order to determine plastic material parameters of copper. Because of the low stiffness of the silicone rubber, the bearings were pressed into the silicone during the testing. As a result, failure occurred at one of the bearings, where no strain measurement is possible. Besides, due to the hyperelastic material behavior of silicone, resulting in stress concentrations and low overall stresses in the copper layers, only strains up to 0.1 percent could be measured. In order to measure cyclic strains in the desired range of up to one percent, further testing was necessary. For these tests stiffer substrates were used. Substrates used in the four point bend test must have a certain minimum thickness to provoke strains of one percent at a given, technically possible, deflection. As force signals obtained from composite specimens made of an about 10 mm thick stiff substrate and 18 µm thick copper layers, do not contain any useable information about the copper's mechanical behavior anymore, bending tests could not be used. Therefore, specimens consisting of thin layers of glass fiber reinforced epoxy resins as substrate and copper foils were tested in cyclic tensile-compression tests to obtain the copper material behavior in a larger strain regime. In order to prevent buckling, suitable fixtures were used and the specimens were made of several layers of glass fiber reinforced epoxy resins and copper to increase their thickness. Hence the cyclic mechanical behavior of thin copper layers in all desired strain intervals could be characterized. These tests were modeled in FEA-simulations in order to determine the material input parameters for a "Nonlinear isotropic/kinematic hardening model" of the thin copper layers in an optimization process. The model was found to be in good agreement with the measured results for most R-ratios. The kinematic hardening parameters were fitted in an optimization process from the hysteretic force-strain curves obtained in the cyclic tension-compression tests. The isotropic hardening variables were determined based on the yield stress versus plastic strain relationship that was constructed

incrementally from the available individual cycles. As the isotropic hardening behavior could not be represented by a unique relationship, a phenomenological model was developed to choose the correct isotropic hardening properties. To this end, a novel idea was presented that takes into account the mean stress sensitivity as it is commonly observed in fatigue tests. A correlation between the yield stress and the mean force in the tests was observed. To account for that a phenomenological approach was proposed. The basic idea was to introduce a further internal variable c memorizing the mean stress. As the overall backstress $\boldsymbol{\alpha}$ gives the center of the elastic region, the first invariant of the backstress $I_1(\boldsymbol{\alpha})$ is calculated and integrated over a certain timespan. This “mean backstress memorization” model worked well for all investigated temperatures. For the sake of simplicity it was implemented in Abaqus in a semi-explicit way using the concept of a “User defined field variable (USDFLD)”. The developed material model was validated for non-isothermal cases based on curvature measurements of wafer bow samples subjected to thermal cycling. For these tests specimen consisting of silicon and copper were used. The model reproduced the measured material behavior very well.

Finally a methodology was presented that allows to numerically assess the performance of new PCB designs in the IST. It is based on a sequential analysis of a PCB subjected to thermal cycling, whose stress-strain response gives rises to a pore volume fraction distribution that deteriorates the conductance properties of the current paths of the PCB. This resistance increase has been simulated and the results have been compared with experiments. A well calibrated pore fraction evolution law allows to reliably predict the electrical performance of various PCB designs as well as draw some conclusions on the initial pore volume fraction in the PCB prior to operation. For the technical implementation of the developed methodology some minor simplifications had to be made. First, the geometry of the conducting paths had to be slightly simplified in the simulation as production-related fluctuations are very difficult to reproduce in FEM models. Second, the pore nucleation in the material was not taken into account in the model since the initial pore volume fraction was already considerable and thus pore growth could

be considered as dominant over nucleation. Nevertheless, the prediction of the electrical performance of the tested PCB design was convincing, the model parameters were in reasonable agreement with literature values. Hence the assumptions made can be regarded as acceptable. Moreover, the developed methodology allows a quick and reliable assessment of the performance of PCBs in the IST.

The logical next steps in a future work will be (i) to evaluate more PCB designs to strengthen the developed correlation and (ii) to develop a methodology to measure the locally varying pore distribution in PCBs. Moreover, the influence of the production and the reflow process on the copper in PCBs should be evaluated. Both processes are likely to cause residual stresses and damage in the copper layers. Eventually also transient thermal simulations of the IST could be conducted in order to account for stresses generated by the temperature distribution inside the PCB. This is especially interesting for thermal shock tests.

The developed concepts have proven their predictive power and have already successfully been applied in the development process of PCBs. A further refinement of the simulation methods presented in this thesis along with an increase of computational power has the potential to eventually allow designing and optimizing the entire production process in a virtual environment thereby reducing the need for costly experiments.

BIBLIOGRAPHY

1. JESD51-6: Integrated Circuit Thermal Test Method Environmental Conditions - Forced Convection (Moving Air). Jedec Solid State Technology Association, 1999

2. JESD51-8: Integrated Circuit Thermal Test Method Environmental Conditions — Junction-to-Board. Jedec Solid State Technology Association, 1999

3. JESD51-2A: Integrated Circuits Thermal Test Method Environmental Conditions - Natural Convection (Still Air). Jedec Solid State Technology Association, 2008

4. JESD22-A106B: Thermal Shock. Jedec Solid State Technology Association, 2004; REAFFIRMED: 2011

5. Amy, R.A., Aglietti, G.S., Richardson, G.: Accuracy of simplified printed circuit board finite element models. Microelectronics Reliability 50(1), 86–97 (2010). doi: 10.1016/j.microrel.2009.09.001

6. Fuchs, P.F., Pinter, G., Major, Z.: PCB drop test lifetime assessment based on simulations and cyclic bend tests. Microelectronics Reliability 53(5), 774–781 (2013). doi: 10.1016/j.microrel.2013.01.001

7. Li, L., Kim, S., Song, S., Ku, T., Song, W., Kim, J., Chong, M., Park, J., Kang, B.: Finite element modeling and simulation for bending analysis of multi-layer printed circuit boards using woven fiber composite. Journal of Materials Processing Technology 201(1-3), 746–750 (2008). doi: 10.1016/j.jmatprotec.2007.11.190

8. Yang, F., Meguid, S.A.: Efficient multi-level modeling technique for determining effective board drop reliability of PCB assembly. Microelectronics Reliability 53(7), 975–984 (2013). doi: 10.1016/j.microrel.2013.03.014

9. Abad, M.D., Parker, S., Kiener, D., Primorac, M.-M., Hosemann, P.: Microstructure and mechanical properties of CuxNb1−x alloys prepared by ball milling and high pressure torsion compacting. Journal of Alloys and Compounds 630, 117–125 (2015). doi: 10.1016/j.jallcom.2014.11.193

10. Kiener, D., Motz, C., Rester, M., Jenko, M., Dehm, G.: FIB damage of Cu and possible consequences for miniaturized mechanical tests. Materials Science and Engineering: A 459(1-2), 262–272 (2007). doi: 10.1016/j.msea.2007.01.046

11. Kiener, D., Motz, C., Dehm, G.: Micro-compression testing: A critical discussion of experimental constraints. Materials Science and Engineering: A 505(1-2), 79–87 (2009). doi: 10.1016/j.msea.2009.01.005

12. Kiener, D., Motz, C., Grosinger, W., Weygand, D., Pippan, R.: Cyclic response of copper single crystal micro-beams. Scripta Materialia 63(5), 500–503 (2010). doi: 10.1016/j.scriptamat.2010.05.014

13. Stefenelli, M., Daniel, R., Ecker, W., Kiener, D., Todt, J., Zeilinger, A., Mitterer, C., Burghammer, M., Keckes, J.: X-ray nanodiffraction reveals stress distribution across an indented multilayered CrN–Cr thin film. Acta Materialia 85, 24–31 (2015). doi: 10.1016/j.actamat.2014.11.011

14. JESD22-B111: Board Level Drop Test Method of Components for Handheld Electronic Products. Jedec Solid State Technology Association, 2003

15. Fuchs, P., Major, Z.: Cyclic bend tests for the reliability evaluation of printed circuit boards under dynamic loads. Frattura ed Integrità Strutturale(15), 64–73 (2011)

16. Wong, E., Seah, S., Shim, V.: A review of board level solder joints for mobile applications. Microelectronics Reliability 48(11-12), 1747–1758 (2008). doi: 10.1016/j.microrel.2008.08.006

17. Wong, E., Seah, S., van Driel, W., Caers, J., Owens, N., Lai, Y.-S.: Advances in the drop-impact reliability of solder joints for mobile applications. Microelectronics Reliability 49(2), 139–149 (2009). doi: 10.1016/j.microrel.2008.12.001

18. Luan, J.-e., Tee, T.Y., Pek, E., Lim, C.T., Zhong, Z.: Dynamic responses and solder joint reliability under board level drop test. Microelectronics Reliability 47(2-3), 450–460 (2007). doi: 10.1016/j.microrel.2006.05.012

19. Wong, E., Seah, S., Selvanayagam, C., Rajoo, R., Driel, W., Caers, J., Zhao, X., Owens, N., Leoni, M., Tan, L., Lai, Y.-S., Yeh, C.-L.: High-Speed Cyclic

Bend Tests and Board-Level Drop Tests for Evaluating the Robustness of Solder Joints in Printed Circuit Board Assemblies. Journal of Electronic Materials 38(6), 884–895 (2009). doi: 10.1007/s11664-008-0610-5

20. Stam, F.A., Davitt, E.: Effects of thermomechanical cycling on lead and lead-free (SnPb and SnAgCu) surface mount solder joints. Microelectronics Reliability 41(11), 1815–1822 (2001). doi: 10.1016/S0026-2714(01)00087-7

21. Zhang, J., Jiang, Y.: Constitutive modeling of cyclic plasticity deformation of a pure polycrystalline copper. International Journal of Plasticity 24(10), 1890–1915 (2008). doi: 10.1016/j.ijplas.2008.02.008

22. Hsu, T.-Y.J., Wang, Z.: Cyclic stress–strain response and microstructure evolution of polycrystalline Cu under pure compressive cyclic loading condition. Materials Science and Engineering: A 615, 302–312 (2014). doi: 10.1016/j.msea.2014.07.047

23. You, J.-H., Miskiewicz, M.: Material parameters of copper and CuCrZr alloy for cyclic plasticity at elevated temperatures. Journal of Nuclear Materials 373(1-3), 269–274 (2008). doi: 10.1016/j.jnucmat.2007.06.005

24. AbaqusV6.12. Abaqus Theory Manual. Providence, RI, USA: Abaqus Inc.; 2012.

25. AbaqusV6.12. Abaqus Analysis User's Manual. Providence, RI, USA: Abaqus Inc.; 2012.

26. Chaboche, J.: A review of some plasticity and viscoplasticity constitutive theories. International Journal of Plasticity 24(10), 1642–1693 (2008). doi: 10.1016/j.ijplas.2008.03.009

27. Lemaitre, J., Chaboche, J.-L.: Mechanics of Solid Materials. Cambridge University Press, Cambridge (1990)

28. Chaboche JL, Dang-Van K. and Cordier G.: Modelization of the strain memory effect on the cyclic hardening of 316 stainless steel. In: International Conference on Structural Mechanics in Reactor Technology (SMIRT) 5, Berlin, Germany, 1979.

29. Pardoen, T., Delannay, F.: Assessment of void growth models from porosity measurements in cold-drawn copper bars. Metallurgical and Materials Transactions A 29 (7), 1895-1909 (1998)

30. Rice, J.R., Tracey, D.M.: On the ductile enlargement of voids in triaxial stress fields. Journal of the Mechanics and Physics of Solids 17, 201-17 (1969)

31. Huang Y.: Accurate dilatation rates for spherical voids in triaxial stress fields. Journal of Applied Mechanics 58, 1084-85 (1991)

32. Marini, B., Mudry, F., Pineau, A.: Experimental study of cavity growth in ductile rupture. Engineering Fracture Mechanics, 22 (6), 989-96 (1985)

33. General principles (ISO 527-1:2012), Aufl. Berlin: Beuth. 2012.

34. Goldenberg, N., Arcan, M., et al: On the most suitable specimen shape for testing shear strength of plastics. ASTM STP 247, 115–21 (1958)

35. Arcan, M., Hashin, Z., et al: A method to produce uniform plane-stress states with applications to fiber-reinforced materials. Experimental Mechanics 18, 141–146 (1978)

36. Arcan, M.: Discussion of the iosipescu shear test as applied to composite materials. Experimental Mechanics 24, 66–70 (1984)

37. Adams, D.O., Moriarty, J.M., Gallegos, A.M., Adams, D.F.: The V-Notched Rail Shear Test. Journal of Composite Materials 41(3), 281–297 (2006). doi: 10.1177/0021998306063369

38. Feichter, C.: Characterization of the Fatigue Behavior of Elastomer Compounds by Fracture Mechanics Methods. Dissertation. University of Leoben. Institute of Materials Science and Testing of Plastics. II 1.1 – II 1.10 (2006)

39. Javořik, J., Dvořàk, Z.: Equibiaxal Test of Elastomers. In: KGK (Kautschuk Gummi Kunststoffe) November 2007, 608–610 (2007)

40. Böhm, H.J.: A short introduction to basic aspects of continuum micromechanics. Institute of Lightweight Design and Structural Biomechanics (ILSB), Vienna University of Technology, (1998)

41. Benveniste Y.: A new approach to the application of Mori–Tanaka's theory in composite materials. Mechanics of Materials 6 (2), 147–157, (1987)

42. DIGIMAT 4.4.1: user documentation, Louvain-la-Neuve, Belgium, e-Xstream engineering, 2013

43. Jawitz, M.W., Jawitz, M.J.: Materials For Rigid And Flexible Printed Wiring Boards, Taylor and Francis Group, LLC, Boca Raton London New York (2007)

44. Fuchs, P., Pinter, G., Tonjec, M.: Determination of the orthotropic material properties of individual layers of printed circuit boards. Microelectronics Reliability 52(11), 2723–2730 (2012). doi: 10.1016/j.microrel.2012.04.019

45. Fellner, K.: Simulation of the "Single Via Thermal Cycle Test" - modelling and determination of the material input parameters. Master's thesis, University of Leoben. Institute of Materials Science and Testing of Plastics (2012)

46. Uetz, H., Wiedemeyer J.: Tribologie der Polymere. Grundlagen u. Anwendung in d. Technik; Reibung - Verschleiß - Schmierung. Carl Hanser Verlag, München Wien (1985)

47. Park, J.-H., An, J.-H., Kim, Y.-J., Huh, Y.-H., Lee, H.-J.: Tensile and high cycle fatigue test of copper thin film. Materialwissenschaft und Werkstofftechnik 39(2), 187–192 (2008). doi: 10.1002/mawe.200700262

48. Ledbetter, H. M., Naimon E.R.: Elastic Porperties of Metals and Alloys. II. Copper. The Journal of Physical Chemistry, 3 (4) 897-935 (1974)

49. Brommundt, E., Sachs, G.: Sachau, D.: Technische Mechanik. Eine Einführung. 4. Aufl. München [u.a.]: Oldenbourg. 165-168 (2007)

50. Chaboche, J.-L., Gaubert, A., Kanouté, P., Longuet, A., Azzouz, F., Mazière, M.: Viscoplastic constitutive equations of combustion chamber materials including cyclic hardening and dynamic strain aging. International Journal of Plasticity 46, 1–22 (2013). doi: 10.1016/j.ijplas.2012.09.011

51. Chaboche, J.L.: Constitutive equations for cyclic plasticity and cyclic viscoplasticity. International Journal of Plasticity 5, 247–302 (1989)

52. Ohno, N.: A constitutive model of cyclic plasticity with a non-hardening strain region. Journal of Applied Mechanics 49, 721 (1982)

53. Bari, S., Hassan, T.: Anatomy of coupled constitutive models for ratcheting simulation. International Journal of Plasticity 16(3-4), 381–409 (2000). doi: 10.1016/S0749-6419(99)00059-5

54. Rezaiee-Pajand, M., Sinaie, S.: On the calibration of the Chaboche hardening model and a modified hardening rule for uniaxial ratcheting prediction. International Journal of Solids and Structures 46(16), 3009–3017 (2009). doi: 10.1016/j.ijsolstr.2009.04.002

55. LS-Opt 4.2, A design optimization and probabilistic analysis tool for the engineering analyst, LSTC, CA, USA, 2011

56. Chaboche, J.L.: On some modifications of kinematic hardening to improve the description of ratchetting effects. International Journal of Plasticity 7 (7), 661–678 (1991)

57. Stephens, R.I.: Metal fatigue in engineering, 2nd edition. A Wiley-Interscience publication. Wiley, New York, NY (2001)

58. AbaqusV6.12. Abaqus User Subroutines Reference Manual. Providence, RI, USA: Abaqus Inc.; 2012.

59. Huang, R., Taylor, C. A., Himmelsbach, S., Ceric, H., & Detzel, T.: Apparatus for measuring local stress of metallic films, using an array of parallel laser beams during rapid thermal processing. Measurement Science and Technology 21(5) (2010)

60. Floro, J. A., Chason, E.; Krauss, A. R. (Ed.), Auciello, O. (Ed.): Curvature-based techniques for real-time stress measurement during thin film growth. In: In-Situ Characterization of Thin Film Growth Processes, John Wiley and Sons, 191-216 (2001)

61. Stoney, G. G.: The tension of metallic films deposited by electrolysis. Proceedings of the Royal Society of London. Series A, Containing Papers of a Mathematical and Physical Character 82 (553), 172-175 (1909)

62. Janssen, G. C. A. M., Abdalla, M. M., Van Keulen, F., Pujada, B. R., Van Venrooy, B.: Celebrating the 100th anniversary of the Stoney equation for film

stress: Developments from polycrystalline steel strips to single crystal silicon wafers. Thin Solid Films 517(6), 1858-1867 (2009)

63. Freund, L. B., Suresh, S.; Film stress and substrate curvature. Thin film materials: stress, defect formation and surface evolution. 86-153. Cambridge University Press, Cambridge (2008)

64. Hopcroft, M.A., Nix, W.D., Kenny, T.W.: What is the Young's Modulus of Silicon? Journal of Microelectromechanical Systems 19(2), 229–238 (2010). doi: 10.1109/JMEMS.2009.2039697

65. Okada, Y., Tokumaru, Y.: Precise determination of lattice parameter and thermal expansion coefficient of silicon between 300 and 1500 K. Journal of Applied Physics. 56(2) 314-320 (1984)

66. Coombs, C.F.: Printed circuits handbook, 6th edition. McGraw-Hill handbooks. McGraw-Hill, New York (2008)

67. Birch, B.: Reliability testing for microvias in printed wire boards. Circuit World 35(4), 3–17 (2009). doi: 10.1108/03056120911002361

68. Birch, B.: Interconnect Stress Test PWB Corp, PWB Interconnect Solutions Inc., Nepean, Ontario, Canada, 2003

69. Koh, J.C.Y., Fortini, A.: Thermal conductivity and electrical resistivity of porous material. NASA topical report, contract NAS 3-12012 (1971).

70. Jerabek, M., Major, Z., Lang, R.: Strain determination of polymeric materials using digital image correlation. Polymer Testing 29, 407–416 (2010)

71. Beremin, F.M.: in Three-Dimensional Constitutive Relations and Ductile Fracture, S. Nemat-Nasser, ed., North-Holland Publishing Company, Amsterdam, 185-205 (1981).

72. El-Hadek, M.A., Kaytbay, S.: Mechanical and physical characterization of copper foam. International Journal of Mechanics and Materials in Design 4(1), 63–69 (2008). doi: 10.1007/s10999-008-9058-2

73. Friedrich Tabellenbuch Elektrotechnik/Elektronik. 582. Auflage. Bildungsverlag EINS, Köln 2007

74. Chu, C.-c., Needleman, A.: Void nucleation effects in biaxially stretched sheets. Journal of Engineering Materials and Technology 102, 249–256 (1980)

75. Fleck N A, Hutchinson J W, Tvergaard V: Softening by void nucleation and growth in tension and shear. Journal of the Mechanics and Physics of Solids 37 (4), 515–540 (1989)

76. Tvergaard, V., Hutchinson, J.W.: Two mechanisms of ductile fracture: void by void growth versus multiple void interaction. International Journal of Solids and Structures 39(13-14), 3581–3597 (2002)